Technische Universität München
TUM School of Computation, Information and Technology

Influence of Automotive Coatings on 77 GHz Radar Sensors for Advanced Driver Assistance Systems and Autonomous Driving

Christian Alexander Constantin Winter

Vollständiger Abdruck der von der TUM School of Computation, Information and Technology der Technischen Universität München zur Erlangung eines

Doktors der Ingenieurwissenschaften (Dr.-Ing.)

genehmigten Dissertation.

Vorsitz: Prof. Dr.-Ing. Martin Buss

Prüfer*innen der Dissertation:

1. Prof. Dr.-Ing. habil. Erwin Biebl
2. Priv.-Doz. Dr.-Ing. Thomas Kleine-Ostmann

Die Dissertation wurde am 28.10.2022 bei der Technischen Universität München eingereicht und durch die TUM School of Computation, Information and Technology am 14.03.2023 angenommen.

Abstract

For highly automated driving functions, a variety of sensors, such as camera, lidar and radar have to be integrated into the vehicle. Radar sensors are not obscured by direct sunlight and maintain their performance during rain, which are advantages when compared to camera and lidar. Furthermore, they achieve highest precision when estimating angle, velocity and distance of a target. As a result, radar represents an indispensable sensor technology for future advanced driver assistance systems and autonomous driving. Currently, state of the art automotive radar sensors are operating between 76 - 77 GHz. Since the functional load on radar sensors is still increasing, an increasing number of radar sensors is needed per vehicle. This is challenging from a design perspective. Therefore, a hidden integration behind painted plastic parts such as radomes or bumpers is favorable. In this thesis, the influence of painted plastic parts on radar transparency is evaluated. First, the dielectric properties of polypropylene and polycarbonate are evaluated utilizing the permittivity, in order to evaluate possible advantages of the materials for radar. Furthermore, the influence of different coating application techniques is evaluated to choose the best possible application for radar transparency. In order to evaluate the direct impact on the sensor, deviation in angle estimation are investigated as well as influences on the capability of separating targets. The same measurements regarding angle estimation and separability are repeated with different titanium dioxide concentrations reaching from 20 to 60 %.

Acknowledgement

This work resulted from a cooperation between the BMW Group and the Associated Professorship of Microwave Engineering at TU Munich. It would not have been possible without the support of many people, which I would like to thank in the following. First of all I would like to thank Prof. Dr. Erwin Biebl from university side and Dr. Stefan Holzknecht from BMW side, for agreeing to supervise this thesis and their scientific advices and support. Furthermore, I would like to thank Dr. Ingo Weber for giving me the chance to conduct the thesis within the radar group at BMW. Also I would like to thank my former BMW radar colleagues for all the scientific discussions about permittivity determination and radar sensors in general. In addition, I want to thank my former PhD colleagues and students from university as well as BMW. I also want to extend my gratitude to my BMW colleagues at TI-314 and TI-311 as well as all my colleagues in Landshut for producing all painted samples used in this thesis and making all micrographs, REM as well as EDX pictures for me. Finally I want to thank my friends and family for all the support during this project.

Contents

CHAPTER 1

Introduction

Introduced approximately 50 years ago, the Anti-lock Braking System (ABS) can be considered to be the first Driver Assistance System (DAS) [1]. Since then, many systems have been developed to guarantee an overall safer driving. In contrast to DAS, Advanced Driver Assistance Systems (ADAS) and Autonomous Driving (AD) make use of various sensors observing the surrounding environment. These sensor types include camera, lidar and radar. Using multiple sensor types in one vehicle brings advantages such as redundancy and compensation of the individual sensor limits. In contrast to radar, a camera's view can be obstructed by direct sunlight and suffers from performance degradation in certain environmental conditions like rain and fog. Radar technology has been an inherent part in the automotive sector for over 20 years. It was first introduced in 1998 as an operational series product by Mercedes-Benz with the Adaptive Cruise Control (ACC) system DISTRONIC operating at 77 GHz [2]. This system allows an automated adjustment of the speed to maintain a safe distance to other vehicles driving ahead by braking or cutting the engine power. BMW introduced its first radar based ACC system in the year 2000. Since then, ADAS have developed further including Blind Spot Detection (BSD), Automatic Emergency Brake Assist (AEB) and Highway Assist (HA), which rely heavily on the information provided by radar sensors. According to the Society of Automotive Engineers (SAE), the degree of automation can be divided into six levels [3]. Level 0 describes a vehicle with no automation at all, meaning that the driver is in control all the time. This level includes assistance systems just like BSD, since it just warns the driver without intervening. Functions like ABS and ACC can be classified as Level 1 functions, leaving the authority to the driver while taking care of specific driving functions. Systems which are able to perform more complex operations are classified as Level 2, including ADAS such as HA. The latter one can control the vehicle laterally as well as longitudinally and can overtake other vehicles on the highway by initiating the maneuver upon activation of the indicator by the driver.

The vehicle can steer, accelerate and brake on its own to perform the overtaking [1]. Furthermore, the system will not overtake when detecting vehicles behind, avoiding a possible collision. While the driver must be able to resume control over a Level 2 vehicle at any time, continuous monitoring is not necessary at Level 3. However, the driver still needs to take control when requested by the vehicle, thus only realizing a conditional automation. An example for a Level 3 function would be an evolution of the HA, which makes the decisions of overtaking without being triggered directly by the driver [1]. Level 4 can be seen as an extension where the driver does only have to intervene rarely. The sixth and final level of automation does not require a driver at all and the vehicle is able to perform driving at all speeds independent of any road types on its own [4]. With increasing level of automation, the functional load on the sensor itself increases. Therefore, more sensors have to be integrated into the vehicle, making it challenging from a design perspective. Especially for radar sensors, a hidden integration is favorable. Usually the sensor is integrated behind a design radome or a painted plastic bumper. As a result, the performance of the radar sensor is affected. Reflections of the radiation on these surfaces deteriorate the angular resolution and object separation capability of the system. A high attenuation leads to a noticeable reduction of the detection range. Besides the curvature of the component placed in front of the radar, the coating has the highest impact on how the sensor performs. Therefore, radar transparent coatings are favorable. In order to classify automotive coatings as radar transparent, it is crucial to understand the influence of coatings on radar. There are several factors influencing the radar transparency of coatings, including the ingredients of the coating as well as the application technique.

1.1 State of the Art

Currently, in the automotive sector Frequency-Modulated Continuous Wave (FMCW) radars are used. This type of radar enables a precise estimation of distances as well as a simultaneous estimation of the radial velocity. In general there are three different types of radar sensors mainly differing in the range they are functioning in:

Short Range Radar (SRR): The SRR is used for monitoring short distances utilizing a large azimuth opening angle. This type of radar is used for ADAS like BSD or AEB. In order to cover a large area around the vehicle, multiple SRRs are integrated into one vehicle. SRRs used to operate at 24 GHz using the ultra-wideband. However, regulations only allowed using a narrow-band, which decreases the possible range resolution drastically. As a result, the frequency was switched to 77 GHz utilizing a bandwidth of 1 GHz by mostly premium automotive companies. Moreover, the increased frequency allows to build a much more compact sensor. Usually SRRs are integrated behind painted bumpers.

Mid Range Radar (MRR): This radar is currently used to realize functions like ACC. As state of the art SRR sensors, MRR sensors are also operating at 77 GHz with the same bandwidth. MRR sensors are usually integrated into the front of the car

behind radomes in the lower air intake or at the height of the license plate. The radomes can vary from a simple plastic cover to complex design elements. This will be explained in detail later. Currently, one MRR sensor can be integrated per vehicle as an option.

Full Range Radar (FRR): FRR sensors are capable of monitoring large distances of 200 m and upwards. Like MRR, they are usually integrated behind radome structures. The amount of FRRs integrated into one vehicle strongly depends on the level of automation the vehicle is capable of.

(a)

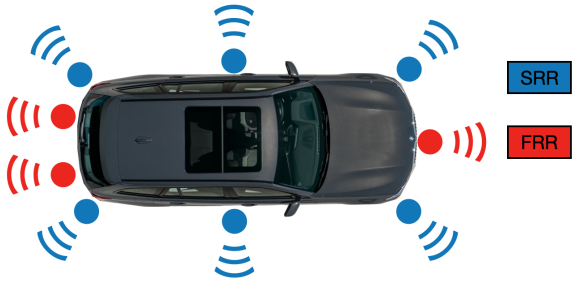

(b)

Figure 1.1: a) Configuration of radar sensors for Level 2 capable vehicle. This setup consists of four SRRs integrated behind painted plastic bumpers in the front and the back. In addition one MRR is integrated into the front behind a radome. b) Possible Level 3 configuration consisting of two additional SRR sensors integrated into the side skirts under the B-Pillar. In addition, the MRR in the front is replaced by a FRR sensor. Additionally two FRR are located at the back.

The type and amount of radar sensors integrated into the vehicle strongly depends on the level of automation. Currently Level 2 functions utilizing camera and radar sensors are state of the art. Usually Level 2 capable vehicles are equipped with four SRR sensors (two in the front and two in the back) integrated behind the painted bumper and one

MRR sensor located at the front behind a radome structure. This configuration enables BSD with the SRR sensors located at the back as well as AEB using the sensors at the front. For Level 3 functions additional sensors are necessary. Besides the optional integration of a lidar sensor, also the amount of radar sensors is increasing. A possible configuration would be the addition of two SRR sensors located at the side skirt under the B-Pillar as well as two additional FRRs in the back. The frontal MRR is upgraded to a FRR. As mentioned before, the FRR covers a larger range than a MRR sensor and has an increased angular resolution. Thus this sensor is more suitable for Level 3 functions. The two additional FRR sensors in the back allow monitoring of the traffic behind the vehicle over a large range. This would allow for automated lane change assist recognizing fast approaching vehicles from behind. The additional two SRR sensors in the side skirts allow to cover a larger area around the vehicle. As a result, even smaller obstacles such as a motorcycle driving side by side can be recognized by the vehicle. Without these two additional sensors, the motorcycle could be driving in a blind spot. This scenario is especially dangerous for driving on a narrow curvy road. Without the additional SRR sensors intersecting the path of a small object like a motorcycle is very likely. A graphical representation of the two configurations for Level 2 and 3 can be found in Fig. 1.1.
Unlike lidar and camera, for radar there is the possibility to integrate the sensor behind plastic parts. This hidden integration is favourable from a design perspective, especially considering the high amount of radar sensors integrated into a single vehicle. Unlike SRR, which are already integrated behind plastic bumpers (see Fig. 1.2), MRR and FRR are integrated behind radomes. The complexity of a radome is directly coupled to the design. There are relatively simple radomes consisting of a single layer plastic structure including heating wires as well as multilayer radomes with different types of coatings. An example of a single layered radome with and without structure can be seen in Fig. 1.3.

Figure 1.2: Cut away of SRR sensor integrated behind the painted bumper in the back.

(a) (b)

Figure 1.3: a) Radome of MRR for BMW iX3 located in the lower air intake b) BMW i4 radome with structure to match the design of the grill.

Design radomes are much more complex and consist of multiple layers of paint plastic and heating wires. Usually the painted layer is extremely thin in order to make the radome radar transparent and also allowing a much more sophisticated integration into the design of the vehicles. The layer is applied utilizing a Physical Vapor Deposition (PVD) process [5]. In order to achieve a high opacity with a very thin layer materials like indium are used. Examples for design radomes can be seen in Fig. 1.4.

(a) (b)

Figure 1.4: a) Multilayered Radome of BMW iX. b) Multilayered BMW 2 series integrated into the kidney grill. The middle part of the radome consists of a thin layer of indium in order to match the overall design.

The main goal of designing a multilayered radome lies within choosing the right thickness for each layer in order to achieve a high radar transparency. By adjusting the thickness of each layer, a low reflection and a high transmission for electromagnetic waves can be achieved for the desired frequency range.

1.2 Goal and Structure of this Work

The hidden integration of radar sensors behind radomes or painted bumper has been of interest since radar sensors have became an essential part of the vehicle. Especially the feasibility of integrating radar sensors behind radome structures and possible influences were investigated in literature. In [6] radome structures are analyzed in great detail. The study includes influences of environmental circumstances such as water or ice films on the radome as well as coatings. The studies regarding automotive coatings included a first dielectric characterization utilizing the relative permittivity as a descriptive quantity for radar transparency. Moreover, the influence of structural elements in the radome, is investigated. For possible future radar sensors operating at frequencies between 77 - 81 GHz comprehensive research for lowering possible reflections were conducted in [7]. The goal of this thesis is to quantify known effects experimentally as well as investigating yet unknown effects.T he latter category includes the influence of application techniques on radar transparency. Furthermore, the influence of different titanium dioxide (TiO_2) concentrations is investigated. In order to evaluate possible exclusion criteria for a hidden integration behind painted plastic parts, direct influences on the sensor performance such as angular deviations and separation of objects are investigated. This thesis is structured as follows: In Chapter 2 the working principle of automotive radar sensors is explained, including the requirements of ADAS and AD towards radar. Influences of material and coatings on radar performance are outlined as well. The method developed in the course of this thesis to characterize the dielectric behavior of automotive coatings is presented in Chapter 3. In addition, the radar transparency of different plastic substrates is evaluated. In Chapter 4 a detailed study is conducted to evaluate the influence of application techniques of automotive coatings on radar transparency. Also, the best suited technique for radar is evaluated. Using a dedicated test setup the influence of coatings on the radar performance is investigated in Chapter 5. Similar measurements are conducted using samples painted with different TiO_2 concentrations in Chapter 6.

CHAPTER 2

Automotive Radar

This chapter provides an overview of the working principle of radar sensors used in the automotive sector. Furthermore, the requirements of ADAS and AD towards radar are outlined. All the requirements are derived from typical ADAS scenarios. Since this thesis is dedicated to influences of automotive coatings and the associated hidden integration of sensors on radar, sources of performance degradations are highlighted.

2.1 Radar Equation

The main working principle of a radar sensor is based on electromagnetic waves getting transmitted and received. If the transmitted waves hit a target, they are reflected back to the sensor, which in return can detect the target if the reflected energy is sufficient. By comparing quantities such as time, frequency or phase of the transmitted and received signal, certain properties of the target can be determined. These include distance, velocity and angle relative to the sensor. Considering a simple radar sensor consisting of one receiving (RX) antenna and one transmitting (TX) antenna, the power density of the transmitted signal is written as:

$$S_{\mathrm{tx}}(R_{\mathrm{t}}) = \frac{P_{\mathrm{tx}} G_{\mathrm{tx}}}{4\pi R_{\mathrm{t}}^2}, \tag{2.1}$$

where P_{tx} denotes the power of the TX antenna, G_{tx} the gain of the TX antenna and R_{t} the distance from the transmitter to the target. The power density reflected from the target at the distance R_{r} is parameterized by

$$S_{\mathrm{ref}}(R_{\mathrm{r}}) = \frac{P_{\mathrm{ref}}}{4\pi R_{\mathrm{r}}^2} = \frac{\sigma_{\mathrm{s}} S_{\mathrm{tx}}(R)}{4\pi R_{\mathrm{r}}^2}. \tag{2.2}$$

In this equation P_{ref} describes the reflected power, σ_{s} the Radar Cross Section (RCS) and $S_{\mathrm{tx}}(R)$ the power density of the transmitting antenna evaluated at the target with

the distance R. Combining the equations above yields the received power assuming that TX and RX antenna are at the same position

$$P_{\mathrm{rx}} = S_{\mathrm{ref}}(R) \cdot A_{\mathrm{r}} = \frac{\sigma_{\mathrm{s}} P_{\mathrm{tx}} G_{\mathrm{tx}} G_{\mathrm{rx}} \lambda^2}{(4\pi)^3 R^4}. \tag{2.3}$$

This equation is commonly referred to as the radar equation. It should be noted that this equation describes the ideal lossless case. However, this equation shows the general relation between the transmitting and receiving power. Often, this equation is also written as a function of the distance R as [8]

$$R = \sqrt[4]{\frac{P_{\mathrm{tx}} G_{\mathrm{tx}} \lambda^2 A_{\mathrm{r}} \sigma_{\mathrm{s}}}{(4\pi)^3 P_{\mathrm{rx}}}}, \tag{2.4}$$

with $A_{\mathrm{r}} = G_{\mathrm{tx}} \lambda^2 / 4\pi$ describing the effective aperture of the receiving antenna. The radar equation shows that the range is proportional to the fourth root of the transmitting power P_{tx}. With this equation the maximum detectable range can be easily estimated [4].

2.2 FMCW Radar Systems

In general there are many types of radar sensors, which can be divided into the different waveforms such as pulsed and continuous. Each kind has certain benefits and drawbacks. Pulsed waveforms can use the same antenna for transmitting and receiving the signal and can output short powerful transmit pulses. However, these type of radars suffer from blind ranges which are a result of the radar being blind for the duration of the transmitted pulse. On the other hand, radars utilizing the Continuous Waveform (CW) need a separate transmitter and receiver. Moreover, there are constraints by power limits due to isolation limitations between the RX and TX antenna [4]. Another drawback of CW radars is given by the fact that they can not provide a range information [9]. High power combined with insufficient isolation will result in leakage of the transmitter signal into the receiver [10]. In general the choice of waveform contributes to the radar system performance metrics, such as the Signal to Noise Ratio (SNR), range and Doppler resolution as well as their ambiguities [11]. For FMCW radar sensors there are several variations including Linear Frequency-Modulated CW (LFMCW), Stepped FMCW and Interrupted FMCW. For the investigations conducted in this thesis, a FMCW radar utilizing the fast chirp ramp sequence waveform is used. This waveform avoids mispairing effects which FMCW radar sensors are suffering from. This effect results in wrong range or velocity estimations in an environment including multiple targets. The fast chirp ramp sequence can solve this problem by determining the range and velocity without pairing [4].

2.2.1 Fast Chirp Ramp Sequence Waveform

The main idea behind the fast chirp ramp sequence waveform is to send multiple consecutive frequency ramps as shown in Fig. 2.1. The following shows a derivation for the

beat frequency f_b. With this frequency quantities such as the maximum range, velocity and its resolution can be estimated. Starting at a carrier frequency f_c, the frequency can be expressed at the time t as [12]

$$f(t) = f_\mathrm{c} + \frac{B}{T}t = f_\mathrm{c} + \mu t, \tag{2.5}$$

where B describes the bandwidth, T the duration of the sweep and μ the chirp rate. The phase ϕ(t) can be obtained using

$$\frac{\mathrm{d}\phi(t)}{\mathrm{d}t} = 2\pi f(t) \tag{2.6}$$

and integrating this expression over the time t to obtain

$$\phi(\mathrm{t}) = 2\pi \int_0^t f(t)\mathrm{d}t = 2\pi \left(f_\mathrm{c} t + \frac{\mu t^2}{2} \right) + \phi_0, \tag{2.7}$$

where ϕ_0 describes the initial phase. Neglecting the initial phase, the transmitted signal can be expressed with an amplitude A_tx as

$$x_\mathrm{tx}(t) = A_\mathrm{tx}\cos\left(2\pi f_\mathrm{c} t + \frac{\pi\mu}{2}(t - nT)^2\right), \tag{2.8}$$

where n is the corresponding chirp ramp. The reflected signal from a target will reach the sensor after a certain delay τ. Considering a target at a distance R and a velocity v, the delay can be expressed as

$$\tau = \frac{2(R + vt)}{c_0}, \tag{2.9}$$

where c_0 denotes the speed of light in the vacuum. With this relation the received signal x_rx can be formulated similar to the transmitted signal as

$$x_\mathrm{rx}(t) = A_\mathrm{rx}\cos\left(2\pi f_\mathrm{c}(t - \tau) + \frac{\pi\mu}{2}(t - \tau - nT)^2\right). \tag{2.10}$$

After passing the mixer (as shown in Fig. 2.2), the signal can be written as follows

$$x_\mathrm{m}(t) = x_\mathrm{tx}(t) \cdot x_\mathrm{rx}(t) \tag{2.11}$$

$$= A_\mathrm{tx}\cos\left(2\pi f_\mathrm{c} t + \frac{\pi\mu}{2}(t - nT)^2\right) \cdot A_\mathrm{rx}\cos\left(2\pi f_\mathrm{c}(t - \tau) + \frac{\pi\mu}{2}(t - \tau - nT)^2\right) \tag{2.12}$$

$$= \frac{A_\mathrm{tx} + A_\mathrm{rx}}{2}\Big(\cos\left(2\pi f_\mathrm{c} t + \frac{\pi\mu}{2}(t - nT)^2 + 2\pi f_\mathrm{c}(t - \tau) + \frac{\pi\mu}{2}(t - \tau - nT)^2\right)$$
$$+ \cos\left(2\pi f_\mathrm{c} t + \frac{\pi\mu}{2}(t - nT)^2 - 2\pi f_\mathrm{c}(t - \tau) + \frac{\pi\mu}{2}(t - \tau - nT)^2\right)\Big). \tag{2.13}$$

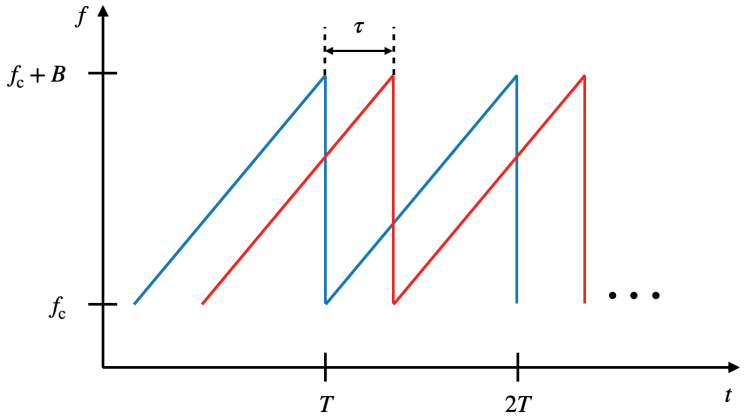

Figure 2.1: Saw tooth pattern of a chirp sequence for a non moving object. The transmitted chirp is colored blue, the received chirp red. Both chirps are separated by a certain time delay τ. Each chirp has a duration T and a frequency corresponding to the bandwidth B.

After the mixer, the signal passes a low pass filter, cutting the high frequency parts of (2.2.1). Assuming the amplitudes to be normalized, the signal reads

$$x_{\mathrm{b}}(t) = \frac{1}{2}\cos\left(2\pi f_{\mathrm{c}}\tau + 2\pi\mu\tau(t - nT) - \pi\mu\tau^2\right). \tag{2.14}$$

This signal is often referred to as the beat signal. Reinserting the delay τ from (2.9) leads to

$$x_{\mathrm{b}}(t) = \frac{1}{2}\cos\left(2\pi f_{\mathrm{c}}\frac{2(R+vt)}{c_0} + 2\pi\mu\frac{2(R+vt)}{c_0}(t - nT) - \pi\mu\left(\frac{2(R+vt)}{c_0}\right)^2\right). \tag{2.15}$$

The third term of this expression is neglectable since $c_0^2 >> (R+vt)^2$, resulting in

$$x_{\mathrm{b}}(t) = \frac{1}{2}\cos\left(2\pi f_{\mathrm{c}}\frac{2(R+vt)}{c_0} + 2\pi\mu\frac{2(R+vt)}{c_0}(t - nT)\right) \tag{2.16}$$

$$= \frac{1}{2}\cos\left(\frac{2\pi}{c_0}\left(2Rf_{\mathrm{c}} + 2f_{\mathrm{c}}vt + \left(2R\mu t - 2R\mu nT + 2\mu vt^2 - 2n\mu vtT\right)\right)\right). \tag{2.17}$$

This equation can be rewritten considering the start time $t = (t_\mathrm{s} + nT)$ for the n-th ramp

$$\begin{aligned} x_\mathrm{b}(t_\mathrm{s}) &= \frac{1}{2}\cos\Big(\frac{2\pi}{c_0}\big(2Rf_\mathrm{c} + 2f_\mathrm{c}v(t_\mathrm{s}+nT) + \big(2R\mu(t_s+nT) \\ &\quad - 2R\mu nT + 2\mu v(t_\mathrm{s}+nT)^2 - 2n\mu v(t_\mathrm{s}+nT)T\big)\big)\Big) \qquad (2.18) \\ &= \frac{1}{2}\cos\Big(\frac{2\pi}{c_0}\big(2Rf_\mathrm{c} + 2f_\mathrm{c}v(t_\mathrm{s}+nT) + \big(2R\mu(t_\mathrm{s}+nT) \\ &\quad - 2R\mu nT + 2\mu v(t_\mathrm{s}^2 + 2nt_\mathrm{s}T + n^2T^2) - 2n\mu v(t_\mathrm{s}+nT)T\big)\big)\Big). \qquad (2.19) \end{aligned}$$

By neglecting any second order terms and reintroducing the bandwidth, the term can also be expressed as

$$x_\mathrm{b}(t_\mathrm{s}) = \frac{1}{2}\cos\left(\frac{2\pi}{c_0}\left(2Rf_\mathrm{c} + 2vnTf_\mathrm{c} + (2R\mu + 2cf_\mathrm{c} + 2nBv)\,t_\mathrm{s}\right)\right). \qquad (2.20)$$

A last simplification can be made by neglecting the first term, which reflects a constant phase resulting in

$$\begin{aligned} x_\mathrm{b}(t_\mathrm{s}) &= \frac{1}{2}\cos\left(2\pi\left(\frac{2vnTf_\mathrm{c}}{c_0} + \frac{(2R\mu + 2vf_\mathrm{c} + 2nBv)\,t_\mathrm{s}}{c_0}\right)\right) \qquad (2.21) \\ &= \frac{1}{2}\cos\left(2\pi\left(nT\frac{2vf_\mathrm{c}}{c_0} + \left(\frac{(2R\mu)}{c_0} + \frac{(2vf_\mathrm{c})}{c_0} + \frac{(2nBv)}{c_0}\right)t_\mathrm{s}\right)\right) \qquad (2.22) \\ &= \frac{1}{2}\cos\left(2\pi\left(nTf_\mathrm{d} + (f_\mathrm{b} + f_\mathrm{d} + f_\mathrm{m})\,t_\mathrm{s}\right)\right), \qquad (2.23) \end{aligned}$$

where f_d is the Doppler frequency, f_b the beat frequency caused by the delay between the transmitted and received signal and f_m is the frequency introduced by motion of the target during sweeps. Since the time of a sweep is generally very small, this frequency part can be neglected.

2.2.2 Signal Processing

After the beat signal is converted by an Analog-to-Digital Converter (ADC), the signal is processed further to estimate quantities such as range, velocity and angle of one or multiple targets. In order to extract these information a Fast Fourier Transformation (FFT) is applied to the beat signal x_{t_s}. The Fourier transformation in the frequency domain can be written as

$$X(f) = \frac{1}{4}\left(\left(e^{i2\pi nTf_\mathrm{d}}\right)\delta(f - f_\mathrm{b}) + \left(e^{-i2\pi nTf_\mathrm{d}}\right)\delta(f + f_\mathrm{b})\right). \qquad (2.24)$$

The beat frequency f_b can be extracted directly from the peak of the FFT spectrum. The distance between radar and the target is estimated since the range can be expressed using the beat frequency as

$$R = \frac{c_0 f_\mathrm{b}}{2\mu}. \qquad (2.25)$$

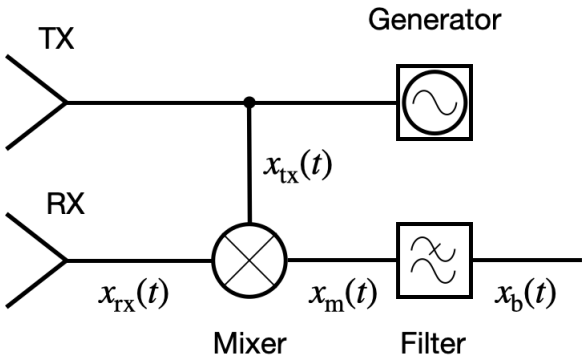

Figure 2.2: Block diagram of a FMCW radar. $x_{\mathrm{tx}}(t)$,$x_{\mathrm{rx}}(t)$ refers to the transmitted or received signal respectively. $x_{\mathrm{m}}(t)$ is the signal after processed by the mixer and $x_{\mathrm{b}}(t)$ is the beat signal.

The range resolution directly depends on the length of the ramp of the chirp and therefore on the bandwidth B and can be written as

$$\Delta R = \frac{c_0}{2B}. \tag{2.26}$$

The maximum theoretical range of the radar depends on the number of sampling points N_{s} used as an input for the FFT and can be formulated as

$$R_{\mathrm{max}} = \frac{c_0 N_{\mathrm{s}}}{4B}. \tag{2.27}$$

Since for the range the information of a single chirp is used, this is also often revered to as "fast time". The "slow time" on the other hand utilizes the information of all chirps and is therefore evaluated for every single frame. By extracting the phase of the peak of the FFT spectrum the Doppler frequency f_{d} can be obtained and thus the corresponding velocity

$$v = \frac{c_0 f_{\mathrm{d}}}{2f_{\mathrm{c}}}. \tag{2.28}$$

Since the velocity uses the information of the number of ramps N_{r} of each frame, the resolution also depends on the latter one

$$\Delta v = \frac{c_0 \Delta f_{\mathrm{d}}}{2f_{\mathrm{c}}} = \frac{c_0}{2f_{\mathrm{c}} N_{\mathrm{r}} T}. \tag{2.29}$$

According to the Nyquist-Shannon sampling theorem [13], a signal can be recovered if the sampling rate exceeds the highest frequency by a factor of two. Otherwise frequency aliasing will be present [14]. As a result, the maximum Doppler frequency is given by $f_{\mathrm{dmax}} = 1/2T$ and therefore the maximum velocity can be obtained

$$v_{\mathrm{max}} = \frac{c_0}{4f_{\mathrm{c}} T}. \tag{2.30}$$

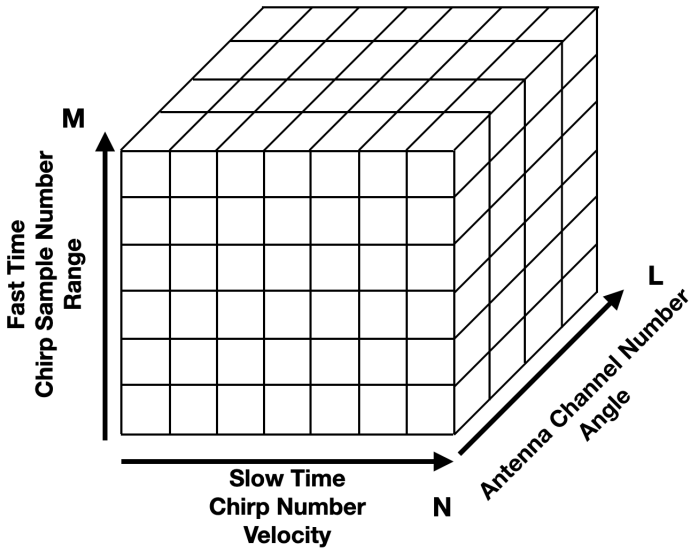

Figure 2.3: Radar data cube including the information of range, velocity and angle. The desired quantity can be obtained by using FFTs over the corresponding dimension N, M, L.

The FFTs used to extract information about range and velocity are referred to as range-FFT and Doppler-FFT respectively. The ADC data of the chirps is stored in a matrix corresponding to the dimensions M and N of the data cube displayed in Fig. 2.3. The FFT over each column can resolve objects in range, where the FFT over each row can be used for resolving objects in velocity. Apart from range and velocity, FMCW radar systems can also determine the so called Angle of Arrival (AoA) of the target by utilizing at least two RX antennas. The small change in distance results in a phase change which can be used to estimate the AoA. However, using only two RX antennas can not resolve the AoA for objects with the same distance and velocity relatively to the sensor. Therefore, using more than two RX antennas is favourable. In the following, it is assumed that the arriving waves are plane, which is valid if the source is located in the far field [15]. This assumption is satisfied for distances greater than the so called Fraunhofer distance, which can be written as [16]

$$R_F = \frac{2D^2}{\lambda}, \tag{2.31}$$

where D describes the dimension of the antenna or antenna array. For plane waves, the phase difference from one to another RX antenna can be written as

$$\Delta\phi = \frac{2\pi d \sin(\theta) f_\mathrm{c}}{c_0} = \frac{2\pi d \sin(\theta)}{\lambda}, \tag{2.32}$$

where d is the distance between two RX antennas and θ is the AoA. The term $d\sin(\theta)$ describes the additional distance compared to a RX antenna closer to the target, as

shown in Fig. 2.4. Since the dependency between the phase difference $\Delta\phi$ and the AoA θ is not linear, the sensitivity decreases with the angle. Therefore, the sensitivity reaches its maximum when the target is located boresight at $\theta = 0$. It should be noted that there is a an ambiguity in measuring phase differences exceeding an interval of $[-\pi, \pi]$ caused by the fact that phases shifted outside the interval by 2π can not be distinguished from phases within the interval. Therefore, the maximum determinable AoA can be calculated using following relation

$$\theta_{\max} = \sin^{-1}\left(\frac{\lambda}{2d}\right). \tag{2.33}$$

Choosing $\lambda/2$ as the distance between the RX antennas, results in a maximum determinable AoA of $\pm 90°$. The maximum determinable AoA should not be confused with the Field of View (FoV) originating from the directivity of the antenna. In order to derive an expression for the angular resolution, two targets separated by the angle $\Delta\psi$ are considered. The phase difference $\Delta\psi$ between the two targets can be written as

$$\Delta\psi = \frac{2\pi d(\sin(\theta + \Delta\theta) - \sin(\theta))}{\lambda}. \tag{2.34}$$

Since the smallest possible angle where the objects still can be separated is of interest, (2.34) can be approximated by

$$\lim_{\Delta\theta \to 0} \Delta\psi = \frac{2\pi d\cos(\theta)\Delta\theta}{\lambda}, \tag{2.35}$$

where for the last step, the following is used

$$\lim_{\Delta\theta \to 0} \frac{(\sin(\theta + \Delta\theta) - \sin(\theta))}{\Delta\theta} = \cos(\theta). \tag{2.36}$$

Taking the number of RX antennas N_{RX} into account one can write

$$\frac{2\pi d\cos(\theta)\Delta\theta}{\lambda} > \frac{2\pi}{N_{\mathrm{RX}}} \tag{2.37}$$

$$\iff \Delta\theta > \frac{\lambda}{N_{\mathrm{RX}} d\cos(\theta)}, \tag{2.38}$$

which leads to the expression for the angular resolution

$$\theta_{\mathrm{res}} = \frac{\lambda}{N_{\mathrm{RX}} d\cos(\theta)}. \tag{2.39}$$

With a spacing of $\lambda/2$ between the RX antennas and assuming the targets are located at $\approx 0°$ the resolution can be simplified and approximated as $\theta_{\mathrm{res}} = 2/N_{\mathrm{RX}}$. The achievable angular resolution depends directly on the amount of used RX antennas and the spacing. Therefore, a large aperture is needed for a high resolution. Although a high resolution can be achieved with just 2 RX antennas with sufficient enough spacing, more antennas reduce ambiguities when estimating the AoA of multiple targets. The

individual information of each antenna is stored in the third dimension building the three dimensional data cube displayed in Fig. 2.3 together with the data of the chirps. The angle can then be estimated by applying the FFT on the corresponding peak across all antennas utilizing the previously calculated two dimensional FFT grid of the chirps. Besides the conventional way to estimate the AoA, there are also high resolution methods such as MUSIC [17] or ESPRIT [18]. Since these methods are not used in the framework of this thesis, they are just mentioned for completeness sake.

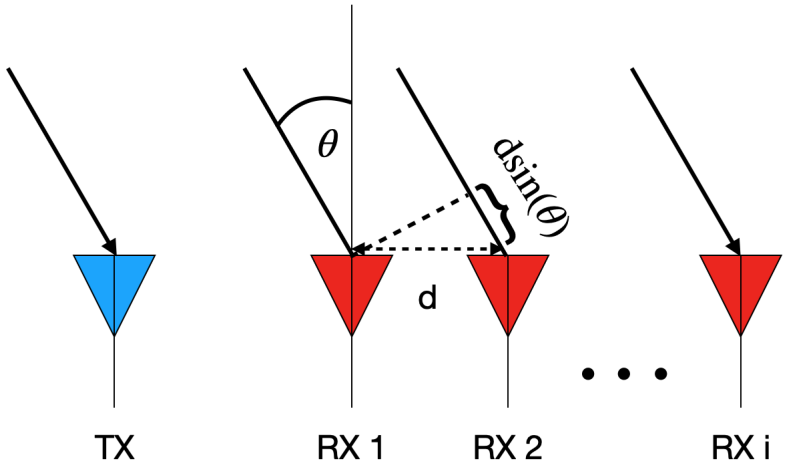

Figure 2.4: Antenna array with one TX and i RX antennas. The Angle of Arrival (AoA) can be estimated by exploiting the phase difference of the wavefront between multiple RX antennas.

2.2.3 MIMO Radar

A Multiple Input Multiple Output (MIMO) radar can be seen as a further development of the idea of a phased array radar. Phased arrays are capable of steering the energy towards a desired direction as well as being coherent by utilizing multiple TX and RX antennas. This is achieved by transmitting waveforms with the right scaling and delay [19]. A MIMO radar also consists of multiple TX and RX antennas. However, unlike the phased array the waveforms can be correlated or uncorrelated [20]. A MIMO radar using correlated antennas for virtual enlargement of the aperture reaches a higher angular resolution while retaining compactness [21] [22]. Additional benefits are the possibility to increase the sensibility to detect slow moving targets as well as better parameter identifiability [20]. In addition to theses benefits, a MIMO radar can utilize so called virtual antenna arrays. In general there are MIMO radars with separated antennas [23] and colocated antennas [20]. In the automotive sector, MIMO radars use colocated antennas. Usually the antennas are spaced in the magnitude of the operating wavelength. By combining the information of the path of the TX and RX antennas, the angular res-

olution can be increased. Exploiting the different time delays and phase shifts, multiple beams can be formed by combining them coherently. In addition, a great flexibility is provided for modeling the transmitted beampattern [19]. An example of a virtual antenna array created by 2 TX and 3 RX antennas spaced 2λ and $\lambda/2$ respectively can be seen in Fig. 2.5. This example shows the possibility to increase the angular resolution in azimuth. It is also possible to arrange the antennas in a stair pattern to simultaneously increase the resolution in elevation.

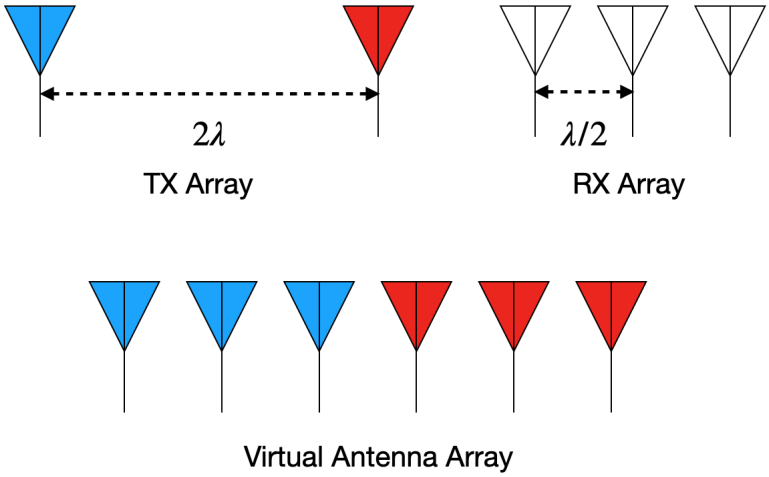

Figure 2.5: Scheme of virtual antenna array created by 2 TX and 3 RX antennas.

2.3 Requirements of Driver Assistance and Autonomous Driving Towards Radar

The performance of a radar used for ADAS and autonomous driving strongly depends on the requirements of the desired functions. Besides requiring a certain robustness against environmental conditions such as low and high temperatures as well as water ingress into the sensor, there are also requirements towards range, detectable velocity, angular resolution and the possible field of view. Currently SRR sensors are used for a range up to 110 m, while for FRR a range of 300 m is needed. According to (2.4), the maximum range scales with the fourth root of the transmitted power. Therefore, the range can be increased by increasing the power. On the signal processing side, the maximum unambiguously range depends on the sampling rate according to (2.27). The actual maximal range strongly depends on the size of the memory, since it is limited by the product of the range resolution times the number of chirps. As a result, a larger memory size can increase the maximum detectable range. Besides the maximum range, also the range resolution is important, which depends on the bandwidth used for the sweep of the chirp, as shown in (2.26). Since the radar sensors are currently operating

between 76 - 77 GHz, the theoretical highest achievable range resolution is limited to 0.15 m. Since SRR and FRR sensors are operating simultaneously, there might be the risk of interference. By using different ranges of the bandwidth, this problem can be avoided. A scenario would be that SRR sensors use the lower half and FRR the upper half of the 1 GHz bandwidth. However, this limits the range resolution and is therefore not ideal. Another approach delays the signal of the different sensors so that only one sensor group operates at once. Usually sensors located at opposite sides are operated simultaneously, e.g. a SRR located in the front bumper at the left side and a SRR located in the back on the right side. This approach makes the whole bandwidth usable without risking interference. The maximum range resolution is crucial for SRR as well as for FRR sensors. Even though FRR operates up to 300 m a high range resolution is necessary to identify precisely the end of a traffic jam.
For velocity estimations the requirements mainly depend on the speed the functions are available as well as the delta velocity between the ego vehicle and other road participants. Usually the maximum velocity is set to 250 km/h. The maximum theoretical detectable velocity depends on the maximum Doppler frequency and therefore on the sweep duration (2.2.2). A smaller sweep duration leads to a higher detectable velocity. Similar to the maximum range resolution, the maximum detectable velocity depends on the memory size. In general, a high resolution of the velocity is necessary to separate objects using a high Doppler resolution. The higher the resolution of the velocity, the more objects can be separated. Also differentiating slowly moving targets from standing targets is only possible with a high velocity resolution. Typical values for state of the art automotive radar sensors are 0.1 m/s - 0.5 m/s. The resolution of the velocity depends on the number of ramps per frame and is enhanceable with increasing number following (2.29).
While the range and velocity capabilities depend on the configuration on both, hardware and software side, angular resolution and the maximum angular FoV mainly depend on hardware. The maximum resolution is given by (2.37) and therefore depends on the spacing between the RX and TX antenna. Increasing the spacing between the antennas increases the capability of resolving smaller angles. In order to increase the amount of unambiguously identifiable targets, the number of antennas also needs to increase. Especially for FRR sensors, capable of measuring great distances, a high angular resolution is necessary. According to (2.33), the achievable maximum AoA is given by the spacing of between the RX antennas. Choosing the spacing as $\lambda/2$ enables a theoretical maximum AoA of $\pm 90°$. In addition to the theoretical AoA, the FoV is mainly determined by the antenna design. Choosing the appropriate antenna design, the FoV can be wider or narrower. In general SRR sensors feature a generally large FoV to cover an area around the car as large as possible. FRRs on the other hand, have a narrow FoV, since they are used for functions such as ACC. In addition, in a narrow FoV more transmitting power can be concentrated into a small areas. Therefore, the achievable range can benefit from a narrow FoV.

2.4 Possible Performance Degradation caused by Hidden Sensor Integration

Integrating radar sensors behind painted plastic parts can degrade the radar performance in many ways. There are multiple factors to be considered, such as the thickness, the number of layers and the dielectric behavior. The dielectric behavior can be characterized by the relative permittivity ϵ_r. A high permittivity leads to a loss in the transmitted signal, reducing the sensitivity of the radar. A high damping leads to a SNR, where objects in larger distances might not be detectable anymore due to a signal being weaker than the overall noise. The influence of a the damping on the range can be seen by considering the lossy case of (2.4), expressed as

$$R = \sqrt[4]{\frac{P_{\mathrm{tx}} G_{\mathrm{tx}} G_{\mathrm{rx}} \lambda^2 \sigma_{\mathrm{s}}}{(4\pi)^3 P_{\mathrm{rx}} L_{\mathrm{total}}}}, \tag{2.40}$$

where L_{total} denotes all losses including internal, external as well as losses caused by the radome or painted bumper (referred to as cover in the following). Since all losses except the one caused by the cover stay the same, the ratio of the range with and without integration behind a cover can be written as [6]

$$\frac{R_{\text{with cover}}}{R_{\text{without cover}}} = (L_{\mathrm{cover}})^{-1/4}. \tag{2.41}$$

Since the transmitted signal passes the cover two times (transmitted and reflected signal), the loss is referred to as two-way loss. Considering a 3 dB loss, which corresponds to a double of the loss caused by the cover L_{cover}, the maximum detectable range decreases by 15.9 % [6]. Considering a FRR range of 300 m, the range would decrease to 252 m, which would drastically impact the ACC functionality. It should be noted that this consideration is valid for an object which is just barely detectable due to the corresponding SNR level. Therefore, the transmission loss should be kept as low as possible. Besides impacting the maximum range, a deviation can occur when estimating the AoA by altering the phase of the wavefront. In general the dielectric behavior of a material is correlated with its refractive index and therefore with the permittivity and the permeability [24]. For radomes and painted bumpers, the permeability is neglectable, since they are considered to be non magnetic. A high permittivity leads to a high refraction of the wave at the boundary layer. Considering a vertically polarized electromagnetic wave, the reflection can be written according to the Fresnel equation as [25]

$$\rho_{\perp} = \frac{n_1 \cos(\alpha) - \frac{\mu_{r,1}}{\mu_{r,2}} n_2 \cos(\beta)}{n_1 \cos(\alpha) + \frac{\mu_{r,1}}{\mu_{r,2}} n_2 \cos(\beta)}, \tag{2.42}$$

where $\mu_{r,i}$ refers to the relative permeability of the corresponding layer and α and β to the angle of incidence and refraction. This equation can be simplified further for a radome or painted bumper. Since all materials including the substrate and the coating are non magnetic, the relative permeability can be considered as $\mu_r = 1$. Snell's law

can be used to make the equation only dependent on the incidence angle. Moreover, the refractive indices can be expressed using the relative permittivity with $n = \sqrt{\epsilon_r \mu_r}$, simplifying (2.42) to

$$\rho_\perp = \frac{\left(\cos(\alpha) - \sqrt{\frac{\epsilon_{r,2}}{\epsilon_{r,1}} - \sin^2(\alpha)}\right)^2}{1 - \frac{\epsilon_{r,2}}{\epsilon_{r,1}}}. \tag{2.43}$$

In case of an incidence angle $\alpha = 0°$, which holds true for a cover perpendicular to the signal of the sensor, the equation can by simplified further to

$$\rho = \rho_\perp = \rho_\parallel = \frac{\left(1 - \sqrt{\frac{\epsilon_{r,2}}{\epsilon_{r,1}}}\right)^2}{1 - \frac{\epsilon_{r,2}}{\epsilon_{r,1}}}. \tag{2.44}$$

This equation shows that the higher the jump in the relative permittivity of the second medium compared to the first medium, the higher the reflection. This holds especially true for radomes and painted bumpers, since the basecoats have a very high permittivity compared to the substrate. The reflection of different coatings with the same thickness but increasing permittivity is shown in Fig. 2.6. For this simulation a structure similar to a car bumper is considered consisting of a polypropylene substrate, basecoat and clearcoat. The incident wave is perpendicular to the backside of the bumper. The model used for the simulation is described in Section 3.5. It can be seen that an increasing permittivity not only increases the reflection but also shifts the resonance and therefore can be used to design a resonant cover for the radar sensor. More details on coatings itself and the resonant design can be found in Chapter 3.

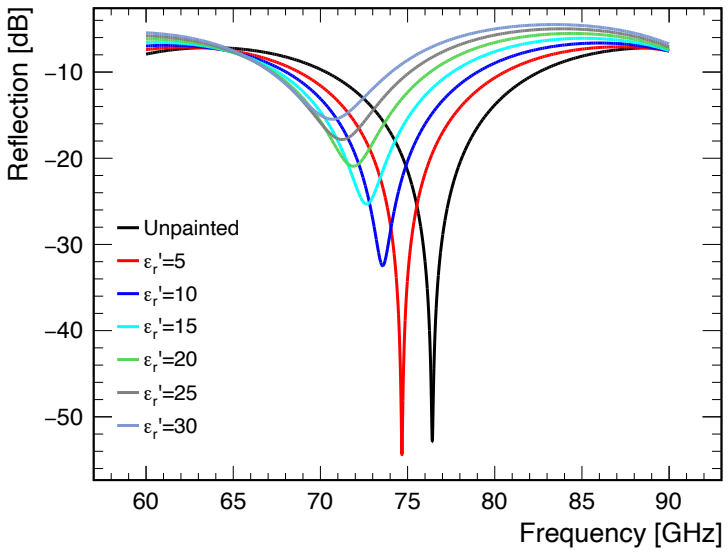

Figure 2.6: Change of the reflection for simulated bumpers with different coatings with increasing real part of permittivity $\varepsilon_r^{'}$. The black line refers to the unpainted bumper substrate.

The main impact on the AoA is caused by a reflection on the inside of the cover. As a result, depending on angle of the cover, a standing wave can occur between the sensor and the cover. These standing waves can result in an interference with the signal reflected from the actual target, resulting in a change of the phase of the wave and therefore the AoA. In the following the amplitude and phase difference caused by an interference of N waves is derived, which is used to describe a multiple reflection scenario between the sensor and the cover. The derivation is mainly based on [25] and [26], where also more details can be found. The waves are considered to have the same frequency ω, which is the case for the present scenario. Furthermore, it is assumed that all waves propagate in the same direction. The sum of the waves can be written as a function of the amplitude $A_{0,i}$ and the phase ϕ_i of the i-th wave as

$$A = \sum_{i=1}^{N} A_{0,i}\cos(\phi_i \pm \omega t), \tag{2.45}$$

In order to obtain an expression for the amplitude A_0 and the phase ϕ of the superimposed waves, following relations can be used:

$$A_0\cos(\phi) = \sum_{i=1}^{N} A_{0,i}\cos(\phi_i) \tag{2.46}$$

$$A_0\sin(\phi) = \sum_{i=1}^{N} A_{0,i}\sin(\phi_i). \tag{2.47}$$

By adding the two equations above and taking the square, an expression for the resulting amplitude can be obtained

$$A_0 = \sqrt{\sum_{i=1}^{N} A_{0,i}^2 + 2\sum_{j>i}^{N}\sum_{i=1}^{N} A_{0,i}A_{0,j}\cos(\phi_i - \phi_j)}, \tag{2.48}$$

where the second term is caused by the inference depending on the phase differences of the interfering waves. A division on the other hand yields the phase

$$\phi = \arctan\left(\frac{\sum_{i=1}^{N} A_{0,i}\sin(\phi_i)}{\sum_{i=1}^{N} A_{0,i}\cos(\phi_i)}\right). \tag{2.49}$$

As shown, the interference can cause a phase shift, which influences the estimation of the AoA. The amplitude and therefore the signal strength might change by constructive or destructive interference. However, the latter effect is too small and therefore neglectable. In addition to a change of the phase caused by interference, also inhomogeneities in the substrate or coating can cause a deviation in estimating the AoA. Since the phase changes when the wave penetrates a material, inhomogeneities cause different phase shifts due to different thicknesses. A typical example for this would be a radome which changes its thickness within the FoV of the sensor. Especially for painted parts a homogenous

application of the coating is therefore crucial. Even though the thickness of the coating is relatively small compared to the substrate itself, the high permittivity of the coating can have a strong impact. Since a dedicated calibration of the sensor for every single produced part is very unpractical in a series production, the substrate and the coating should be as homogenous in thickness as possible.
Multiple reflections between the sensor and the target can theoretically influence range estimations indirectly. One scenario would be that the wave reflects back from the target and afterwards between the sensor and the inside of the radome. As a result, a second artificial target can be seen behind the actual target. The distance between these two target corresponds to the distance between sensor and radome and how often the wave reflects between those two. Since the range resolution of a radar with 1 GHz bandwidth is 0.15 m, the real and artificial target fall within in the same range bin and therefore is considered to be unproblematic. Furthermore, multiple reflexions between the sensor and the target can occur. This type of reflexion results in equally spaced targets, where the spacing corresponds to the original distance between sensor and target. In order to recognize such targets as artificial, further data processing within the tracker is necessary.

2.5 Influence of Polarization

For radomes, it is common practice to mount them at a certain tilting angle relatively to the sensor to reduce the reflections between sensor and radome. In addition, for painted plastic bumpers such effects can play a key role, when designing a radar transparent part. The reflection and transmission strongly depends on the polarization of the wave for incidence angles, which are not perpendicular. In general, this effect is similar to the Brewster angle in optics, where the light can penetrate a dielectric surface without reflection under a certain angle and polarization. The angle leads to an annihilation of the parallel component of the electric field vector relatively to the surface of incidence. This leads to a linear polarization of the reflected light [27]. Considering an electromagnetic wave with a H and E polarization, the reflection and transmission can be differentiated using the wave impedance Z, which can be written according to [28] as

$$Z_l^E = \frac{\omega \mu_l}{k_{n,l}} \tag{2.50}$$

for the E polarization and

$$Z_l^H = \frac{k_{n,l}}{\omega \varepsilon_l} \tag{2.51}$$

for the H polarization, with μ_l describing the permeability and ε_l the permittivity. The index l describes the l-th layer of a sample with an arbitrary amount of layers. The relations for the norm of the normal component of the complex wave vector in z direction can be written as

$$k_{n,l} = \sqrt{\varepsilon_l \, \mu_l \, \omega^2 - k_0^2 \, \sin^2(\alpha)}, \tag{2.52}$$

with α denoting the angle of incidence. Utilizing the relation above and $\omega = k_0 c_0$, the wave impedance for the H and E polarization can also be expressed as

$$Z_l^E = \frac{\omega \mu_l}{k_0 \sqrt{\varepsilon_l \mu_l c_0^2 - \sin^2(\alpha)}} \tag{2.53}$$

and

$$Z_l^H = \frac{k_0 \sqrt{\varepsilon_l \mu_l c_0^2 - \sin^2(\alpha)}}{\omega \varepsilon_l}. \tag{2.54}$$

The expressions can be simplified further with introducing the relative permittivity $\varepsilon_{r,l} = \varepsilon_l / \varepsilon_0$ and relative permeability $\mu_{r,l} = \mu_l / \mu_0$ as well as the free space wave impedance $Z_0 = \sqrt{\mu_0 / \varepsilon_0}$ to

$$Z_l^E = Z_0 \frac{\mu_r}{\sqrt{\varepsilon_r \mu_r - \sin^2(\alpha)}} \tag{2.55}$$

and

$$Z_l^H = Z_0 \frac{\sqrt{\varepsilon_r \mu_r - \sin^2(\alpha)}}{\varepsilon_r}, \tag{2.56}$$

where also the relation $c_0 = 1/\sqrt{\varepsilon_0 \mu_0}$ is used. The change of the wave impedance for different angles of incidence and permittivities for a H and E polarization can be seen in Fig. 2.7. The wave impedance is drawn as the ratio of two media. For the first medium, $\varepsilon_r = 1.0$ is used, which represents air. Therefore, the angle which result in a ratio $Z_{m2}/Z_{m1} = 1$ represent a wave impedance of the second medium equal to the free space wave impedance. This angle is equivalent to the Brewster angle, mentioned before. It can be seen that for small angles, the polarization does not influence the wave impedance. However, for larger angles the difference between H and E polarization increases. Since radomes or painted bumpers are usually tilted at rather small angles, an influence cause by polarization can therefore be neglected and it is not expected to have an impact on the sensor performance.

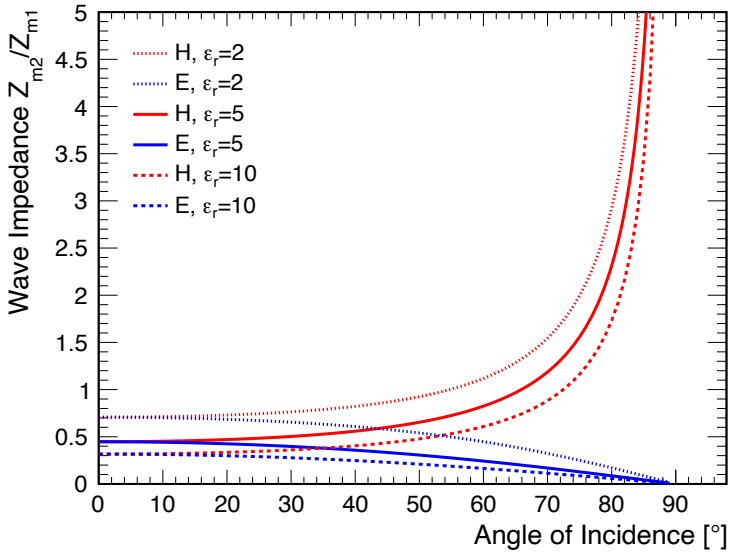

Figure 2.7: Change of wave impedance for different permittivities and angles of incidence. The wave impedance is drawn as the ratio of two media Z_{m2}/Z_{m1}. The permittivity refers to the second medium for the first medium $\varepsilon_r = 1.0$ is used, which represents air.

CHAPTER 3

Permittivity Determination of Materials and Coatings

In order to compare materials and coatings regarding radar transparency a descriptive quantity is necessary. In this thesis the relative permittivity is used to evaluate the radar transparency of coatings, since it does not depend on the thickness. This is especially interesting since applying the coating to a sample is subject to tolerances. In this chapter a method to determine the permittivity of multilayer samples is presented. This includes a proper sample preparation as well as a proper thickness determination of the coatings. The method developed within the framework of this thesis can also be found in [29]. In this chapter also the dielectric behavior of a Polypropylene (PP) and a Polycarbonate (PC) substrate is investigated. Furthermore, the possibilities of designing a resonant radome for the radar is evaluated.

3.1 Structure of Painted Bumpers

A modern painted bumper consists of three layers, the substrate, basecoat and clearcoat as shown in Fig. 3.1. Although primer were an inherent part of the bumper design, state of the art bumpers are produced without primer. However, since spare part bumpers are still coated with primers, they are not obsolete. Due to an elaborate preparation of the bumper substrate, the basecoat can be applied directly on the substrate in series production. This preparation includes a treatment with heat and ionized air, which guarantees an extremely clean surface. Since these methods are hard to adopt for repair shops, spare parts include primers. In the following the different parts of a painted bumper are elaborated.

Substrate: The substrate of the bumper is usually made of Polypropylene (PP), at an overall thickness of 3 mm. The area before the SRR sensor is slightly thicker in order to achieve a more radar transparent bumper (see Section 3.7). For radomes often Polycarbonate (PC) or Acrylonitrile Butadiene Styrene (ABS) is used as a

substrate material. Even though they are relatively comparable in terms of radar transparency, there can be differences in the homogeneity, which is discussed in Section 3.6.

Primer: Usually the primers are applied 10 µm thick. As mentioned before, primer are usually only applied to spare part bumpers and are sandwiched between the substrate and the basecoat. In general primers are used to even out the roughness of the substrate as well as increasing the adhesive effect between substrate and basecoat. Primers can be non conductive or conductive. The latter ones show a very high real part of the relative permittivity as well as a dielectric high loss. This is mainly caused by the high amount of graphite necessary for the conductivity, which enables an electrostatic application of the coatings.

Basecoat: The basecoat measures around 20 µm in thickness and defines the color and the effect of the paint. The basecoat is also the most problematic part regarding radar transparency. The permittivity ranges from low values comparable to the plastic substrate to very high values mainly caused by the effect pigments. These include aluminum flakes, mica and xirallic particles, which can be found in metallic paints. Mica particles are hydroaluminum silicate minerals [30] [31], where xirallic is a trademarked effect pigment for aluminium oxide flakes coated with refractive metal oxides [32]. Furthermore, TiO_2 is also a very important part of basecoats. It is used to modify the appearance of pigments such as aluminum flakes as well as the coating itself. This is caused by the fact that TiO_2 has a high refractive index and therefore makes the color appear bright and vibrant

Clearcoat: This layer is 30 µm thick and serves as a protective layer for the basecoat. The main formulation consists of acrylic resin [33]. There is also the possibility to add silica such as silicon dioxid (SiO_2) to change the appearance of the clearcoat. SiO_2 is often used as a matting agent. Within the framework of this thesis different concentrations of SiO_2 are investigated, ranging from 20 % to 60 %. However, for radar transparency no influence could be examined. In general, clearcoats are comparable to the substrate from a radar perspective.

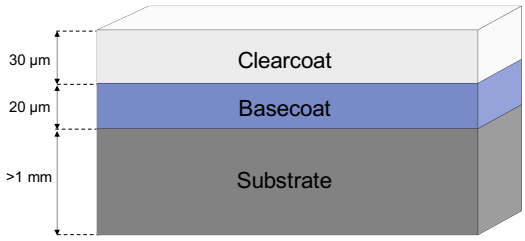

Figure 3.1: Schematic of the structure of a modern painted bumper including the thickness of each layer.

3.2 Method and Modelling

Characterizing materials using the permittivity as a descriptive quantity have been of great interest in the past. Since it is not possible to determine the dielectric properties of the basecoat and clearcoat without a substrate, at least a two layer sample structure is necessary. For the coatings studied within this thesis the clearcoat is also necessary. This is due to the fact that water based basecoats in contrast to solvent based show a slightly sticky and viscous behavior even after a long dry time. This results in a sample structure, which consists of three layers. More information about the difference between water and solvent bases basecoats can be found in Section 3.8. Existing methods for single layered samples are found in [34] [35] [36], [37] [38] [39]. Also in the W-band material characterization are developed including waveguide measurement [40], quasi-optical measurement [41] as well as novel approaches [42] [43]. Methods taylored to multilayer samples are reported in [44] [45]. Unfortunately, these methods are not suited for investigating automotive coatings, since they either require a sample size as small as the waveguide or a special sample preparation, not possible for automotive coatings. Therefore, within this thesis an easily adoptable method is developed utilizing two different commercial measurement setups. The first setup consists of a Vector Network Analyzer (VNA) combined with a corrugated horn antenna. This setup measures the four complex scattering parameters S_{11}, S_{22}, S_{12} and S_{21} of the sample. The second measurement setup is a commercially available quasi optical free space measurement device dedicated towards the automotive sector. With this device only the amplitude of the transmission is recorded. Within the framework of this thesis the second device serves as a validation. More information about the measurement devices and procedure can be found in Section 3.3. As mentioned before, for water based coatings a three layered structure is necessary, therefore the samples follow the same structure as a painted car bumper. For a substrate a 6.4 mm thick PC plate is used. The thickness allows to have multiple resonances within the measured frequency bandwidth. Therefore, the curve fitting algorithm used to determine the permittivity runs in less numerical ambiguities as it can be seen in Section 3.5.1. Moreover, these plates have a high dielectric homogeneity when compared to PP plates, as shown in Section 3.6. The used substrate is also manufactured with permittivity determination in mind and therefore is shaped like a bar. This form leads to one side having rounded edges, which reduce the surface tension of the coating [46]. Hard edges would result in a slight concave shape of the coating resulting in a distortion of the measured reflectivity, which in return deteriorates the measurement precision.

3.2.1 Thickness Measurement

Determining the thickness of each layer of the sample is crucial for achieving high precision, since it serves as a direct input for the determination of the permittivity. Since only one layer can be unknown at a time, the real part of the permittivity and the loss factor have to determined one at a time. An error in thickness will result in an error in the determined permittivity for the layer needed to evaluate the permittivity of the next layer. For measuring the thickness of the coatings an eddy current method is used.

Therefore, metal stripes are applied to the substrate, separated into three parts. One part is used for reference measurements with a thickness measurement device, whereas the other two areas are used to measure the thickness of only the clearcoat and the clearcoat with basecoat combined. The thickness of the basecoat is then determined by subtracting the thickness of the clearcoat, which has to be measured beforehand. The measurement device itself consists of a coil which is wound around a ferrite core. Due to a current flowing through the ferrite core, an alternating magnetic field is induced, which in return induces an eddy current in the metal stripe where the coatings are applied to. This leads to an alternating magnetic field induced in the opposite direction, which weakenes the field, which was originally created by the coil. How much the field is weakens corresponds to the distance between the coil and the metal stripe, which finally corresponds to the thickness of the coating itself. A graphical interpretation of a thickness measurement using eddy current can be seen in Fig. 3.2.

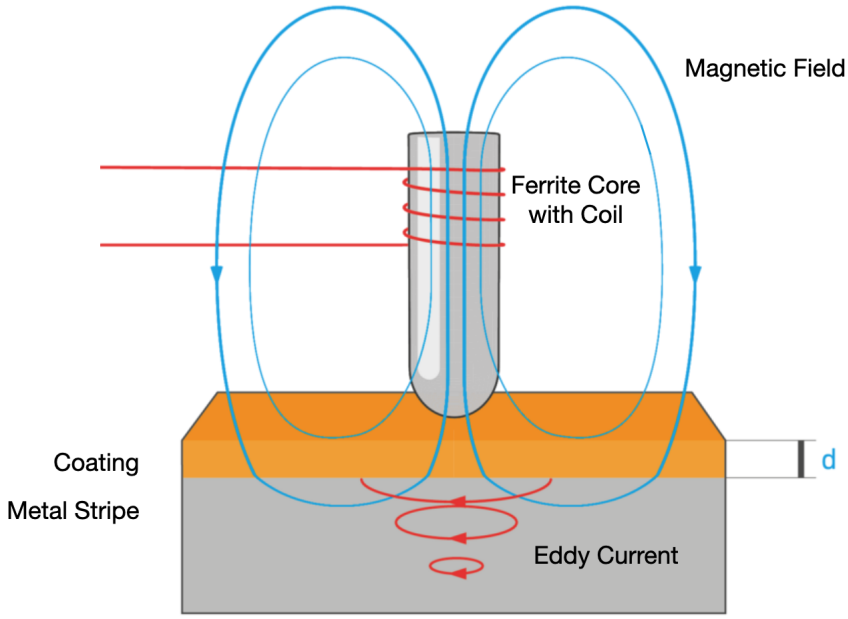

Figure 3.2: Schematic for an amplitude sensitive eddy current measurement method (Taken and altered from [47]).

The thickness of the coating is measured in 16 points along the metal stripe and averaged afterwards. Measuring the thickness of the coating of the same sample only showed a deviation by 0.2 µm and therefore the resulting measurement uncertainty is neglectable. In order to determine the thickness of the substrate itself a micrometer is used. The largest deviation in thickness originates from the substrate. As a result, it is not sufficient enough to measure the thickness of any PC substrate plate. Since the mechanical micrometer might damage the surface of the substrate, which can have a negative im-

pact on the adhesion of the coating, the thickness of the substrate has to be evaluated after the application of the coating. Therefore, the micrometer is used to measure the thickness of the entire sample including all layers. The thickness of the substrate is then determined by subtracting the thickness of the basecoat and clearcoat, which are measured beforehand. The error originating from the substrate measurement is determined to be 3 µm, which is the combined uncertainty originating from the micrometer itself and the uncertainty resulting from repeatability. The latter one is determined by measuring the same point multiple times and considering the highest deviation. A picture of a sample including the metal stripe can be seen in Fig. 3.3.

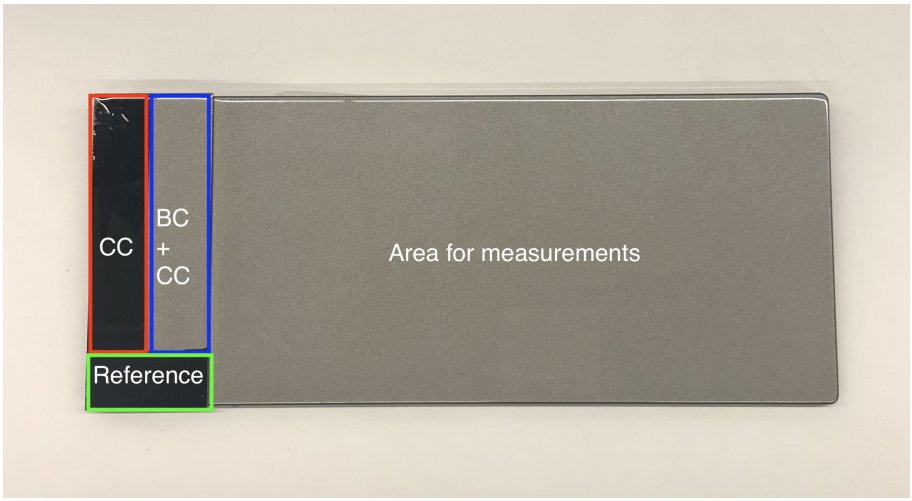

Figure 3.3: Painted sample for determination of the permittivity of the sample. On the left side the metal stripe can be seen, where the thickness of the basecoat (BC) (red) and clearcoat (CC) + basecoat (blue) is measured using the eddy current method. The reference area (green) is used for reference thickness measurements.

3.3 Measurement Setup

Two different measurement setups are used in order to determine the dielectric properties of the samples. The first one consists of a VNA and a corrugated horn antenna, the second one is a commercially available quasi-optical free space device. The second setup offers complementary measurements and is used to crosscheck the results. The following sections describe the technical details of each device.

3.3.1 S-Parameter Corrugated Horn Antenna Measurement

The first one consists of a R&S ZVA 24 VNA combined with a SwissTo12 Material Characterization Kit (MCK). The VNA is connected to two ZVA-Z90 upconverter, which enables measuring in a frequency range from 60 - 90 GHz. With this setup the four complex scattering parameter S_{11}, S_{12}, S_{21}, S_{22} are measured. An overview of the setup

can be seen in Fig. 3.4. The conducted measurement utilizes 30 GHz bandwidth. As a result the determined permittivity is considered to be dispersionless, which is valid for polymers at such frequencies [48]. Using such a large bandwidth brings benefits when applying the fitting algorithm to determine the dielectric properties, as shown in Section 3.5.1.

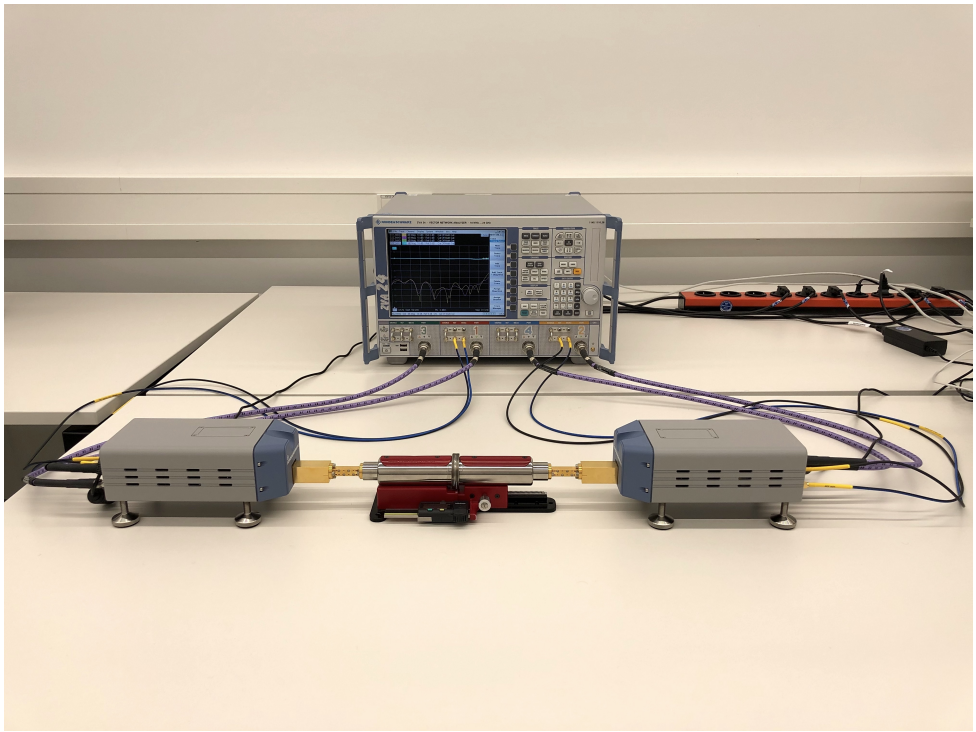

Figure 3.4: VNA measurement setup. The setup consists of a R&S ZVA 24 VNA connected to two ZVA-Z90 upconverter combined with a SwissTo12 Material Characterization Kit (red).

The VNA is calibrated with a Short Open Load Thru (SOLT) calibration. Since the MCK is added to the setup afterwards, for each measurement the reflection (S_{11}, S_{22}) and transmission (S_{12}, S_{21}) is normalized using the included software, which guarantees a fixture de-embedding. The reflection normalization is done using a metal plate, where the transmission is normalized by closing the gap between the two antennas. This setup allows to measure the scattering parameter locally within an area of 40 mm. As a result, multiple measurement points can be realized using the samples developed in this thesis. In contrast to the used setup, a quasi-optical setup has the disadvantage that the measured area depends on the width of the gaussian beam. Furthermore, the measurement represents an average over the area. As a result possible inhomogeneities within the sample can not be identified. The used configuration of the VNA with the MCK is shown in Table 3.1. The number of measurement points is set to 1600, a higher

number does not show a positive effect on the permittivity determination. The timegate of the MCK is adjusted to the thickness of the used sample.

Parameter (VNA)	Value
Bandwidth	60-90 GHz
Power Upconverters	7 dBm
IFBW	500 Hz
Number of Points	1600
Timegate MCK	580 ps

Table 3.1: Configuration VNA with MCK

3.3.2 Free Space Transmission Loss Measurement

For the second measurement device the perisens Radome Measurement System (RMS) is used, which enables a quasi-optical free space measurement. This technique is especially interesting for curved samples because they are problematic for the VNA, due to the MCK sample holder. The measurement is comparable to a S_{21} only measurement. As is the case with the VNA, the whole available bandwidth reaching from 76 - 81 GHz is used. This bandwidth is chosen by the manufacturer to be future proof for the potentially available frequency band for radar sensors from 77 - 81 GHz. For the measurement 51 measurement points are used within the available bandwidth. The sample is placed between the RX and TX antenna, where the orientation does not matter, since only the transmission is measured. The measurement device can be seen in Fig. 3.5. In contrast to the VNA, there is no need for an elaborate calibration from the user side. Before each measurement the transmission has to be normalized to the distance between the antennas, which is done with the included software. This is necessary since the distance might change due to temperature changes. It should be noted that this device is also capable of estimating the real part of the relative permittivity and loss factor of multilayer materials, however, due to comparability reasons, the same method for the sample characterization is used as for the VNA. The recorded data for each measurement can be extracted from the measurement device as the one-way-magnitude of the transmission in units of dB. Although the RMS uses less information when compared to the VNA the results are very comparable as shown in Section 3.5.1.

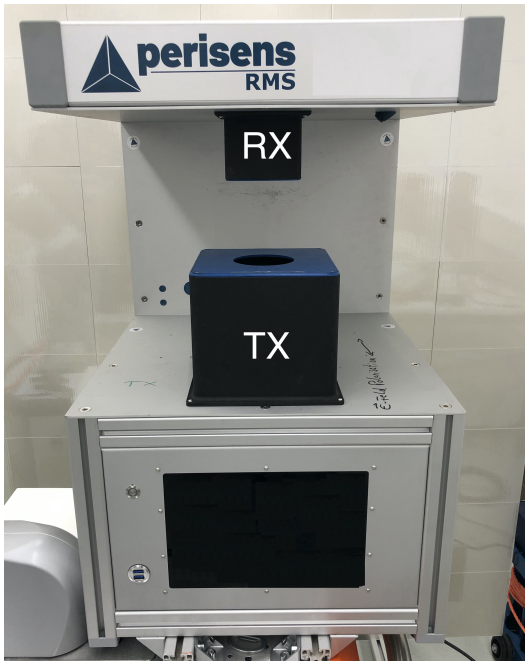

Figure 3.5: RMS measurement setup. The sample is placed on the hole on top of the TX antenna. In order to avoid measurement artefacts, the complete hole has to be covered by the sample.

3.4 Measurement Procedure

For a precise determination of the permittivity, a precise knowledge of the thickness of the coating as well as the substrate is crucial. However, although measuring the thickness of the coatings with an eddy current method, the estimated substrate thickness can result in higher uncertainties due to local inhomogeneities. As mentioned before, the substrate thickness is determined by measuring the painted samples with a micrometer and subtracting the thickness of the basecoat and the clearcoat. In order to compensate for possible local inhomogeneities it is crucial to coincide the area where the electromagnetic wave of the measurement device penetrates the sample with the area where the thickness measurement is taken. This is done using alignment tools to match these areas.
For the VNA setup the measurement is performed as shown in Fig. 3.6 as follows: First the thickness measurement is taken using the micrometer. In total six thickness measurements are taken, three on each side. The thickness measurement is taken using the first alignment tool marked with (1). The holes in the alignment tool correspond to the diameter of the micrometer $d_{\text{micrometer}}$. Subsequently, the second alignment tool is used labeled with (2), where the arches measuring $d_{\text{sample\_holder}}$ represent the diameter of the MCK. The alignment tools are designed in such a way that the center of the arch corre-

sponds to the hole of the first alignment tool and therefore the thickness measurement is taken where the VNA measurement is conducted.

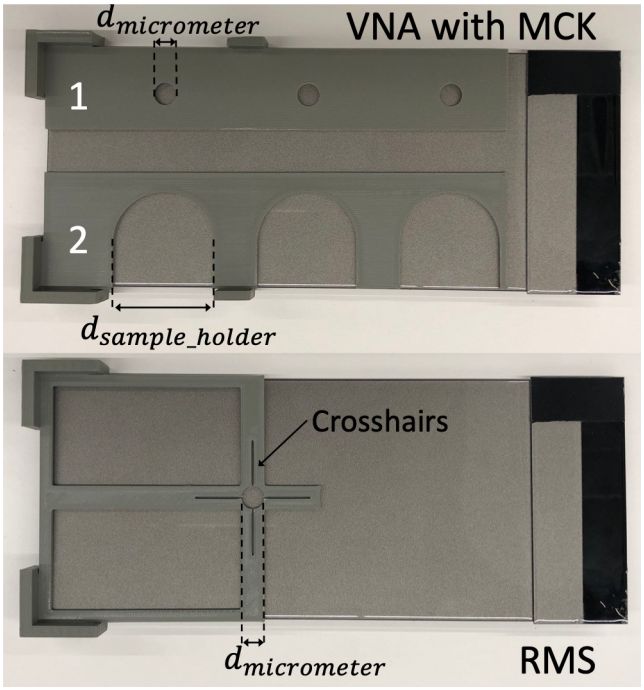

(a)

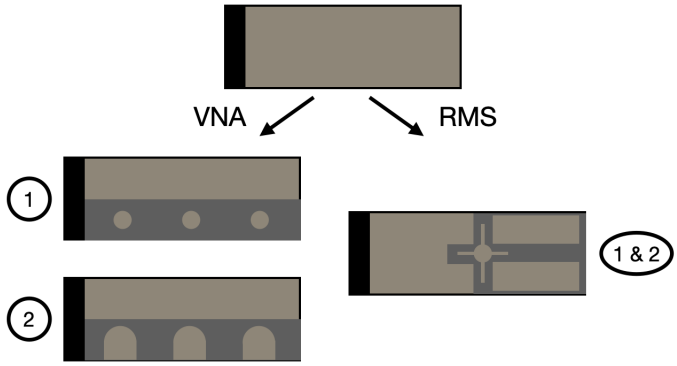

(b)

Figure 3.6: a) Alignment tools on a sample for the VNA and RMS b) Steps for measurement procedure with alignment tools.

For the RMS only one template exists, since the sample can be positioned using the crosshair projected by the laser of the device. In addition, only one measurement point is taken. This is due to the fact that the measured area roughly corresponds to the size

of the hole above the TX antenna which only makes measuring one point possible due to an insufficient sample size. The alignment tool for the RMS consists of a hole for the thickness measurement and a crosshair for alignment. It should be noted that the alignment tool has to be removed before conducting the measurement. A picture of the samples placed in the VNA and RMS respectively can be found in Fig. 3.7.

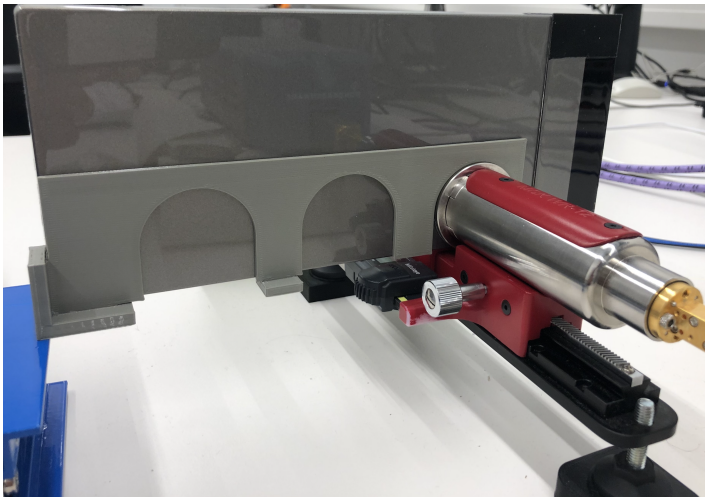

(a)

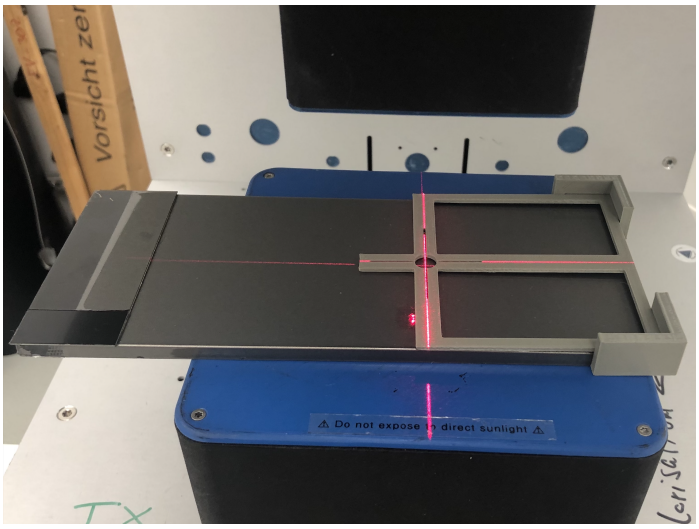

(b)

Figure 3.7: a) Placed sample in the VNA with MCK setup. The alignment tool (2) is used to coincide the area of the thickness measurement with the area measured by the VNA b) Sample with alignment tool for the RMS. The hole is used for the thickness measurement, where the crosshair is used to align the sample.

3.5 Transmission Line Model for Multilayer Samples

There are several methods to model multilayered samples. In the following the transmission line model is used to model a multilayer structure. This approach is already well established in the context of material characterization [49] [50]. The theory of modeling a multilayer sample is based on [51]. The transmission line model can be used to model a N layered sample using a transmission line for each individual layer. Each layer l is described by its thickness d_l, the relative permittivity $\varepsilon_{\mathrm{r},l}$ and the relative permeability $\mu_{\mathrm{r},l}$. The first and N-th layer are surrounded by air with the relative permittivity $\varepsilon_{\mathrm{r},0}$ and the relative permeability $\mu_{\mathrm{r},0}$. Furthermore, each layer is described by a phase factor and a wave impedance. A schematic of a reflected and transmitted wave in a N-th layer structure can be seen in Fig. 3.8.

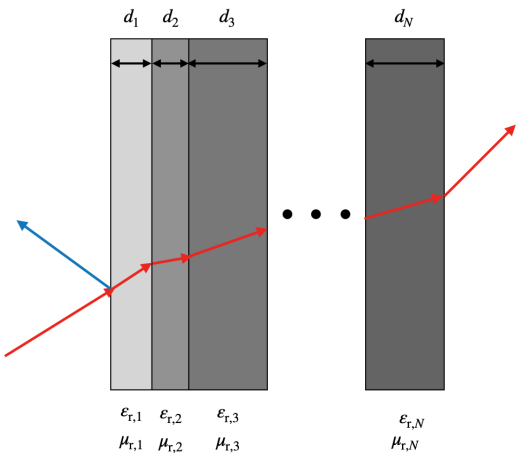

Figure 3.8: Schematic of reflected (blue) and transmitted (red) wave in a N-th layer structure.

Each layer can be expressed as a single matrix. The multilayered sample can then be expressed by multiplying each matrix of each layer. The direction of the measurement depends on the order of multiplication. For N layers the matrix can be written as

$$\mathbf{M}_{\mathrm{sample}} = \begin{bmatrix} m_{11} & m_{12} \\ m_{21} & m_{22} \end{bmatrix} = \prod_{l=1}^{N} \begin{bmatrix} \cos\phi_l & jZ_l\sin\phi_l \\ j\frac{1}{Z_l}\sin\phi_l & \cos\phi_l \end{bmatrix}, \tag{3.1}$$

where $N \in \mathbb{N}$, l denotes the individual layer and j the imaginary unit. In general an arbitrary number of layers can be modeled using this matrix. Often this matrix is also referred to $ABCD$ matrix in literature. Assuming a vertical polarization, the wave impedance can be written as

$$Z_l = Z_0 \cdot \frac{\mu_{\mathrm{r},l}}{\sqrt{\varepsilon_{\mathrm{r},l}\mu_{\mathrm{r},l} - \sin^2(\alpha)}}. \tag{3.2}$$

The factor $Z_0 = \sqrt{\mu_0/\varepsilon_0}$ denotes the free space wave impedance of the vacuum and α the incidence angle of the wave. The phase factor ϕ of each layer can be written as

$$\phi_l = k_l \cdot d_l, \tag{3.3}$$

with k_l denoting the z-component of the complex wave vector, which can be represented using the wavelength λ by [52]

$$k_l = \frac{2\pi}{\lambda}\sqrt{\varepsilon_{\mathrm{r},l}\mu_{\mathrm{r},l} - \sin^2(\alpha)}. \tag{3.4}$$

For the measurements conducted to determine the permittivity some simplification can be made. First the wave of the measurement is always orientated perpendicular to the surface and thus $\alpha = 0$. Moreover, the substrate as well as the basecoat and the clearcoat can be assumed to be non magnetic, which means $\mu_{\mathrm{r},l} = 1$. This assumption is very important, since otherwise only the ratio between the permittivity and permeability could be determined. Also the relative permittivity can be written using the real and imaginary part as

$$\varepsilon_{\mathrm{r}} = \varepsilon'_{\mathrm{r}} - j\varepsilon''_{\mathrm{r}} = \varepsilon'_{\mathrm{r}}(1 - j\,\tan\delta), \tag{3.5}$$

where the term $\tan\delta_l$ is referred to as the loss factor or loss tangent. Taking the assumptions and the relation above into account, the wave impedance (3.2) can be simplified to

$$Z_l = Z_0 \cdot \sqrt{\frac{1}{\varepsilon'_{r,l}(1 - j\,\tan\delta_l)}}. \tag{3.6}$$

The wave vector (3.4) can also be rewritten as

$$k_l = \frac{2\pi}{\lambda}\sqrt{\varepsilon'_{r,l}(1 - j\,\tan\delta_l)}. \tag{3.7}$$

The samples investigated in thesis are not symmetric, meaning that the directional dependence of the reflectivity has to be taken into account. Since the order (substrate $\rightarrow$ basecoat $\rightarrow$ clearcoat) $\neq$ (clearcoat $\rightarrow$ basecoat $\rightarrow$ substrate) and thus $S_{11} \neq S_{22}$, two cases have be modeled. This results in two matrices, which have to be considered for a four scattering parameter measurement. The matrices are a result of multiplying the matrices from (3.1) in the right order. A graphical interpretation can be seen in Fig. 3.9.

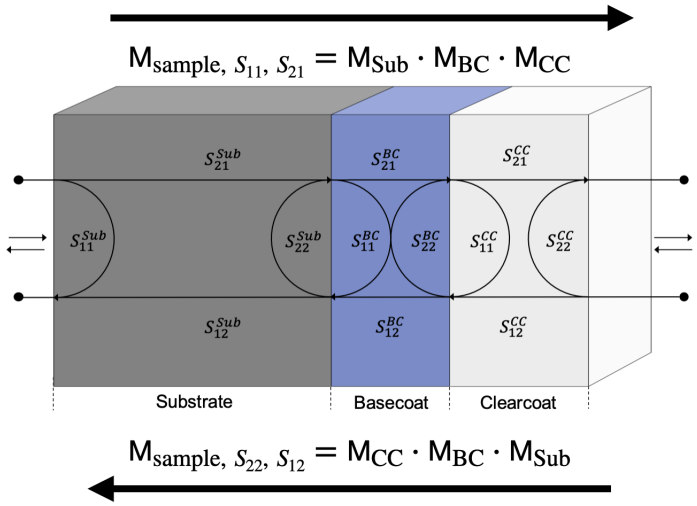

Figure 3.9: Graphical interpretation of a three layer sample similar to a painted car bumper with corresponding scattering parameter and matrix.

Considering a VNA with two ports, the first direction from port 1 to port 2, which represents S_{11}, S_{21} can be defined as

$$\mathbf{M}_{\text{sample, } S_{11},\ S_{21}} = \mathbf{M}_{\text{Sub}} \cdot \mathbf{M}_{\text{BC}} \cdot \mathbf{M}_{\text{CC}}. \tag{3.8}$$

The second matrix multiplication describes the opposite direction from port 2 to port 1, S_{22}, S_{12} respectively and can be written as

$$\mathbf{M}_{\text{sample, } S_{22},\ S_{12}} = \mathbf{M}_{\text{CC}} \cdot \mathbf{M}_{\text{BC}} \cdot \mathbf{M}_{\text{Sub}}. \tag{3.9}$$

After multiplying the matrices in the right order, the reflection coefficient ρ and the transmission coefficient τ for the whole multilayer sample can be extracted from the Matrix $\mathbf{M}_{\text{sample}}$ from the elements m_{11}, m_{12}, m_{21}, m_{22}:

$$\rho = \frac{m_{11} + m_{12}\frac{1}{Z_0} - m_{21}Z_0 - m_{22}}{m_{11} + m_{12}\frac{1}{Z_0} + m_{21}Z_0 + m_{22}}, \tag{3.10}$$

$$\tau = \frac{2}{m_{11} + m_{12}\frac{1}{Z_0} + m_{21}Z_0 + m_{22}}. \tag{3.11}$$

In total there are two reflection factors and two transmission factors when using four scattering parameters.
The real part and the loss factor are determined by using a curve fitting algorithm. It should be noted that only one layer can be unknown due to ambiguities. Therefore, in order to determine the dielectric properties of the basecoat, the properties of the clearcoat and the substrate have to be determined beforehand. As a result, additional

samples are necessary, the bare substrate and a sample with the substrate and only clearcoat on top. With one layer unknown the real part of the relative permittivity and the loss factor can be determined by minimizing the difference between the measured data (mes) and the model (mod) as a sum over the measured frequencies. For the VNA measurements this function can be expressed as

$$\begin{aligned}\xi_{\mathrm{VNA}}(f) = \sum_f \Bigg(& \sqrt{(\rho_f^{mes,S11} - \rho_f^{mod,S11})^2} \\ & + \sqrt{(\rho_f^{mes,S22} - \rho_f^{mod,S22})^2} \\ & + \sqrt{(\tau_f^{mes,S21} - \tau_f^{mod,S21})^2} \\ & + \sqrt{(\tau_f^{mes,S12} - \tau_f^{mod,S12})^2} \Bigg).\end{aligned} \tag{3.12}$$

This function includes two transmission and two reflection coefficients which are a result of (3.8)-(3.9). For the RMS measurements only one transmission coefficient τ is considered, since only one transmission measurement is conducted. The function used for determining the dielectric properties can be written as

$$\xi_{\mathrm{RMS}}(f) = \sum_f \left(\sqrt{(\tau_f^{mes,S21} - \tau_f^{mod,S21})^2} \right). \tag{3.13}$$

As an algorithm, MIGRAD is used, which is part of the Minuit C++ package [53] [54]. This algorithm utilizes a variation of the well stablished Newton's method, which is called variable metric method [55]. The mathematical principle is described in detail in [56]. Considering that the minimum of a functions corresponds to the zero of the functions derivative, the method can be expressed in a multidimensional case as

$$\underline{\mathbf{x}}_{n+1} - \underline{\mathbf{x}}_n = -H^{-1}(\underline{\mathbf{x}}_n)\underline{\nabla} f(\underline{\mathbf{x}}_n), \tag{3.14}$$

where $H^{-1}(\underline{\mathbf{x}}_n)$ denotes the inverse of the Hessian matrix. For small $\underline{\mathbf{x}}$ the following can then be stated

$$f(\underline{\mathbf{x}}) - f(\underline{\mathbf{0}}) \approx \underline{\mathbf{x}}^T \left(\frac{1}{2} H(\underline{\mathbf{x}}) \right) \underline{\mathbf{x}}. \tag{3.15}$$

This expression describes the estimated vertical distance to the minimum [55]. Using this numerical method achieved precise values for determining the real part of the relative permittivity and the loss factor as shown in the following section.

3.5.1 Results and Validation of Method

The following shows results of a green and silver basecoat. Besides the color, the basecoats mainly differentiate in their real part of the permittivity. The silver basecoating has a high permittivity, where the green basecoat has a relatively low permittivity. The real part of the permittivity and the loss factor is determined using the method and the model described above. As mentioned before, only one layer can be unknown at once and since all examined samples have to consist of a substrate basecoat and clearcoat, the dielectric properties of the substrate and the clearcoat have to be determined beforehand. Since all samples investigated within this thesis share the same substrate and clearcoat, this only has to be done once. In general the number of layers should be kept as low as possible to increase the precision. For water based coatings, three layers are the minimum amount of layers. The uncertainties considered in this thesis for ε'_r and $\tan\delta$ arise from the uncertainty of the thickness measurement. As mentioned in Section 3.2.1, the error from the measurement is neglectable and only the measurement error originating from the thickness measurement of the substrate is considered. Therefore, the thickness uncertainty of 3 µm serves as a direct input for the curve fitting. This in return gives an interval for possible values for ε'_r and $\tan\delta$, where the width of the interval is used as an uncertainty. The values of the samples investigated for demonstrating the method can be seen in Table 3.2 for the VNA and in Table 3.3 for the RMS. The samples include a Polycarbonate (PC) substrate, Clearcoat (CC) and two different Basecoats (BC).

Sample	ε'_r (VNA)	$\tan\delta$ (VNA)
Substrate (PC)	$2.736 \pm 2.8 \cdot 10^{-3}$	$7.0 \cdot 10^{-3} \pm 4.8 \cdot 10^{-6}$
CC	$2.856 \pm 96.6 \cdot 10^{-3}$	$2.80 \cdot 10^{-2} \pm 1.1 \cdot 10^{-3}$
Silver BC	$15.898 \pm 22.9 \cdot 10^{-2}$	$3.4 \cdot 10^{-2} \pm 0.1 \cdot 10^{-2}$
Green BC	$5.351 \pm 23.5 \cdot 10^{-2}$	$4.7 \cdot 10^{-2} \pm 0.3 \cdot 10^{-2}$

Table 3.2: Comparison of ε'_r and $\tan\delta$ obtained with the VNA setup.

Sample	ε'_r (RMS)	$\tan\delta$ (RMS)
Substrate (PC)	$2.761 \pm 2.5 \cdot 10^{-3}$	$5.9 \cdot 10^{-3} \pm 2.4 \cdot 10^{-5}$
CC	$2.833 \pm 15.4 \cdot 10^{-2}$	$1.2 \cdot 10^{-3} \pm 2.0 \cdot 10^{-3}$
Silver BC	$15.884 \pm 16.6 \cdot 10^{-2}$	$1.9 \cdot 10^{-2} \pm 0.56 \cdot 10^{-2}$
Green BC	$5.149 \pm 23.2 \cdot 10^{-2}$	$2.4 \cdot 10^{-2} \pm 0.8 \cdot 10^{-2}$

Table 3.3: Comparison of ε'_r and $\tan\delta$ obtained with the RMS setup.

By comparing the uncertainties of the samples displayed in the tables, it can be seen that the uncertainty is higher for the basecoats than for the bare substrate. This is caused

by the increased complexity of the model, which increases the numerical ambiguity. Therefore, the number of layers should be kept as low as possible. Also, it can be seen that the uncertainty for the loss factor is higher when compared to the uncertainty of the real part of the permittivity. This is mainly caused by numerical difficulties when minimizing two quantities simultaneously with different orders of magnitude. However, this effect is reduced by increasing the importance of the factor in the minimizer. This effect is more present for the RMS than the VNA, which can be explained by the fact that the RMS method uses 75 % less data (transmission only measurement compared to four scattering parameters). As already mentioned, for the VNA six measurement points are considered, where for the RMS only one measurement point can be considered. For the RMS as well as for the VNA, the uncertainties are relatively small and therefore tolerable. The fitting results can be seen in Fig. 3.10, 3.11 and Fig. 3.12, 3.13 for the VNA and RMS respectively. Overall, it can be seen that the model agrees well with the measured data. Also, for the silver coating, taking the directional dependence of the reflection into account becomes clear. This effect is not as present for the green basecoat due to the lower permittivity. In general the directional dependence can reduce numerical ambiguities and therefore the precision of the values can be increased. Furthermore, having multiple resonances within the measured bandwidth also decreases ambiguities, which is the reason for the PC substrate measuring 6.4 mm in thickness. Also a very good agreement can be seen between the results for the two basecoats when comparing the VNA with the RMS. The real part of the relative permittivity only deviates 0.014 for the silver coating and 0.202 for the green coating. The loss factor shows a higher deviation being $1.5 \cdot 10^{-2}$ and $2.3 \cdot 10^{-2}$ for the silver and green basecoat respectively. Overall it can be stated again that the higher deviation in the loss factor is caused by the RMS using less information than the VNA setup.
For validating the method Rogers Duroid substrates are used. This is due to the fact that no literature values for the coatings exist. The usual copper cladding is removed, in order to use the bare laminate. The Duroid substrates are known for their precise and constant dielectric properties. Furthermore, they can be assumed to be dispersionless, which is convenient, since the permittivity in this thesis is determined over a bandwidth rather than a single frequency. In total, two different substrates are used, namely Rogers Duroid 5880 and 3003. The reference values can be found in [57] and [58]. For validating the one layer permittivity (e.g. substrate only measurements), the bare Duroid sheets are measured. For the two layer measurement, which correspond to the determination of the permittivity of the clearcoat, the two substrates are stacked (referred to as Validation 1) and measured as one sample consisting of two layers. The dielectric properties of 3003 are considered unknown. For the three layer validation (referred to as Validation 2), which correspond to the basecoat measurement, Duroid 3003 is sandwiched between two 5880. Similar to the two layer validation, the Duroid 3003 substrate layer is again considered to be unknown. The results of the validation can be found in Table 3.4 and 3.5 for the VNA and RMS setup respectively. Comparing the values of the validation with the values found in literature, it can be seen that the model shows a very good agreement. The RMS show a slightly higher deviation from literature, which can be

explained by the fact that the RMS measurement provides less information to the fitting algorithm, since only the one-way transmission is recorded.

Sample	ε_r' (VNA)	$\tan\delta$ (VNA)	ε_r' (Ref.)	$\tan\delta$ (Ref.)
RO5880	$2.205 \pm 4.4 \cdot 10^{-3}$	$0.9 \cdot 10^{-3} \pm 2.1 \cdot 10^{-5}$	2.2 ± 0.02	$0.9 \cdot 10^{-3}$
RO3003	$3.030 \pm 4.4 \cdot 10^{-3}$	$1.1 \cdot 10^{-3} \pm 3.3 \cdot 10^{-6}$	3.0 ± 0.04	$1.0 \cdot 10^{-3}$
Validation 1	$3.010 \pm 5.6 \cdot 10^{-3}$	$1.0 \cdot 10^{-3} \pm 1.3 \cdot 10^{-5}$	3.0 ± 0.04	$1.0 \cdot 10^{-3}$
Validation 2	$2.980 \pm 5.7 \cdot 10^{-3}$	$1.2 \cdot 10^{-3} \pm 1.9 \cdot 10^{-5}$	3.0 ± 0.04	$1.0 \cdot 10^{-3}$

Table 3.4: ε_r' and $\tan\delta$ values obtained with the VNA setup compared to literature values.

Sample	ε_r' (RMS)	$\tan\delta$ (RMS)	ε_r' (Ref.)	$\tan\delta$ (Ref.)
RO5880	$2.410 \pm 5.4 \cdot 10^{-3}$	$0.8 \cdot 10^{-3} \pm 2.1 \cdot 10^{-5}$	2.2 ± 0.02	$0.9 \cdot 10^{-3}$
RO3003	$3.010 \pm 6.4 \cdot 10^{-3}$	$0.9 \cdot 10^{-3} \pm 4.1 \cdot 10^{-6}$	3.0 ± 0.04	$1.0 \cdot 10^{-3}$
Validation 1	$2.986 \pm 7.1 \cdot 10^{-3}$	$1.1 \cdot 10^{-3} \pm 4.6 \cdot 10^{-6}$	3.0 ± 0.04	$1.0 \cdot 10^{-3}$
Validation 2	$3.090 \pm 7.5 \cdot 10^{-3}$	$1.2 \cdot 10^{-3} \pm 5.1 \cdot 10^{-6}$	3.0 ± 0.04	$1.0 \cdot 10^{-3}$

Table 3.5: ε_r' and $\tan\delta$ values obtained with the RMS setup compared to literature values.

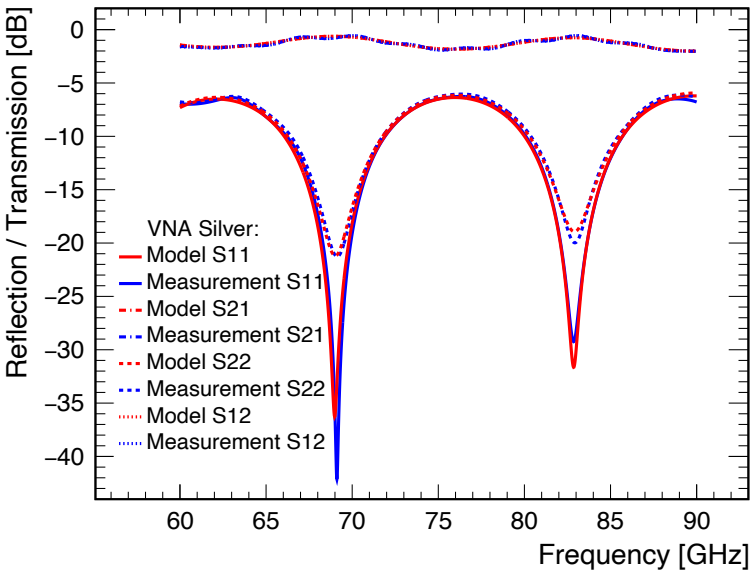

Figure 3.10: Model fitted to VNA measurement data for the silver basecoat to the reflection (in the lower part of the graph) and the transmission (in the upper part of the graph). The directional dependence of the reflectivity can be clearly seen when comparing S_{11} and S_{22}.

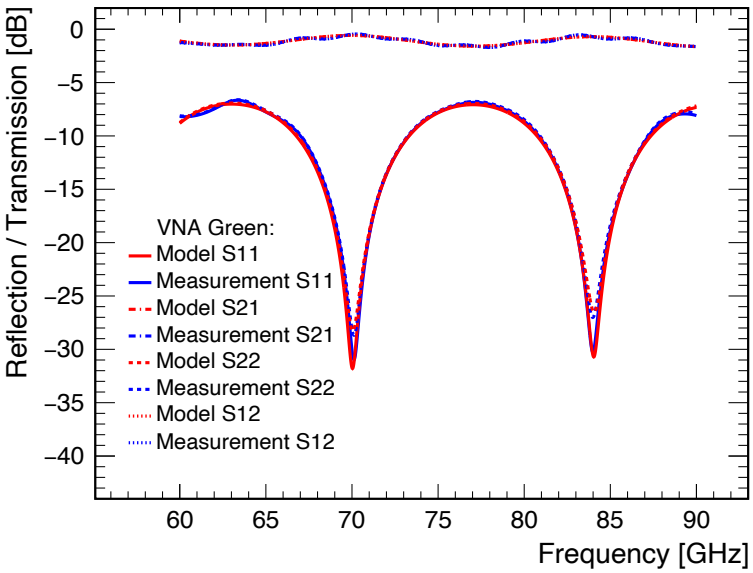

Figure 3.11: Model fitted to VNA measurement data for the green basecoat to the reflection (in the lower part of the graph) and the transmission (in the upper part of the graph). Due to the lower reflectivity of the basecoat, the influence of the directional dependence is less distinct compared to the silver basecoat.

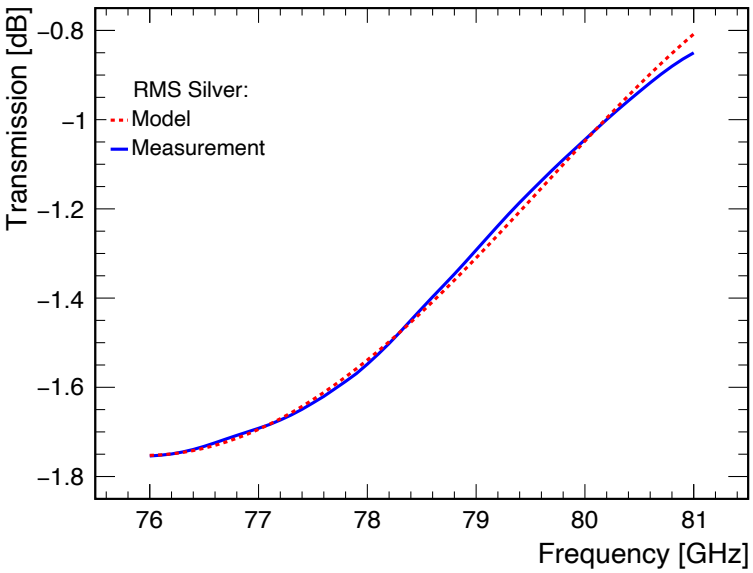

Figure 3.12: Model fitted to RMS measurement data for the silver basecoat.

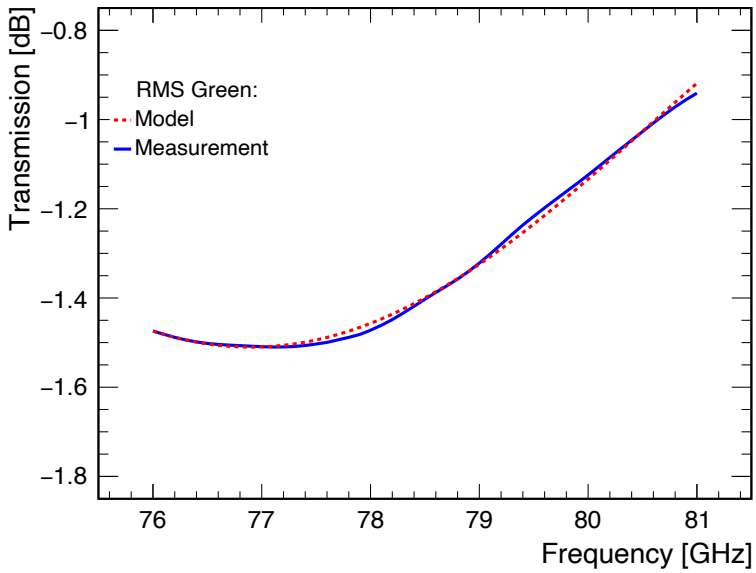

Figure 3.13: Model fitted to RMS measurement data for the green basecoat.

3.5.2 Limits of Method

The used transmission line model is often stated to be used if the wavelength is comparable to the size of the distributed element. Since the thickness of one layer is much smaller than the wavelength, the limits of the method and model used in this thesis is investigated. The goal of this study is to find a problematic layer thickness of the coating, where the transmission line model is not applicable. Since basecoats can not be applied at an arbitrary thickness due to the viscosity of the material, primer are used for this study. The primer is applied from a thickness between 0.9 and 54.4 µm. In total, the samples consist of two layers, the substrate and the primer. Since the permittivity is a material constant, the value for the primer must not change with increasing or decreasing thickness. Although some fluctuation is expected due to measurement error, a significant change should not be seen. In total, 14 samples are investigated, where 6 samples have a thickness measuring below 2 µm. The resulting ε_r' and $\tan\delta$ of this investigation can be seen in Fig. 3.14 and 3.15 respectively. Looking at the results for the real part of the permittivity, it can be seen that large deviations occur for a thickness below 2 µm. The discrepancy between VNA and RMS shows the highest value for low thicknesses. For a thicker application, the real part of the permittivity shows a stable behavior as intended with minor fluctuations which are tolerable. The fluctuations are mainly caused by the fact that the primers are applied by hand, which results in slightly inhomogeneous thickness gradient over the sample. Considering the error, it can be seen that it increases with decreasing thickness. This behavior is expected, since although the uncertainty caused by the thickness measurement of the coatings is considerably small compared to the uncertainty caused by the micrometer, it still has an impact if the thickness of the coating is extremely small. As already seen in previous error anal-

ysis, the RMS tends to show a higher uncertainty than the VNA data. As discussed in Section 3.5.1, the precise determination of $\tan\delta$ is difficult because the numerical value of the ε_r' is two orders of magnitude higher. As a result, the higher fluctuations seen in Fig. 3.15 when compared to the fluctuation of the real part of the permittivity are expected.

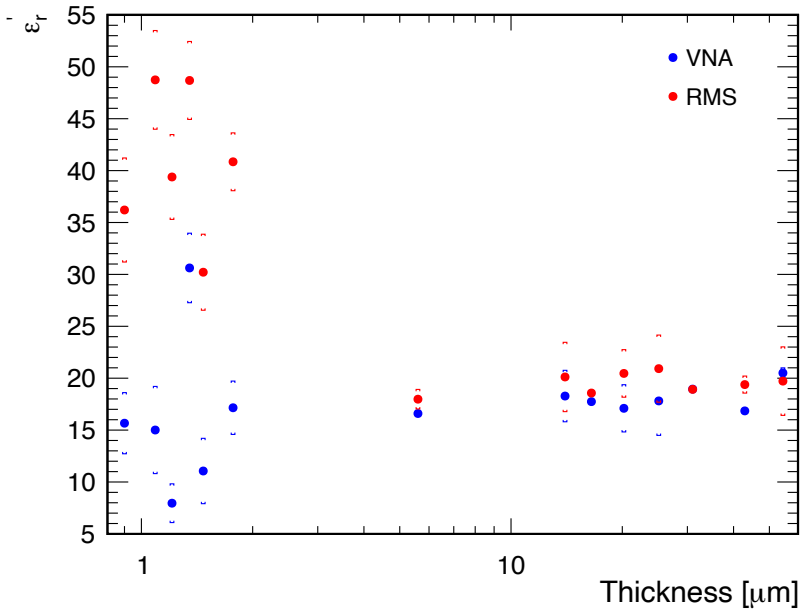

Figure 3.14: Change of real part of the relative permittivity with thickness for a conductive primer. The uncertainty is marked with '[ ]'. For a thickness below 2 µm it can be seen that large fluctuation for ε_r' occur, due to the model failing.

It should be noted that the loss tangent values presented in this section are relatively high compared to the basecoats analyzed in Section 3.5.1, since the primer is conductive. Although a limit for a thickness for the method can not be extracted from the loss tangent results, due to a fluctuation over the whole thickness interval, there are several useful informations. It can be seen that the RMS measurements agree with the VNA measurements for higher thicknesses. For a small thickness below 2 µm the difference between RMS and VNA shows the highest value. This behavior is also observed before when investigating the real part of the permittivity, however, in Fig. 3.14, the VNA data shows smaller values when compared to the RMS data, where in Fig. 3.15, the opposite is the case. This shows that the high fluctuation of the loss tangent or real part of the permittivity are not caused by insufficiently precise thickness measurements, but by a failure of the model. This can be explained by the fact that the permittivity can be expressed by a real and imaginary part as seen in (3.5). Since the real part and the loss tangent are coupled to each other, this may cause numerical problems. With a low coating thickness, an ambiguity arises where a small real part and a large imaginary part

satisfy the same condition as a large real part and a small imaginary part. Therefore, the model used in this thesis is not usable for extremely small thicknesses. In order to avoid possible wrong results caused by this phenomena, all coatings investigated in this thesis are applied with a target thickness of 20 µm for basecoats and 30 µm for clearcoats.

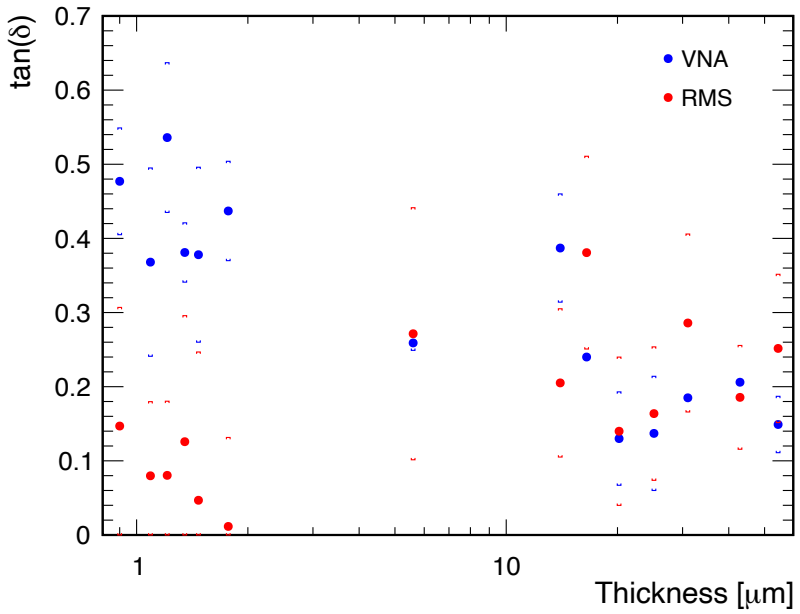

Figure 3.15: Change of the loss tangent with thickness for a conductive primer.

3.6 Determination of Dielectric Properties of Substrates

For modern automotive bumpers PP is a commonly used substrate material. This material has several characteristics, which are very beneficial towards functions a car bumper has to provide. The weight of materials used in the automotive sector is crucial, since light weight materials improve fuel or energy consumption by the car, which in return increases the range of the vehicle. Especially for large exterior parts such as bumpers, light materials are even more of interest. Since PP is the lightest thermoplastic [59], it is an ideal material for automotive bumpers. Thermoplastics are characterized by a higher impact strength, which is especially important for an automotive bumper. By withstanding higher impact strengths, a high amount of energy can be absorbed at very low speeds without cracking the material. Furthermore, thermoplastics are relative easy to process, comparatively cheap and can adapt to complex mold designs [60]. Radomes on the other hand are manufactured from different materials. For single layered radomes, one commonly used material is ABS, which is often chosen since it provides tensile strength, a high ductility and shows a hydrophobic behavior [61]. Besides ABS, PC is also used for radomes, especially state of the art multilayered radomes including a

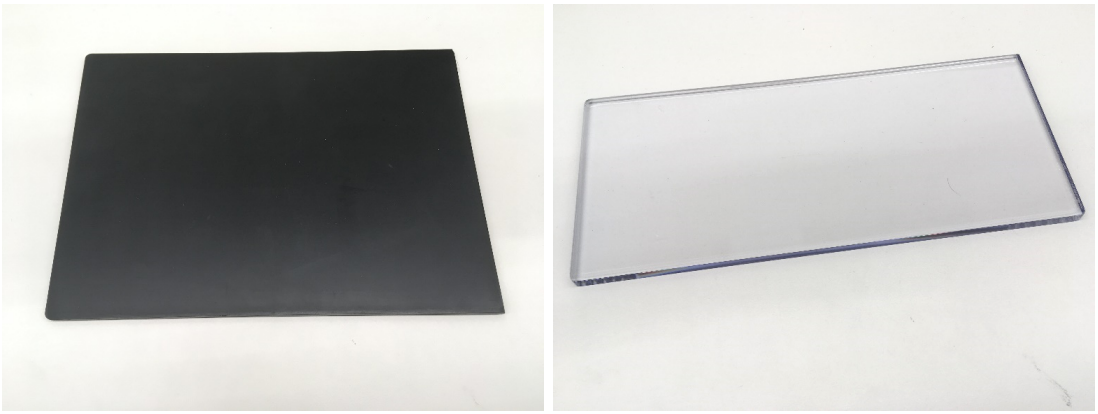

(a) (b)

Figure 3.16: a) PP Substrate measuring $210 \times 148 \times 2.9\,\text{mm}$. b) PC substrate measuring $250 \times 105 \times 6.4\,\text{mm}$.

PVD layer use PC, since it is a transparent material. Besides mechanical and chemical properties of materials, also the dielectric properties are of interest, when the material is placed to cover a radar sensor. Therefore, in this section PP and PC are compared using the permittivity. The main focus is to investigate the dielectric homogeneity to evaluate a possible differences of the substrate used for a painted bumper and a modern radome. All the data presented in this section is recorded using the VNA with MCK setup, which makes local measurements possible due to the small measurement area. These measurement are not possible using the RMS setup, since it can only realize one measurement point for each sample. In total six measurement points are taken using the alignment tool method described in Section 3.4. For each substrate type 20 plates are investigated, in order to determine not only the dielectric homogeneity at six different positions on a single plate but also among the plates themselves. The PP plates measure $210 \times 148 \times 2.9\,\text{mm}$ and the PC plates $250 \times 105 \times 6.4\,\text{mm}$, the latter ones are also used as a substrate for the determinations of the relative permittivity of coatings in this thesis. A picture of both substrates can be seen in Fig. 3.16. Both substrate types are injection molded, however, the PP plates use multiple injection points, where the PC plates use only on point located at one of the smaller sides of the plate. First the thickness homogeneity is evaluated using a micrometer. The results of the thickness measurements for the 20 points can be seen on the in Fig. 3.17 (a). Each point represents six measurement points taken on a single plate. On the right in (b) the same graph can be seen for the six measurement points, where each point represents the same position, but distributed among all 20 plates. The first plot allows to evaluate the thickness homogeneity of the each sample itself, where the second plot can be used to evaluate the thickness fluctuation of the plates relatively to each other.

In the top part of each graph the deviation of the mean thickness of each sample can be seen relatively to the targeted thickness which measures 2.9 mm and 6.4 mm for PP

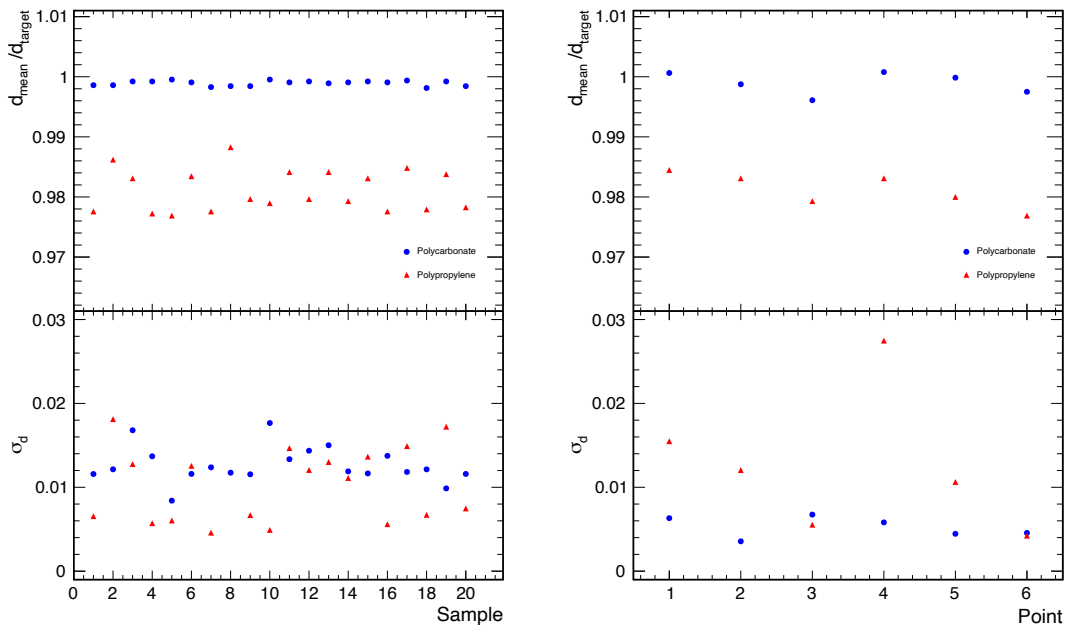

(a) (b)

Figure 3.17: Deviation from the targeted thickness and standard deviation for all 20 samples (a) and for every measurement point (b). It can be seen that PP and PC are comparable in terms of thickness homogeneity.

and PC respectively. In the lower part the standard deviation for each plate can be seen. Comparing the thickness of PP and PC it can be clearly seen that the PC substrates show less deviation from the targeted thickness specified by the manufacturer. Even though the targeted thickness is closer to specification, the fluctuation of the thickness on a single plate is comparable with the PP substrate. Comparing the thickness fluctuation on a single plate (Fig. 3.17 (a)) , however, shows that the PC plates have a similar fluctuation in thickness. In contrast to PC, the PP substrate shows that not only the thickness fluctuates on a single plate but also across all samples. Although a high homogeneity in thickness is favourable for using the substrate for permittivity determinations, possible inhomogeneities can be compensated by local thickness measurements, which are performed as a consequence. However, the dielectric behavior is much more important for utilizing the substrate for permittivity determinations as well as part of a radome or bumper. The real part of the relative permittivity of all samples as well as of the six measurement point across the samples can be seen in Fig. 3.18. Unlike the thickness, the real part of the relative permittivity shows a much more homogenous

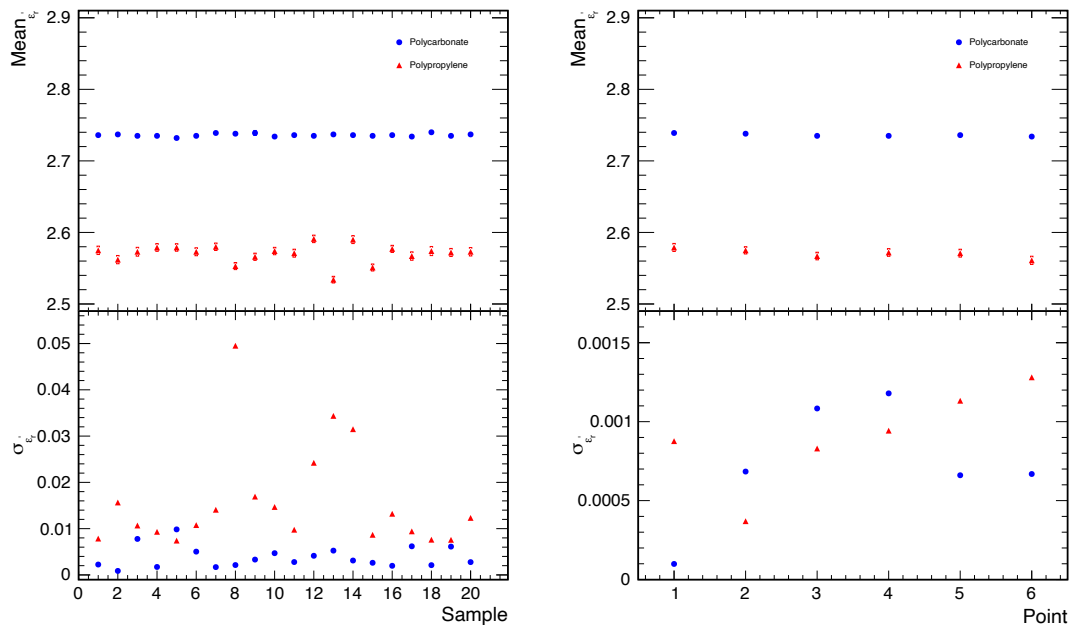

(a) (b)

Figure 3.18: Mean and standard deviation of the real part of the relative permittivity for all 20 samples (a) and for every measurement point (b). It can be seen that PC shows a more homogenous dielectric behavior than PP on a single plate, but not across the samples.

behavior for the PC plates as for the PP ones. This can be seen by looking at the mean value as well as the standard deviation. On the other hand, evaluating the six points across the samples, shows that the fluctuation of both substrates shows very low values. The same can be also stated by looking at Fig. 3.19, where the loss tangent is shown. It shows that even though, the thickness of both substrates shows a similar fluctuation, the dielectric fluctuation is smaller for PC. As stated before, an inhomogeneity in thickness can be compensated by measuring the thickness at the same location, where the actual measurement with the VNA is taken. The PC substrate clearly shows a more dielectric homogeneity, which is crucial for using the substrate for permittivity determinations. This is caused by the fact that the dielectric properties are determined once and assumed to be constant for all substrate plates. The substrate material used for determining the dielectric properties of the coating is characterized by using the average value of all 20 samples with six measurements points each. An overview of the mean values of the thickness as well ε_r' and $\tan\delta$ for PP and PC can be found in Table 3.6.

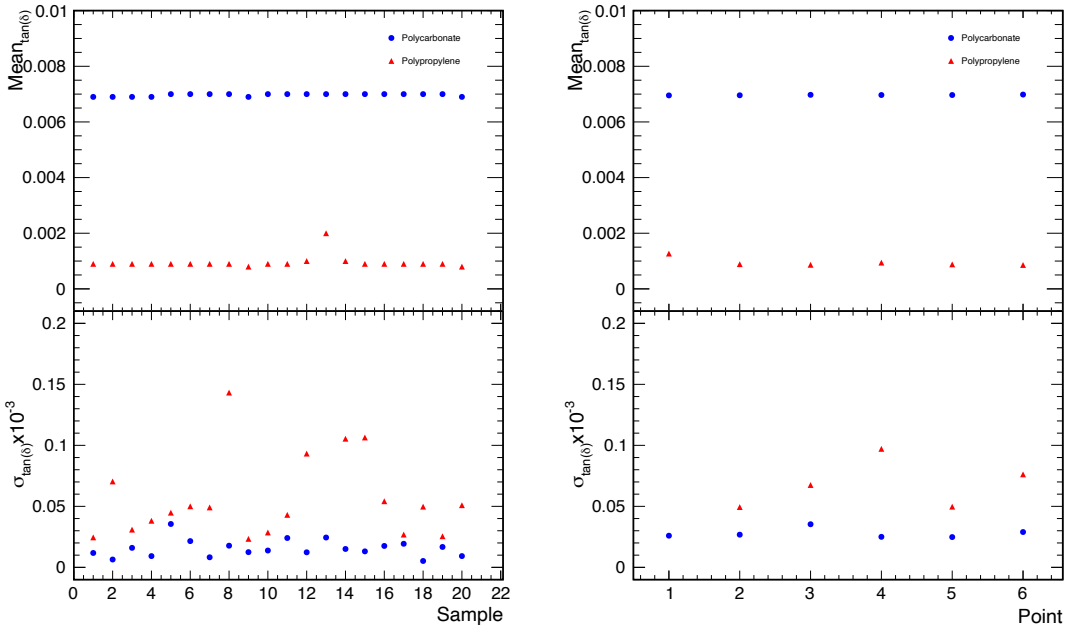

(a) (b)

Figure 3.19: Mean and standard deviation of the loss tangent for all 20 samples (a) and for every measurement point (b). It can be seen that PC shows a slightly more homogenous dielectric behavior than PP on a single. However, the differences are extremely small.

Substrate	Thickness (mean) [mm]	ε_r' (mean)	$\tan\delta$ (mean)
PC	$6.393 \pm 3.0 \cdot 10^{-3}$	$2.736 \pm 2.8 \cdot 10^{-3}$	$7.0 \cdot 10^{-3} \pm 4.8 \cdot 10^{-6}$
PP	$2.845 \pm 3.0 \cdot 10^{-3}$	$2.571 \pm 5.4 \cdot 10^{-3}$	$1.0 \cdot 10^{-3} \pm 9.1 \cdot 10^{-6}$

Table 3.6: Comparison of the thickness, real part of the relative permittivity and the loss tangent of the PP and PC substrate

The difference in fluctuation of ε_r' and $\tan\delta$ between PP and PC is mainly caused by the injection molding process in conjunction with the rheology of the materials. The different standard deviations of both substrates can be found in Table 3.7. The standard deviation includes all measurement points across all plates, amounting to 120 measurement points for each substrate type in total. In conclusion PC is the superior material from a dielectric perspective, therefore, it is used as a substrate material for all material characterizations within this thesis.

Substrate	σ_d	$\sigma_{\varepsilon'_r}$	$\sigma_{\tan\delta}$
PC	$12.1 \cdot 10^{-2}$	$4.4 \cdot 10^{-3}$	$2.9 \cdot 10^{-5}$
PP	$16.4 \cdot 10^{-2}$	$21.7 \cdot 10^{-3}$	$62.1 \cdot 10^{-5}$

Table 3.7: Comparison of the standard deviations of the PP and PC substrate

3.7 Resonant Design of Samples

One of the main problems of hidden integration of radar sensors behind painted bumpers or radomes, is the associated reflection. The reflection is caused by the difference in permittivity of air and the material. In Section 2.3 it is shown that a higher permittivity leads to a higher reflection, which impacts the performance of the sensor. However, the reflection can be reduced by exploiting a resonant design of a radome or a bumper. In theory there are different ways to achieve a resonance in the desired frequency range, either by adjusting the thickness or the permittivity itself. Since the latter one is extremely unpractical, aiming for a resonant thickness is a common way to reduce the reflection between radar and radome or painted bumper. In the simple case of single layer structure the resonance frequency is given by [62]

$$f = m\frac{c_0}{2dn}, \tag{3.16}$$

with $m = 1, 2, 3, ...$, d being the thickness and n the refractive index. Expressed as a function of the thickness d and using the permittivity and permeability, the equation becomes

$$d_{res} = m\frac{c_0}{2f}\frac{1}{\sqrt{\varepsilon_{\mathrm{r},l}\mu_{\mathrm{r},l} - \sin^2(\alpha)}}. \tag{3.17}$$

The angle α defines the angle of incidence and d_{res} describes the resonant thickness. This equation can be simplified further for automotive coatings by assuming a non magnetic behavior. Again a wave perpendicular to the surface can simplify the expression further to

$$d_{res} = m\frac{c_0}{2f}\frac{1}{\sqrt{\varepsilon'_{\mathrm{r}}(1 - j\,\tan\delta)}}. \tag{3.18}$$

The reflection and transmission for the PC substrate with increasing thickness can be seen in Fig. 3.20, the frequency is set to 76.5 GHz.

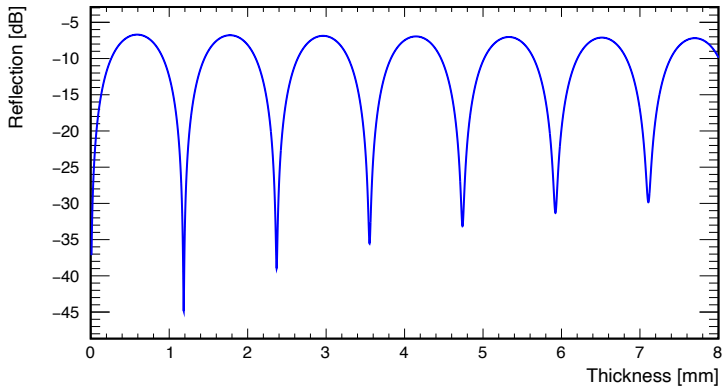

(a)

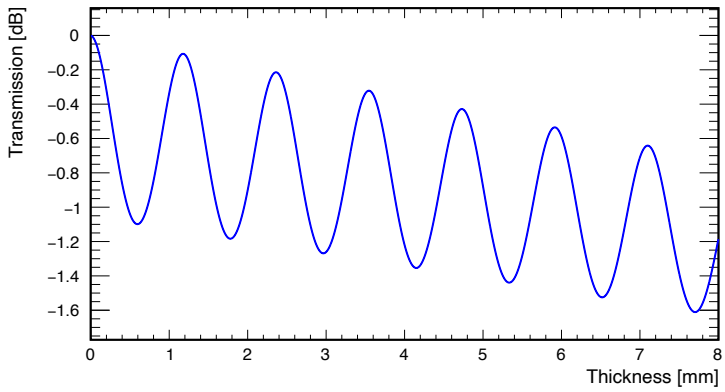

(b)

Figure 3.20: a) Change of Reflection with increasing thickness of PC substrate. b) Change of transmission wit increasing thickness for PC substrate. The frequency is set to 76.5 GHz.

The position of the resonance and therefore the resonant thickness can be estimated by $n\lambda_0/2\sqrt{\varepsilon} = n\lambda_m/2$, when including all simplifications, which are assumed before. It can be seen that the resonant thickness is given by a multiple of $\lambda_m/2$, where the wavelength describes the wavelength in the respective medium. As mentioned before, this simple method can only be used for single layer samples. For multilayer scenarios, the sample has to be modeled e.g. with the transmission line model described in Section 3.5. However, many radomes still consist of a single layer plastic substrate, especially when the sensor is located in the lower air intake in the front. For bumpers, using a resonant thickness is unpractical, since the thickness would have to change depending on the color. Furthermore, bumpers have to fulfill certain thickness requirements given by safety regulations. Fulfilling the resonance condition precisely requires very involved designs, unfeasible for mass production painted bumpers. This is mainly caused by the fact that the tolerances when applying automotive coatings are too high. For design

radomes resonances are achieved with great effort and cost utilizing PVD layers, avoiding the tolerances problem.

3.8 Differences in Permittivity of Water- and Solvent-borne Basecoats

Depending on the region, either basecoats based on solvent or water are used. Since both variants exist, possible differences for the radar sensor need to be investigated. In this section the differences in ε_r' and $\tan\delta$ are evaluated to determine the impact on the radar transparency. All results are taken from work, supervised within the framework of this thesis [63]. As a result, the same methods and measurement setups are used as presented in this chapter. Solvent-borne basecoats use a solvent as a diluent. After the application, the diluent evaporates, which does not require an additional step to fully cure the coating. In addition, the application process can be carried out under less controlled ambient temperature and conditions [64] [65]. However, solvent-borne basecoats are usually more expensive than the water based counterpart and are more harmful to the environment. Therefore, usually water based basecoats are more commonly used especially in series production, where a controlled environment and temperature can be achieved. As the name implies, water based basecoats use water as a diluent. Since the water does not evaporate in such a short time as a solvent, the basecoat has to cure at relatively high temperatures. Due to the high surface tension of water, the application is far more complex than for solvent-borne basecoats [65]. The basecoats studied in this section are gray, red, light blue, dark blue and green. For each basecoat, the water- and solvent-borne variant is measured. The results obtained using the VNA setup can be seen in Table 3.8, the results using the RMS setup in Table 3.9. A comparison shows that water-borne basecoats show a higher real part of the relative permittvity than solvent-borne basecoats. The difference is rather small, varying from 0.5 to 3.16 when including VNA and RMS data. Furthermore, the difference is not scaling with the permittivity, which is expected since the contents of the basecoat have to be very similar to achieve the same optical appearance. Looking at the loss tangent, it can be seen that no clear picture can be drawn if water-borne basecoats or solvent-borne basecoats shows higher radar transparency. All the values are in the same order of magnitude, with the RMS showing slightly higher values. The higher value is likely caused by the fact that the RMS uses less data as explained in Section 3.5.1. As a possible explanation for the slightly higher real part of the relative permittivity, the higher silicon concentration in water-borne basecoats compared to solvent-borne basecoats is mentioned as the root cause in [63]. The higher concentration is found utilizing energy-dispersive X-ray spectroscopy. In conclusion it can be stated that although water-borne basecoats show a higher ε_r' than solvent-borne basecoats, the difference is neglectably small and therefore for the radar sensor no difference exists between water-borne basecoats and solvent-borne basecoats.

Basecoat	ε_r' (VNA)	$\tan\delta$ (VNA)
Red WBBC	$5.080 \pm 20.4 \cdot 10^{-2}$	$2.5 \cdot 10^{-2} \pm 2.3 \cdot 10^{-3}$
Red SBBC	$4.000 \pm 17.7 \cdot 10^{-2}$	$0.4 \cdot 10^{-2} \pm 1.5 \cdot 10^{-3}$
Green WBBC	$6.788 \pm 57.6 \cdot 10^{-2}$	$7.5 \cdot 10^{-2} \pm 7.6 \cdot 10^{-3}$
Green SBBC	$5.038 \pm 34.2 \cdot 10^{-2}$	$1.6 \cdot 10^{-2} \pm 3.8 \cdot 10^{-3}$
Blue L WBBC	$11.588 \pm 23.3 \cdot 10^{-2}$	$1.7 \cdot 10^{-2} \pm 0.9 \cdot 10^{-3}$
Blue L SBBC	$9.736 \pm 66.5 \cdot 10^{-2}$	$1.9 \cdot 10^{-2} \pm 2.6 \cdot 10^{-3}$
Blue D WBBC	$5.826 \pm 28.4 \cdot 10^{-2}$	$3.0 \cdot 10^{-2} \pm 3.2 \cdot 10^{-3}$
Blue D SBBC	$5.426 \pm 28.2 \cdot 10^{-2}$	$2.4 \cdot 10^{-2} \pm 2.9 \cdot 10^{-3}$
Gray WBBC	$22.708 \pm 24.6 \cdot 10^{-2}$	$1.1 \cdot 10^{-2} \pm 1.9 \cdot 10^{-3}$
Gray SBBC	$21.832 \pm 24.2 \cdot 10^{-2}$	$2.6 \cdot 10^{-2} \pm 0.6 \cdot 10^{-3}$

Table 3.8: Results for the Solvent-Borne Basecoats (SBBC) and Water-Borne Basecoats (WBBC) using the VNA setup.

Basecoat	ε_r' (VNA)	$\tan\delta$ (VNA)
Red WBBC	$5.096 \pm 16.5 \cdot 10^{-2}$	$1.5 \cdot 10^{-2} \pm 9.4 \cdot 10^{-3}$
Red SBBC	$3.328 \pm 15.7 \cdot 10^{-2}$	$0.6 \cdot 10^{-2} \pm 6.1 \cdot 10^{-3}$
Green WBBC	$6.727 \pm 49.6 \cdot 10^{-2}$	$8.3 \cdot 10^{-2} \pm 18.4 \cdot 10^{-3}$
Green SBBC	$4.272 \pm 28.7 \cdot 10^{-2}$	$4.3 \cdot 10^{-2} \pm 15.9 \cdot 10^{-3}$
Blue L WBBC	$11.298 \pm 12.3 \cdot 10^{-2}$	$5.0 \cdot 10^{-2} \pm 7.4 \cdot 10^{-3}$
Blue L SBBC	$8.129 \pm 7.7 \cdot 10^{-2}$	$7.3 \cdot 10^{-2} \pm 7.1 \cdot 10^{-3}$
Blue D WBBC	$5.911 \pm 22.2 \cdot 10^{-2}$	$1.4 \cdot 10^{-2} \pm 8.2 \cdot 10^{-3}$
Blue D SBBC	$5.419 \pm 32.9 \cdot 10^{-2}$	$10.9 \cdot 10^{-2} \pm 15.2 \cdot 10^{-3}$
Gray WBBC	$22.928 \pm 29.4 \cdot 10^{-2}$	$5.3 \cdot 10^{-2} \pm 2.4 \cdot 10^{-3}$
Gray SBBC	$21.563 \pm 6.7 \cdot 10^{-2}$	$3.1 \cdot 10^{-2} \pm 6.4 \cdot 10^{-3}$

Table 3.9: Results for the Solvent-Borne Basecoats (SBBC) and Water-Borne Basecoats (WBBC) using the RMS setup.

CHAPTER 4

Evaluation of Influences of Paint Techniques on Radar Transparency

There are many factors which have an impact on radar transparency of radomes or bumpers. These include the choice of materials as well as the thickness of each layer. Moreover, for coatings the application technique can also influence the radar transparency. These investigations are the focus of this chapter. In total three different application systems are compared, one pneumatic and two electrostatic ones. Multiple basecoats are compared including coatings which are rather uncritical for radar such as black or white colors without effect pigments as well as silver coatings consisting of a high amount of effect pigments. In order to guarantee a supplier independent result, two different suppliers are evaluated. Since the exact contents are not revealed by the coating suppliers, this guarantees a result not influenced by unknown paint contents. All samples are painted using robots to exclude any influences caused by human imprecision. The main focus of these investigations are painted bumpers, since radomes are usually not painted with the same techniques as bumpers. Furthermore, only basecoats are investigated, since they are the main cause of possible problems for radar sensors.

4.1 Comparison of Application Techniques

The state of the art method for applying coatings in series production is an electrostatic application. This method brings multiple benefits such as less overspray (paint lost during application) and a drastically improved paint transfer efficiency. In series production, all exterior parts are painted using almost exclusively electrostatic methods. However, paint repairs in workshops are performed utilizing pneumatic methods. This is due to the fact that pneumatic methods are easier to adopt as well as less costly. For exterior parts produced with special paints in small quantities, pneumatic systems are often preferred. In this section the main differences between an electrostatic and a pneumatic system are discussed.

4.1.1 Pneumatic Application

A pneumatic spray gun uses high pressurized air to atomize the paint and transporting the resulting paint droplets on the part. Although this application system may seem to be rather simple, there are several factors influencing the application. In addition, these systems are still highly of interest in research [66] [67] [68]. Depending on the composition of the coating the air pressure as well as the spray gun trajectories have to be chosen correctly, otherwise it will result in a bad uniformity of the coating [69]. Furthermore, different air cap designs lead to different spray flow field characteristics as shown in [70]. The pressure for the pneumatic application used within this thesis is set to approximately 6 bar. The main parts of the system are a compressor, the body including different openings for the air supply as well as a fluid nozzle and the air cap. The body including the fluid nozzle mounted on a robot can be seen in Fig. 4.1.

Figure 4.1: Pneumatic application system mounted on a robot. The air cap is removed, revealing the fluid nozzle in the middle.

As mentioned before, the air cap design has a strong impact on the flow field characteristic. In general, the air cap has multiple holes including an atomizing, assisting and shaping air holes. The paint which flows through the fluid nozzle is atomized by the air flowing around the nozzle at the hole in the middle of the air cap which turns the liquid into small paint droplets. This airflow also transports the small paint droplets towards

the sample. Around the larger hole in the middle, multiple small holes are placed, which are used to change the expansion speed of the spray flow. Moreover, there are also air holes at the edge of the cap, which are also tilted towards the spray flow. These holes are primarily shaping the conical spray flow and narrowing it in one dimension. A detailed view of a air cap for pneumatic application can be seen in Fig. 4.2.

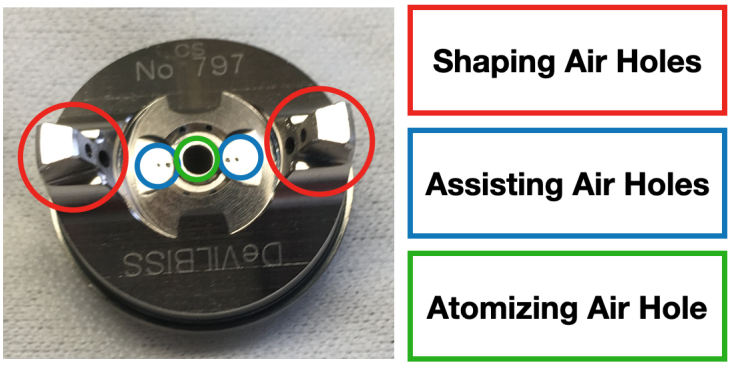

Figure 4.2: Air cap of a pneumatic application system. The different air holes are essentially influencing the spray behavior of the pneumatic application.

Besides the number of holes also the distance between the air supply holes and the tilting angle itself has an impact on the resulting spray flow. As stated before, pneumatic methods are usually used for repairing bumpers or painting small quantities of parts. However, for complex structures such as bumpers usually a pneumatic application is also used in addition after applying the largest part with electrostatic methods. This is caused by the fact that complex geometrical structures may show locations, where no paint is applied by the electrostatic method.

4.1.2 Electrostatic Rotary-Bell Application

For the electrostatic application, two different systems from two different manufacturers are used. The systems differ mainly in the type of charging process for the paint. In general, the main parts of an electrostatic application system include a bell cup, a turbine, an air supply similar to the pneumatic application system and electrodes. The bell cup is shaped like a conical disc, with the paint being injected into the center. A picture of a bell cup can be seen in Fig 4.3. The turbine rotates the bell cup at around 50.000 rpm, forcing the injected paint to the edge of the cup and subsequently, a thin film of paint forms. The exact speed strongly depends on the properties of the coating. The small film is dispersed into droplets at the edge as shown in Fig. 4.3 (b), which are then transported by an air shroud towards the sample. Without the air shroud, the paint droplets would just leave the bell cup in radial direction and thus, no application would be possible.

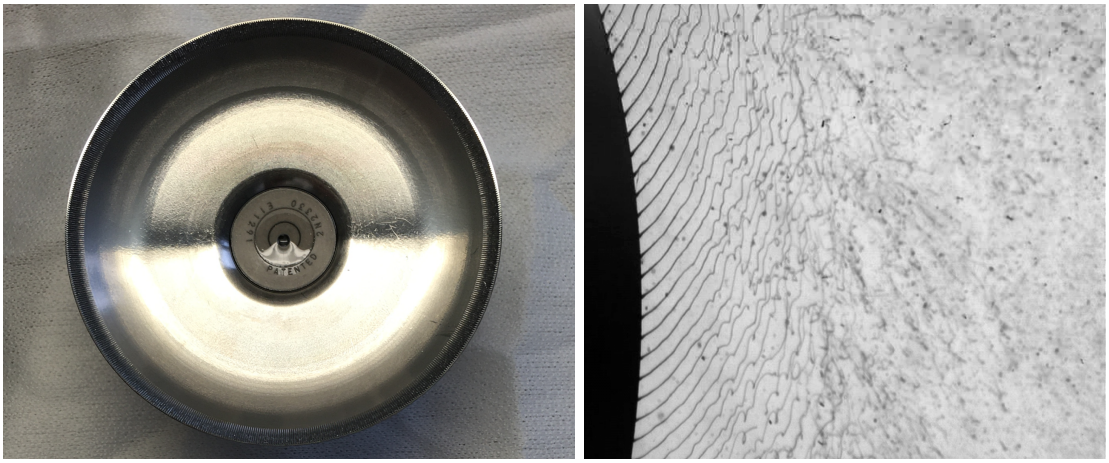

(a) (b)

Figure 4.3: (a) Dismantled bell cup. The bell cup is rotated by a turbine. As a result, the paint coming from the hole in the middle forms a small film on the bell cup. (b) Paint film breaking up and atomizing into droplets at the edge of bell cup, taken from [71].

Furthermore, the paint droplets are charged, which is either done internally or externally [72]. A schematic of both systems is shown in Fig. 4.4. Internal charging is usually applied to solvent based coatings due to their low conductivity [73]. In general, internal charging is also possible for water based coatings, by using a galvanic isolation. In order to charge the paint externally, forward facing electrodes are used, which are placed around the bell cup. The external electrodes are supplied by a high voltage up to 90.000 V, ionizing the surrounding air. When the paint droplets pass the ionizing air, they get charged. Since the paint droplets are charged negatively and the sample is grounded or charged positively, an electrostatic attraction emerges. Also a repulsion between the paint droplets itself can be observed, which results in an even spread of the coating across the sample. One of the used systems in this chapter is internally charged the other one externally, a picture of both application systems can be seen in Fig. 4.5. Similar to the pneumatic application, also the electrostatic method has multiple parameters, which have to be fine tuned for an optimal coating application. In addition to drag forces from the focusing air also electromagnetic forces have to be considered. However, in [74] it was shown that the droplet trajectory is mostly dominated by the drag forces. The field of electrostatic rotary-bell application is a subject of research for many years, in order to understand all influences of all parameters [75] [76] [77].

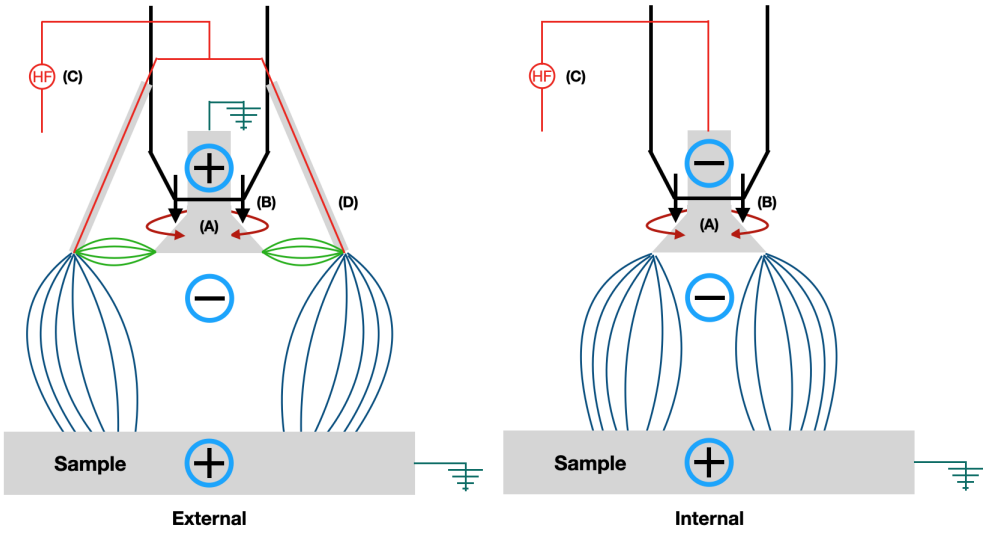

Figure 4.4: Scheme of electrostatic application system. (A) rotary bell cup, (B) air supply, (C) high voltage source, (D) external electrodes.

(a) (b)

Figure 4.5: a) External charged application system b) Internal charged application system. Both systems are shown without bell cup.

4.2 Evaluation of Best Technique for Hidden Sensor Integration

In order to evaluate the best suited paint application technique for a hidden integration behind a painted bumper the relative permittivity is used. As shown in Section 2.3, a lower permittivity is favourable, since it leads to less reflections between the sensor and the radome or bumper respectively. The different application techniques are evaluated using the permittivity as well as micrographs, pictures obtained from a Scanning Electron Microscope (SEM) as well as Energy-Dispersive X-ray (EDX) spectroscopy. The latter ones are used to find a possible explanation for differences between the application techniques.

4.2.1 Change of Permittivity for Different Applications

The real part of the relative permittivity and the loss tangent are evaluated using the transmission line model described in Section 3.5. Since all investigated coatings are water based, a clearcoat is required. Therefore, each sample consists of three layers (PC substrate, basecoat, clearcoat). For the basecoats, various colors are chosen in order to investigate the effect of paint application techniques with increasing permittivity. The substrate and clearcoat are the same for all samples. In total, three samples for each color are painted, one with a pneumatic application (PNM) and two with Electrostatic rotary-bell application (ESTA 1, ESTA 2). The system utilizing the internal charge system will henceforth be called ESTA 1, the system utilizing an external charge system ESTA 2. As mentioned before, two different paint suppliers are used for the same basecoats to guarantee independent results. Since not all basecoats are available from the second supplier not all basecoats can be compared. However, the most important basecoats showing low and high amounts of effect particles such as aluminum and mica are investigated. To provide results independent of the measurement device, VNA as well as RMS measurements are considered. The values for the permittivity obtained by the VNA represent an average over six measurement points, for the RMS only one measurement point is considered due to the design of the device and a small sample. The results for the ε_r' can be seen in Table 4.1. Comparing the values of the real part of the relative permittivity for the three application techniques, it can be seen that the electrostatic rotary-bell application always shows a lower ε_r' than the pneumatic one. This implies that ESTA 1 and ESTA 2 provide a more radar compatible basecoat application. The only exception is given by the black basecoat, which does not show a change of ε_r' for the different application techniques within the uncertainty. Comparing the two electrostatic methods, ESTA 2 shows a lower ε_r' for most of the basecoats, the only exceptions being the silver and turquoise basecoat. The ESTA methods showing a lower ε_r' that the PNM method can also be observed for both paint suppliers. This effect is also seen within the RMS data. The improvement when comparing a PNM and an ESTA application scales with the base ε_r' of the basecoats. This shows that problematic coatings for radar such as silver profit more from an ESTA application than e.g. a white basecoat. The results of the $\tan\delta$ for the different application techniques can be seen in

Table 4.2. It can be clearly seen that the application technique has no impact on the loss tangent. The change is either very small or not existent within the uncertainty.

Basecoat	ε'_r (PNM)	ε'_r (ESTA 1)	ε'_r (ESTA 2)
Black (VNA)	$3.700 \pm 22.1 \cdot 10^{-2}$	$3.934 \pm 32.3 \cdot 10^{-2}$	$3.968 \pm 28.3 \cdot 10^{-2}$
White S1 (VNA)	$5.841 \pm 20.5 \cdot 10^{-2}$	$5.803 \pm 25.7 \cdot 10^{-2}$	$5.125 \pm 18.9 \cdot 10^{-2}$
White S2 (VNA)	$5.901 \pm 27.1 \cdot 10^{-2}$	$5.755 \pm 21.7 \cdot 10^{-2}$	$5.295 \pm 17.3 \cdot 10^{-2}$
Green S1 (VNA)	$5.352 \pm 23.5 \cdot 10^{-2}$	$4.847 \pm 23.4 \cdot 10^{-2}$	$4.464 \pm 20.2 \cdot 10^{-2}$
Green S2 (VNA)	$5.324 \pm 48.4 \cdot 10^{-2}$	$5.308 \pm 33.3 \cdot 10^{-2}$	$4.832 \pm 27.0 \cdot 10^{-2}$
Blue S1 (VNA)	$7.795 \pm 24.0 \cdot 10^{-2}$	$7.357 \pm 33.9 \cdot 10^{-2}$	$5.732 \pm 21.1 \cdot 10^{-2}$
Blue S2 (VNA)	$8.286 \pm 46.3 \cdot 10^{-2}$	$7.513 \pm 27.6 \cdot 10^{-2}$	$6.806 \pm 25.0 \cdot 10^{-2}$
Gray S1 (VNA)	$15.897 \pm 22.9 \cdot 10^{-2}$	$13.252 \pm 25.0 \cdot 10^{-2}$	$10.428 \pm 23.1 \cdot 10^{-2}$
Gray S2 (VNA)	$21.140 \pm 40.2 \cdot 10^{-2}$	$17.774 \pm 24.6 \cdot 10^{-2}$	$17.437 \pm 25.0 \cdot 10^{-2}$
Silver (VNA)	$24.011 \pm 96.3 \cdot 10^{-3}$	$17.215 \pm 13.1 \cdot 10^{-2}$	$17.883 \pm 14.8 \cdot 10^{-2}$
Turquoise (VNA)	$27.122 \pm 29.1 \cdot 10^{-2}$	$15.785 \pm 23.2 \cdot 10^{-2}$	$16.863 \pm 25.8 \cdot 10^{-2}$
Black (RMS)	$3.672 \pm 21.3 \cdot 10^{-2}$	$3.918 \pm 31.9 \cdot 10^{-2}$	$3.967 \pm 25.9 \cdot 10^{-2}$
White S1 (RMS)	$5.922 \pm 17.5 \cdot 10^{-2}$	$5.705 \pm 25.7 \cdot 10^{-2}$	$4.887 \pm 17.5 \cdot 10^{-2}$
White S2 (RMS)	$6.101 \pm 19.2 \cdot 10^{-2}$	$5.842 \pm 28.3 \cdot 10^{-2}$	$5.162 \pm 18.4 \cdot 10^{-2}$
Green S1 (RMS)	$5.149 \pm 23.5 \cdot 10^{-2}$	$4.205 \pm 21.8 \cdot 10^{-2}$	$3.727 \pm 20.5 \cdot 10^{-2}$
Green S2 (RMS)	$5.304 \pm 21.4 \cdot 10^{-2}$	$4.509 \pm 23.7 \cdot 10^{-2}$	$4.012 \pm 23.6 \cdot 10^{-2}$
Blue S1 (RMS)	$7.250 \pm 20.7 \cdot 10^{-2}$	$7.464 \pm 33.0 \cdot 10^{-2}$	$5.704 \pm 20.7 \cdot 10^{-2}$
Blue S2 (RMS)	$7.864 \pm 23.8 \cdot 10^{-2}$	$7.742 \pm 25.2 \cdot 10^{-2}$	$5.626 \pm 21.5 \cdot 10^{-2}$
Gray S1 (RMS)	$15.883 \pm 16.6 \cdot 10^{-2}$	$12.604 \pm 24.3 \cdot 10^{-2}$	$9.989 \pm 21.5 \cdot 10^{-2}$
Gray S2 (RMS)	$16.051 \pm 20.4 \cdot 10^{-2}$	$13.002 \pm 25.1 \cdot 10^{-2}$	$10.401 \pm 23.4 \cdot 10^{-2}$
Silver (RMS)	$22.918 \pm 26.7 \cdot 10^{-2}$	$16.326 \pm 12.2 \cdot 10^{-2}$	$17.029 \pm 10.2 \cdot 10^{-2}$
Turquoise (RMS)	$26.140 \pm 31.2 \cdot 10^{-2}$	$16.023 \pm 24.1 \cdot 10^{-2}$	$18.207 \pm 21.6 \cdot 10^{-2}$

Table 4.1: Values for the real part of the relative permittivity evaluated from data obtained from VNA and RMS measurements for different basecoats. For some basecoats two suppliers (S1 and S2) are compared.

Basecoat	$\tan\delta$ (PNM)	$\tan\delta$ (ESTA 1)	$\tan\delta$ (ESTA 2)
Black (VNA)	$(79.5 \pm 6.4) \cdot 10^{-3}$	$(95.5 \pm 10.0) \cdot 10^{-3}$	$(95.9 \pm 8.8) \cdot 10^{-3}$
White S1 (VNA)	$(38.0 \pm 2.6) \cdot 10^{-3}$	$(46.2 \pm 3.5) \cdot 10^{-3}$	$(42.5 \pm 2.8) \cdot 10^{-3}$
White S2 (VNA)	$(39.2 \pm 3.4) \cdot 10^{-3}$	$(43.1 \pm 7.0) \cdot 10^{-3}$	$(37.2 \pm 8.4) \cdot 10^{-3}$
Green S1 (VNA)	$(47.4 \pm 3.4) \cdot 10^{-3}$	$(46.7 \pm 3.6) \cdot 10^{-3}$	$(44.8 \pm 3.5) \cdot 10^{-3}$
Green S2 (VNA)	$(51.8 \pm 4.1) \cdot 10^{-3}$	$(48.5 \pm 11.2) \cdot 10^{-3}$	$(51.9 \pm 8.6) \cdot 10^{-3}$
Blue S1 (VNA)	$(47.9 \pm 2.8) \cdot 10^{-3}$	$(60.2 \pm 4.3) \cdot 10^{-3}$	$(47.5 \pm 3.0) \cdot 10^{-3}$
Blue S2 (VNA)	$(48.3 \pm 5.4) \cdot 10^{-3}$	$(46.7 \pm 7.3) \cdot 10^{-3}$	$(51.2 \pm 6.9) \cdot 10^{-3}$
Gray S1 (VNA)	$(34.4 \pm 0.7) \cdot 10^{-3}$	$(33.6 \pm 1.3) \cdot 10^{-3}$	$(36.7 \pm 1.9) \cdot 10^{-3}$
Gray S2 (VNA)	$(41.5 \pm 1.6) \cdot 10^{-3}$	$(37.8 \pm 4.2) \cdot 10^{-3}$	$(35.2 \pm 5.8) \cdot 10^{-3}$
Silver (VNA)	$(30.3 \pm 0.1) \cdot 10^{-3}$	$(28.6 \pm 0.5) \cdot 10^{-3}$	$(29.1 \pm 1.4) \cdot 10^{-3}$
Turquoise (VNA)	$(52.6 \pm 0.9) \cdot 10^{-3}$	$(34.8 \pm 0.9) \cdot 10^{-3}$	$(58.4 \pm 1.1) \cdot 10^{-3}$
Black (RMS)	$(82.7 \pm 11.9) \cdot 10^{-3}$	$(81.7 \pm 16.0) \cdot 10^{-3}$	$(68.3 \pm 11.9) \cdot 10^{-3}$
White S1 (RMS)	$(33.2 \pm 7.2) \cdot 10^{-3}$	$(40.9 \pm 8.2) \cdot 10^{-3}$	$(37.0 \pm 7.0) \cdot 10^{-3}$
White S2 (RMS)	$(37.5 \pm 5.4) \cdot 10^{-3}$	$(42.7 \pm 7.0) \cdot 10^{-3}$	$(41.6 \pm 8.4) \cdot 10^{-3}$
Green S1 (RMS)	$(24.1 \pm 8.7) \cdot 10^{-3}$	$(50.2 \pm 9.4) \cdot 10^{-3}$	$(58.5 \pm 10.7) \cdot 10^{-3}$
Green S2 (RMS)	$(34.2 \pm 5.4) \cdot 10^{-3}$	$(31.7 \pm 6.1) \cdot 10^{-3}$	$(36.2 \pm 6.3) \cdot 10^{-3}$
Blue S1 (RMS)	$(56.7 \pm 8.6) \cdot 10^{-3}$	$(42.3 \pm 10.0) \cdot 10^{-3}$	$(37.4 \pm 8.6) \cdot 10^{-3}$
Blue S2 (RMS)	$(52.3 \pm 8.4) \cdot 10^{-3}$	$(59.2 \pm 6.3) \cdot 10^{-3}$	$(56.2 \pm 4.7) \cdot 10^{-3}$
Gray S1 (RMS)	$(19.6 \pm 5.7) \cdot 10^{-3}$	$(33.1 \pm 7.3) \cdot 10^{-3}$	$(31.3 \pm 7.2) \cdot 10^{-3}$
Gray S2 (RMS)	$(23.5 \pm 6.7) \cdot 10^{-3}$	$(32.4 \pm 3.4) \cdot 10^{-3}$	$(34.2 \pm 5.8) \cdot 10^{-3}$
Silver (RMS)	$(38.5 \pm 3.8) \cdot 10^{-3}$	$(12.5 \pm 6.4) \cdot 10^{-3}$	$(34.9 \pm 6.0) \cdot 10^{-3}$
Turquoise (RMS)	$(41.2 \pm 4.2) \cdot 10^{-3}$	$(39.8 \pm 6.1) \cdot 10^{-3}$	$(45.1 \pm 8.2) \cdot 10^{-3}$

Table 4.2: Values for the real part of the loss tangent evaluated from data obtained from VNA and RMS measurements for different basecoats. For some basecoats two suppliers (S1 and S2) are compared.

4.2.2 Investigation of Basecoat Contents

In order to understand the reason for ESTA applications showing a lower ε_r' and critical basecoats showing a higher improvement, the contents of the basecoat have to be investigated. Since coating suppliers keep the contents of their coatings secret, different methods are used to extract the necessary information. These methods include micrographs, SEM as well as EDX spectra. Despite obviously differentiating in color and appearance, the main difference between the basecoats is based on the contents. Especially the effect pigments, including concentration, material and size heavily influence the permittivity. One of the main elements, which drastically increases the permittivity is aluminum. The change of permittivity with increasing aluminum concentration is shown in [78] for aluminum filled epoxy resins as well as for metallic basecoats [49]. Especially silver basecoats show a high amount of aluminum resulting in a critical permittivity from radar perspective.

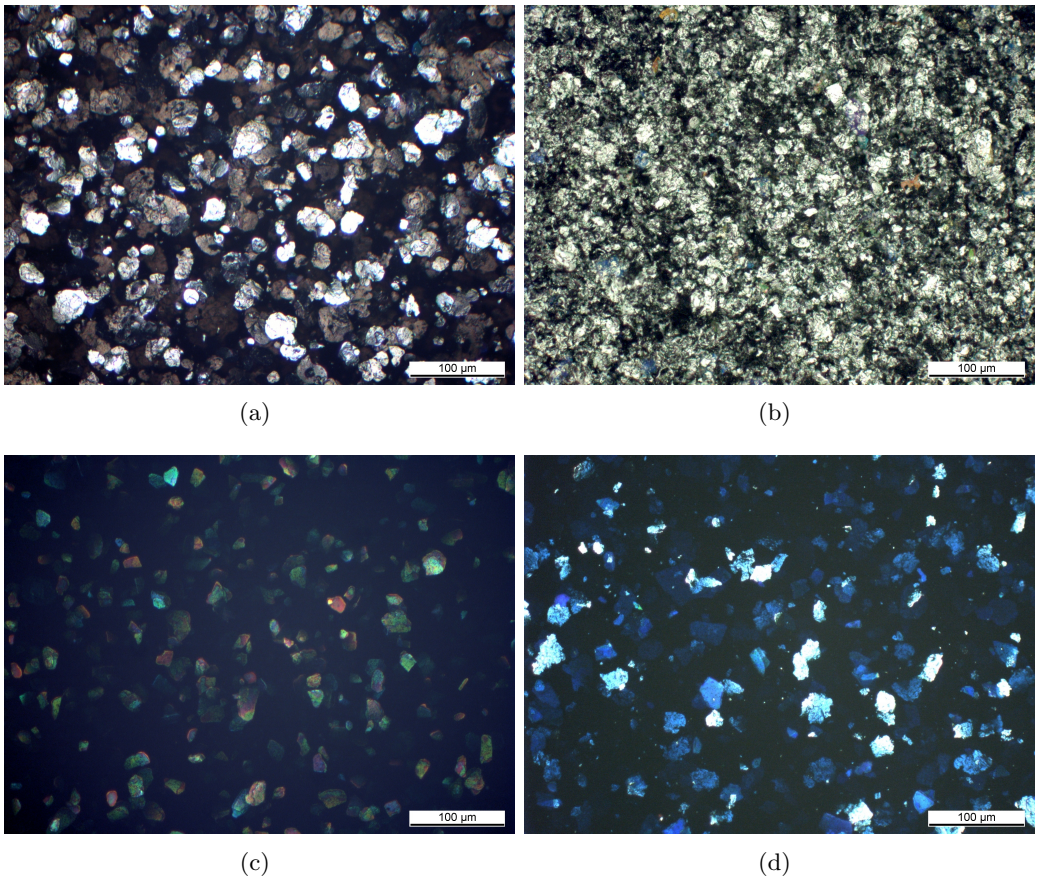

(a) (b)

(c) (d)

Figure 4.6: Magnification of different basecoats using the PNM application. All pictures are taken using the same samples as for the permittivity determination. As a result, all pictures are recorded through a layer of clearcoat. (a) Gray. (b) Silver. (c) Green. (d) Blue.

In Fig. 4.6 different magnifications for basecoats applied with PNM application can be seen for the gray, silver, green and blue basecoat. The high amount of aluminum can be clearly seen for the gray and the silver basecoat. Furthermore, the different concentration as well as the size of the flakes is also visible. Although alumiunium is present in every silver or coatings similar to silver, also mica particles show a high occurence in almost all colors, such as green and blue as seen in Fig 4.6 (c) and (d). In addition to this, often a mix of aluminum and mica particles is used to set accents in the appearance. This can be observed for the silver basecoats, where clearly blue mica particles can be seen in a small quantity, resulting in a slightly blueish appearance when looking at the car from different point of views. It can be stated that the amount of improvement in the permittivity when using PNM and ESTA application is strongly correlated with the amount of effect pigments. As a result, the silver basecoat shows a higher improvement when compared to the green or blue basecoat.
In order to understand the composition of different basecoats in more detail, EDX spectra are recorded. The EDX spectra are obtained using a SEM. The main principle of EDX spectroscopy is based on electron beams which get focused on the desired area. The unexcited electrons get stimulated subsequently, which results in an injection of the electron from the inner shell. As a result, an electron hole is created, which gets filled by an electron from an outer shell. This results in the electron from the outer shell emitting X-rays corresponding to the energy difference between the shell where the electron hole was created and the shell, where the electron filling the hole was placed originally [79]. Since most of the atoms have multiple shells, also multiple peaks in the EDX-spectrum may exist [80]. In order to get a good impression of the contents of the basecoats investigated in this chapter, black, white, green, blue and gray are investigated using the SEM in conjunction with the EDX-spectrum. Since all samples have clearcoat on top of the basecoat, the sample is cut in order to have access to the side of the layers.

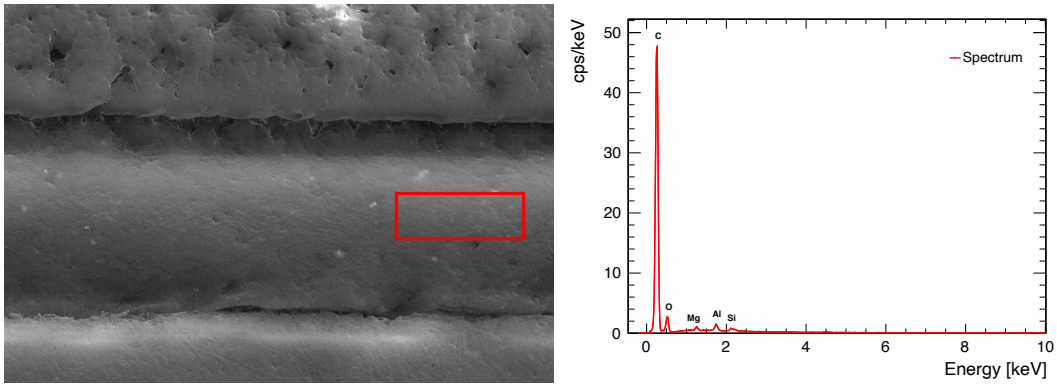

(a) (b)

Figure 4.7: REM and corresponding EDX diagram of black basecoat. The red square refers to the area, where the EDX spectrum is evaluated.

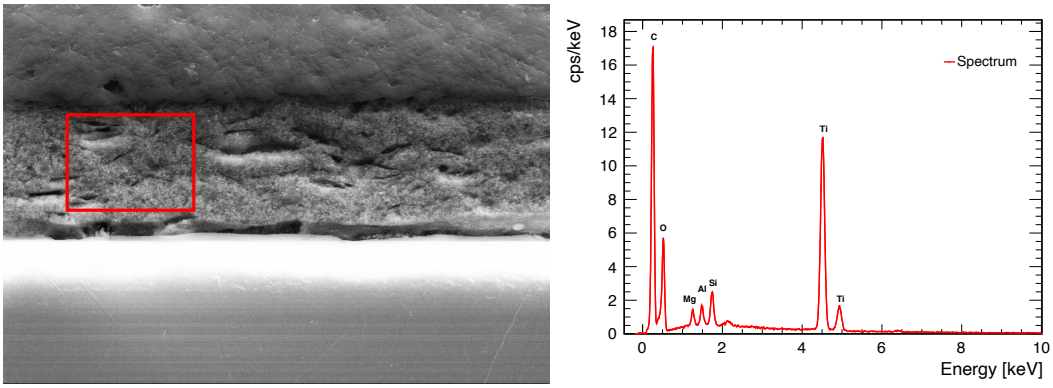

(a) (b)

Figure 4.8: REM and corresponding EDX diagram of white basecoat.

Looking at the EDX spectrum for the black basecoat, shown in Fig. 4.7, it can be seen that the dominant element is carbon, which also gives the basecoat its black appearance. In addition, the SEM picture shows a very homogenous layer, with no effect pigments. The small dots which can be seen are gold particles used for sputtering, since the samples are non conductive and therefore no SEM recordings would be possible. Since the black basecoat showed a rather low ε_r' between three and four, it can be concluded that carbon is not a critical element for radar. Similar to the black basecoat, the white basecoat also does not show effect pigments. However, a granulated structure can clearly be observed. This structure is caused by the crystalline shape of TiO_2, which is the main element found in the white paint besides carbon. The SEM picture and EDX spectrum of the white basecoat can be found in Fig. 4.8. The ε_r' shows higher values for the white basecoat than for the black basecoat, this shows that TiO_2 definitely has a higher impact on radar transparency than carbon.

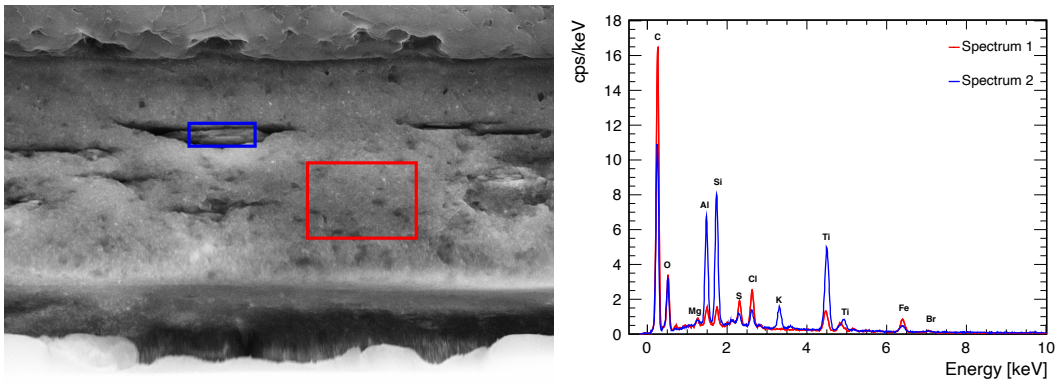

(a) (b)

Figure 4.9: REM and corresponding EDX diagram of green basecoat.

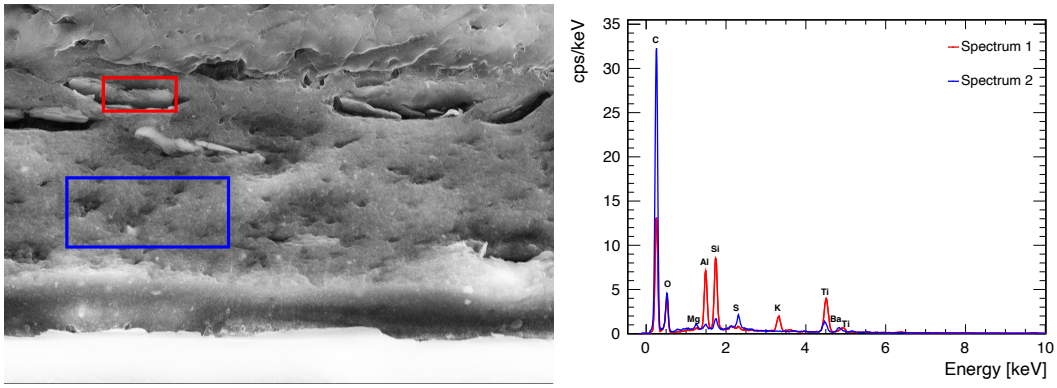

(a) (b)

Figure 4.10: REM and corresponding EDX diagram of blue basecoat.

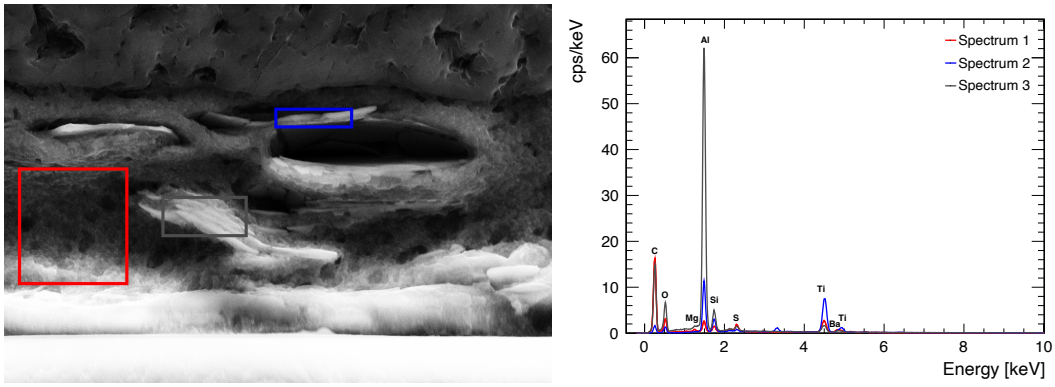

(a) (b)

Figure 4.11: REM and corresponding EDX diagram of gray basecoat.

For the green, blue and gray basecoats, multiple EDX spectra are taken due to the fact that the mentioned basecoats include effect pigments. Compared to the white basecoat, the green basecoat shows less TiO_2, however, more aluminum, which results in a comparable permittvity overall. The green color of the basecoat originates not only from the flake itself but also from the material, where the flakes are embedded. This is due to the fact that a relatively high amount of chlorine is present, as seen in the EDX spectra shown in Fig. 4.9. The spectrum of the mica particle clearly shows a plethora of different elements, which is typical for mica particles. The main elements include aluminum, silicon, titanium as well as the corresponding oxides. The latter one is present in composite with silicon or titanium or iriodin particles, which are trademarked mica particles coated in a wafer-thin layer of metal oxide [81]. The blue basecoat shows a similar composition to the green coating, the exception being chlorine. The composition of the flakes is nearly identical as shown in Fig. 4.10. Although the composition is very

similar, the ε_r' is slightly higher, which can be mainly explained by the fact that the blue basecoat shows a higher concentration of effect pigments. The gray basecoat clearly shows two different effect pigment types. This can be seen in the EDX spectrum in Fig. 4.11. The first type of pigments are aluminum flakes, which can be identified by the large peak in the EDX spectrum. The second pigments are mica particles, showing a similar composition to other mica particles found in the green and blue basecoat. However, the mica pigments in the gray basecoat show a higher share of aluminum than silicon, where the opposite holds true for the green and blue basecoat. The gray basecoat shows the highest permittivity when compared to the blue and green basecoat. The EDX spectrum and SEM picture shows that this is clearly caused by a high aluminum as well as mica concentration. This can also be seen in the magnified picture shown in Fig. 4.6.
In conclusion basecoats including effect pigments such as mica, aluminum or iriodin, share an extremely similar embedding. The only exception are slight changes to change the appearance, an example being chlorine for the green basecoat. The main difference, which also strongly influences the resulting permittivity are the effect pigments. Especially aluminum shows a high impact, resulting in the basecoat having a significantly higher permittivity than the other investigated coatings. Furthermore, the gray basecoat also shows the highest concentration of effect pigments.

4.2.3 Interpretation of Change in Permittivity

In this section, it is shown that the permittivity changes with different paint application techniques. Electrostatic rotary-bell applications show a lower ε_r' when compared to a pneumatic application. In the last subsection the contents of basecoats are investigated and it is observed that the permittivity strongly depends on the concentration and type of effect pigments. In order to identify the impact of the different application techniques on the basecoats, micrographs are taken. To investigate a possible change of orientation of flakes, for each basecoat a micrograph is made in longitudinal and transverse direction. Since the difference in permittivity for different paint techniques is more present for coatings with a high amount of effect pigments, migcrographs for the silver and gray basecoat are shown in Fig. 4.12 and Fig. 4.13 respectively.
Comparing the PNM application with the ESTA 1 and 2 application, it can be seen that less effect pigments are present for the ESTA application than for the PNM one. This can be seen for the longitudinal as well as the traversal micrograph. Furthermore, the effect pigments tend to be smaller in size for the ESTA application. For the gray basecoat a similar effect can be seen. Since the effect pigments are in general larger compared to the silver basecoat and less flakes are present by design the effect does not apply as strong as for the silver basecoat. However, an additional effect can be observed. For the PNM application the effect pigments can pile up to bulks, where for the ESTA applications, they are more evenly distributed within the coating, which is a result of the applied charge of the ESTA methods. This effect is present for the longitudinal but not for the transverse direction. The main question is, how these effects can influence the permittvity.

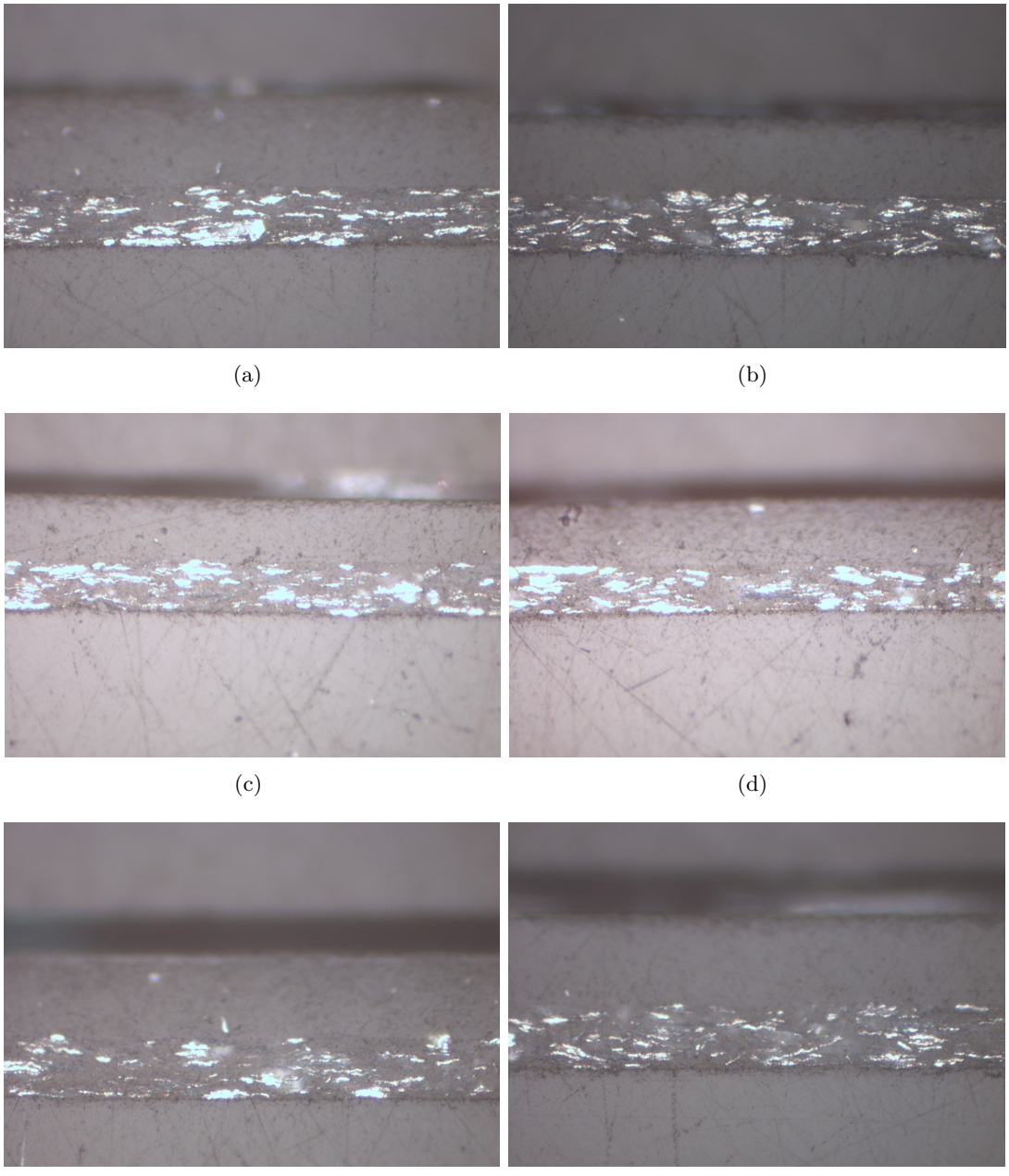

(a) (b)

(c) (d)

(e) (f)

Figure 4.12: Micrographs for silver basecoat for PNM, ESTA1 and ESTA2 applications.

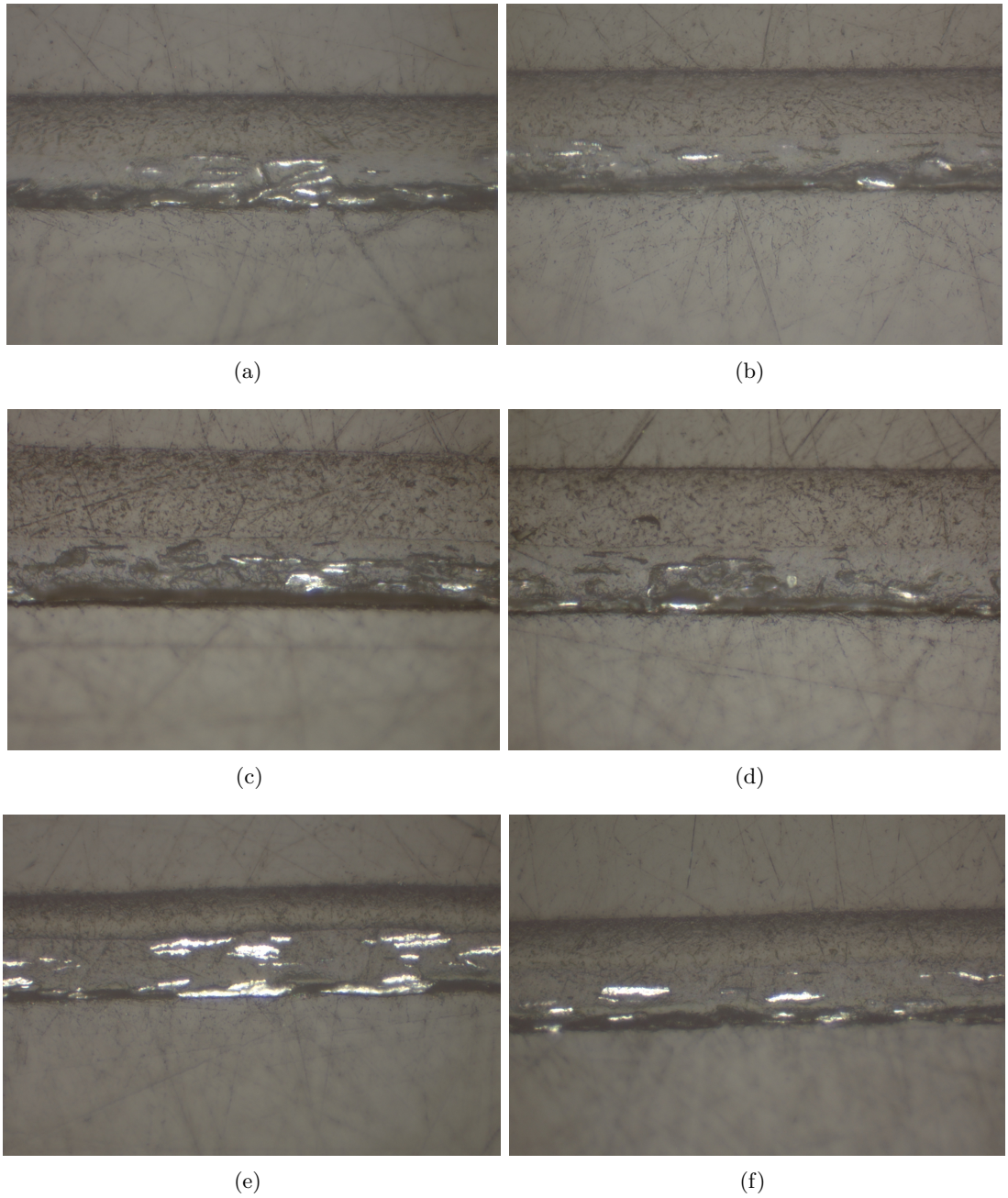

(a) (b)

(c) (d)

(e) (f)

Figure 4.13: Micrographs for gray basecoat for PNM, ESTA1 and ESTA2 applications.

The main difference between the PNM and ESTA application besides charging the paint is the fact that ESTA application utilize a turbine in conjunction with a bell cup to generate a thin paint film, which is then atomized into small droplets, and transported towards the sample by the air shroud. Depending on the speed of the rotating bell cup, effect pigments may be pushed into the overspray due to centrifugal forces. Since this force scales linearly with the mass of the particles, larger paint droplets tend to be lost due to overspray and smaller and therefore lighter paint droplets will be applied to the sample. As a result, large effect pigments e.g. aluminum flakes will not be applied to the sample. This results in a lower aluminum concentration in the basecoat and therefore a lower permittivity. For the PNM application on the other hand, small droplets containing small effect pigments tend to be lost in the overspray and larger droplets will be applied to the sample more likely. This increases the aluminum concentration in contrast to the ESTA application and therefore also the permittvity. These effects were also mentioned in [82]. Larger particles likely being pushed into overspray when using ESTA application can also be validated by simulation as shown in Fig. 4.14.

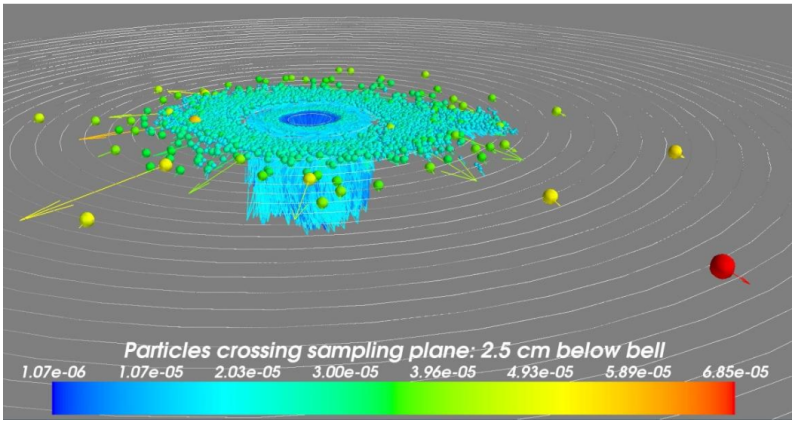

Figure 4.14: Simulation of an electrostatic rotary-bell applicator. The simulation is performed 2.5 cm below the bell cup. The simulation clearly shows that larger particles are pushed into overspray due to the rotation of the bell cup. Taken from [73].

The more effect pigments are present in the basecoat, the larger the difference between the PNM and ESTA application. Within this chapter also basecoats are investigated without any effect pigments and thus the effect described before does not apply. Furthermore, except the silver and the turquoise basecoat, the ESTA 2 method always shows a lower permittivity than the ESTA 1 application. The difference in permittvity for basecoats without effect pigments such as the white basecoat can be explained by the fact that the high pressure of the PNM application results in a denser application overall, compressing the material. As mentioned before, the white basecoat consists of granular particles of TiO_2 as seen in Fig 4.15 (a). The higher pressure of the PNM application results in denser packed TiO_2 particles and as a result, a higher permittivity is observed. The black basecoat, shows no improvement by an ESTA application, which results from

an extremely homogenous structure of the basecoat as seen in Fig. 4.15 (b). Since no difference is visible in the micrograph only the PNM longitudinal pictures are shown.

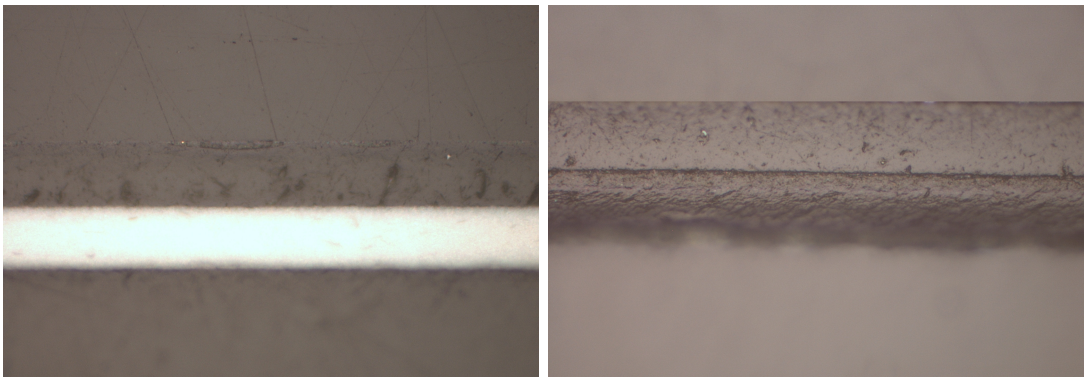

(a) (b)

Figure 4.15: Micrograph for white (a) and black (b) basecoat. The granular structure of the white basecoat is clearly visibly as well as the homogenous one of the black basecoat. The gold dots are leftovers of the gold used for the SEM after polishing the samples in order to reuse them for the microscope.

Comparing the ESTA 1 and ESTA 2 application, shows that ESTA 2 generally shows smaller values for ε_r' than ESTA 1. An exception being, as mentioned before, the silver and turquoise basecoat, where the difference is very small. This can also be explained by the difference in density caused by different pressures. The ESTA 1 application operates at 13 bar, where ESTA 2 only uses 6 bar. This results in a generally lower permittvity with ESTA 2 than ESTA 1. The silver and turquoise basecoat show the highest amount of effect pigments of all basecoats investigated in this chapter. As a result, the concentration of effect pigments is very high and dense and therefore the higher pressure of the ESTA 1 application shows a weaker impact when compared to basecoats with less effect pigements.

4.3 Concluding Remarks

In this chapter it is shown that electrostatic rotary-bell applications show a lower permittivity than pneumatic applications and therefore a higher radar transparency. The amount of improvement strongly depends on the amount of effect pigments. Especially coatings containing a high amount of aluminum and mica particles benefit from an ESTA application. As mentioned at the beginning of this chapter, in series production both paint techniques are used in conjunction. Therefore, in order to improve the radar transparency in series production, the ratio of PNM and ESTA application could be adjusted. Moreover, basecoats applied by hand in small numbers are often suffering from a high permittivity. Applying these basecoats with ESTA applications can improve the radar transparency. It should be noted however, that an ESTA application might change the

appearance of the coating compared to the PNM application. For the basecoats investigated in this chapter, this is observed for the turquoise basecoat, which is caused by less effect pigments being present in the basecoat.

CHAPTER 5

Influences of Automotive Coatings on Sensor Performance

A painted radome or bumper in front of the radar sensor can cause various problems including a decreased detection range as well as deviations when estimating angles. These effects range from a decreased performance to an unusable signal, depending on the permittivity of the material and coatings. The decrease in range can simply be estimated as shown in Section 2.4. However, for possible angle estimations, there is no simple analytical way to estimate a possible deviation. In this chapter, the angular deviation caused by the same basecoats already investigated in Chapter 4 is examined. In addition, the influence on object separation is studied.

5.1 Angular Deviation and Error in Object Separation

In this section, an experimental radar setup is used to determine the angular deviation caused by different basecoats. The basecoat is applied to two different ABS substrates with different thicknesses. One substrate shows a more resonant behavior for a center frequency of 76.5 GHz than the other. This allows to evaluate the benefit of a resonant substrate after applying coatings. All basecoats are applied using the same ESTA application technique. In particular, the ESTA 1 application is used utilizing an internal charge process. An ESTA application guarantees a very homogenous coating application. In order to examine possible reflection reducing effects, the painted substrates are also measured tilted relatively to the sensor. To examine a possible influence on object separation, two corner reflectors are used with variable distance to each other, in order to find the point, where the two objects are just barely separable by the sensor. It should be mentioned that the investigations performed in this section strongly depend on the sensor itself. Therefore, the results are only valid for the used experimental radar. The main goal of this section is to examine possible influences on a physical level.

5.1.1 Configuration of Experimental Radar

As a FMCW MIMO radar evaluation platform, the INRAS Radarbook2 with a 77 GHz frontend is used. This experimental radar allows choosing an individual configuration, which can be adapted to the desired measurement scenario. The used frontend consists of 2 TX and 16 RX antennas. The RX antennas are spaced $\lambda_0/2$ apart. The TX antennas are spaced $15\lambda_0/2$, resulting in a virtual antenna array of 32 elements, with one element overlapping. The wavelength λ_0 refers to the free space wavelength at 77 GHz. The overlapping element can be used for motion compensation [83]. However, since such compensations are not necessary for the measurements performed within this thesis, the overlapping element is not used, reducing the available elements to 31. The antennas on the used frontend are only separated horizontally and not vertical and thus azimuth and elevation angle estimations are not possible simultaneously. A scheme of the virtual antenna array with overlapping element can be seen in Fig. 5.1. The used evaluation platform operates from 76 - 77 GHz, utilizing 1 GHz bandwidth, which results in a range resolution of 15 cm. The configuration is adopted from [84] with slight modifications, since a newer version of the Radarbook is used. In total 256 chirps are sent for each frame, with a ramp-up time $t_{\text{up}} = 32\,\mu\text{s}$ and a ramp-down time $t_{\text{down}} = 12\,\mu\text{s}$. A summary of the used values can be found in Table 5.1. In order to create the virtual antenna array, the two TX antenna are operated alternately. To enable fast measurement times, the raw data of both TX antennas is recorded and processed further offline.

Description	Symbol	Value
Start Frequency	f_{start}	76 GHz
Stop Frequency	f_{stop}	77 GHz
Sweep Frequency	B	1 GHz
Number Transmit Antennas	TX	2
Number Receive Antennas	RX	16
Number Utilized Channels	N_{channel}	31
Ramp-Up time	t_{up}	32 µs
Ramp-Down time	t_{down}	12 µs
Number of Chirps	N_{chirp}	256

Table 5.1: Configuration of Radarbook2 with 77 GHz frontend. The configuration is adopted from [84], with slight adjustments.

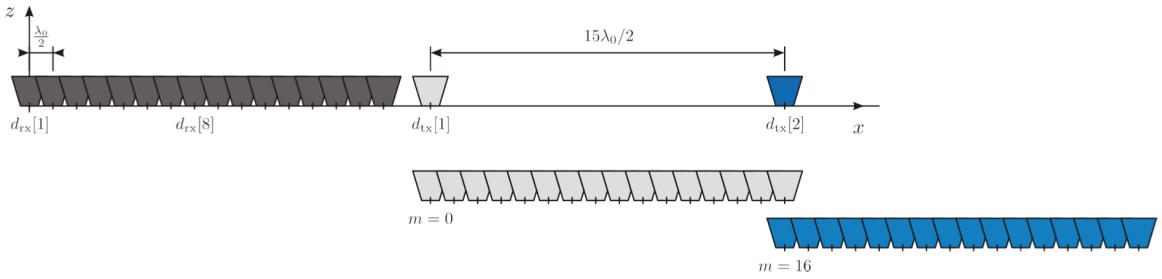

Figure 5.1: Antenna array and virtual elements for the used experimental radar. The overlapping element can be used for motion compensation. Taken from [85].

5.1.2 Measurement Setup and Procedure

All measurements are performed indoor. This is mainly caused by the fact that the used radar sensor shows a high temperature sensitivity, which will falsify the measurement. Due to limited space and therefore reflections from the walls or other obstacles, a absorber tunnel is used. This tunnel guarantees a clean signal, not distorted by other objects from the surroundings. The tunnel measures approx. 1.5 m in length. As a target, a dSPACE DARTS target simulator is used. Using a target simulator instead of a simple corner cube brings the benefit that the signal can be delayed to an arbitrary distance, depending on the available cable length. For this thesis the signal is delayed to approx. 4.5 m. This is primarily done to improve the signal quality, since the target simulator is placed in front of an absorber wall. Although the absorber wall shows a very good absorption, small reflections are still visible. Since these reflection fall within the same range bin as the actual target, the signal used for the measurements might be disturbed. In order to evaluate the angular deviation caused by the painted sample under different angles, the radar sensor is mounted on a rotatable stand with a bracket to mount the sample. The stand enables a rotation between $\pm 19.8°$ with a step size of $0.9°$, resulting in a total of 44 steps. Higher and lower angles are not feasible due to high reflection caused by the direct reflection between the sensor and the inside of the absorber tunnel due to acute angles. A schematic of the setup can be found in Fig. 5.2.
The measurements are performed as follows. For each individual basecoat, one measurement is taken over the whole angular range without a sample in front of the sensor. The next measurement is performed using the bare substrate without a coating applied. In the last step, the painted sample is measured. This procedure allows to compare the angular deviation caused by the bare substrate as well as the painted sample relatively to the angle estimated without a sample in front of the sensor and to the angle seen with an unpainted substrate. Since this setup does not allow to precisely determine the angular deviation seen by the sensor itself, all shown measurements are based on a relative measurement. However, for a relative comparison of the basecoats this represents the most expedient solution. For each angular bin 15 frames are measured and averaged.

Each measurement is conducted three times and subsequently averaged as well. The angle is then estimated as the mean of a gaussian fit applied to the target scene shown in Fig. 5.3

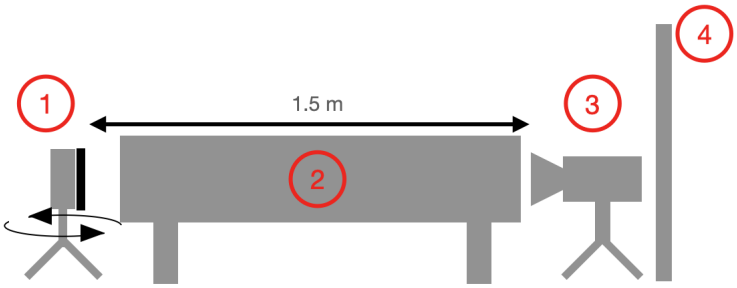

Figure 5.2: Schematic of measurement setup: 1) Radar with radome, 2) Tunnel with absorber, 3) Target simulator, 4) Absorber wall.

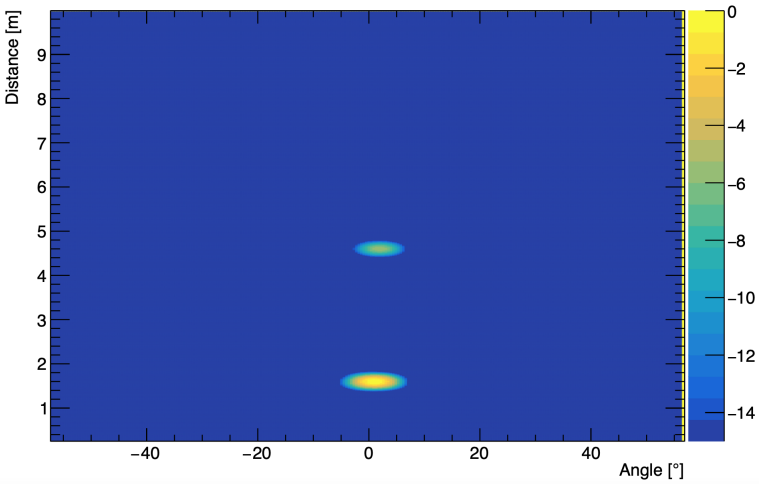

Figure 5.3: Range angle heatmap of the target scenery. The target is positioned boresight relative to the sensor. The signal at approx. 1.5 m is the actual target, the signal at approx. 4.5 m the delayed signal, used for evaluating the angle. The heatmap shows arbitrary units with higher values indicating higher reflections.

Applying a fit instead of simply using the highest point, guarantees an independence of the angular binning. The target simulator is positioned centered to the radar sensor, as a result the TX horn antenna of the target simulator is slightly offset, which shifts the delayed signal as seen in the range angle map. However, since only relative measurements are conducted, as mentioned before, no negative impact is expected. In total, the seven different basecoats, already investigated in Chapter 4, are measured and applied to two

substrates measuring a difference in thickness. Also possible effects caused by tilted samples are investigated. Therefore, each sample is measured tilted 0° as well as 10°. Furthermore, two different distances between the sample and the sensor are used. The first measures 2 cm, the second 5 cm.

5.1.3 Material Characterization of used Samples

As a substrate material ABS is used. In order to evaluate the influence of the thickness of the substrate, despite the influence of different basecoats, two different thicknesses are used. The first substrate measures 2.277 mm, the second one 2.347 mm. All basecoats are applied using the ESTA 1 application and are manufactured by the first supplier mentioned in Chapter 4. Since all the basecoats are water based, a clearcoat is needed. All samples are fitted with a metal strip to determine the thickness of basecoat and clearcoat using the method described in Section 3.2.1. The metal stripe is placed in such way that the radar measurements are not deteriorated.

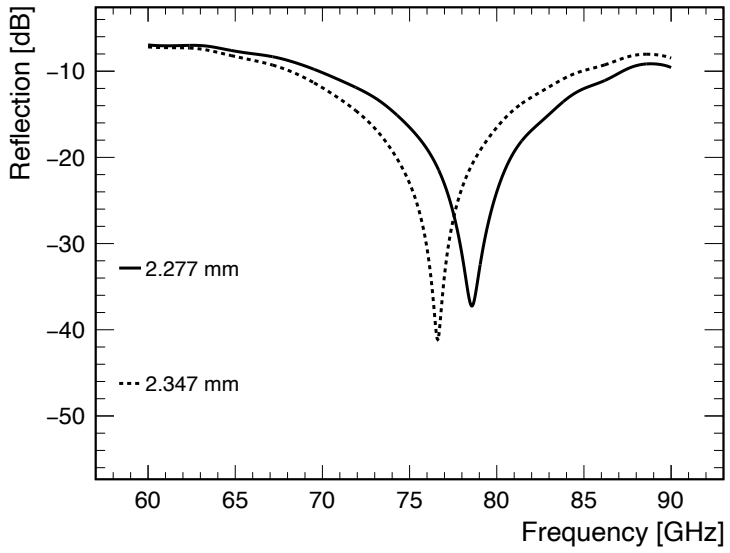

Figure 5.4: Reflection of the two substrates ABS substrates. The reflection is measured using a VNA. The thicker substrate shows a resonance between 76 - 77 GHz and therefore a higher radar transparency.

Although the information of the thickness of each layer is not needed as an input for the performed measurements, they are used to guarantee a similar coating thickness for all samples, which makes comparing the angular deviation based on the real part of the permittivity possible. Since it is expected that basecoats with a higher permittivity also result in a higher reflection and therefore a higher angular deviation, all reflections are measured using the VNA setup described in Section 3.3.1. The reflection for the substrates can be seen in Fig. 5.4.

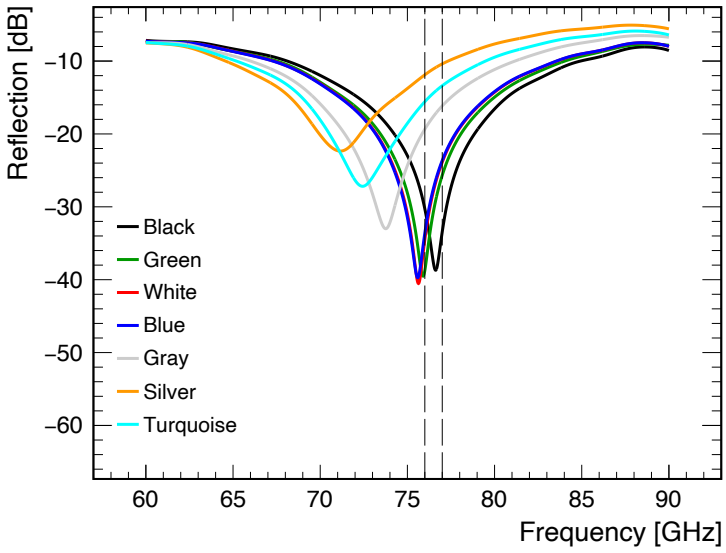

(a)

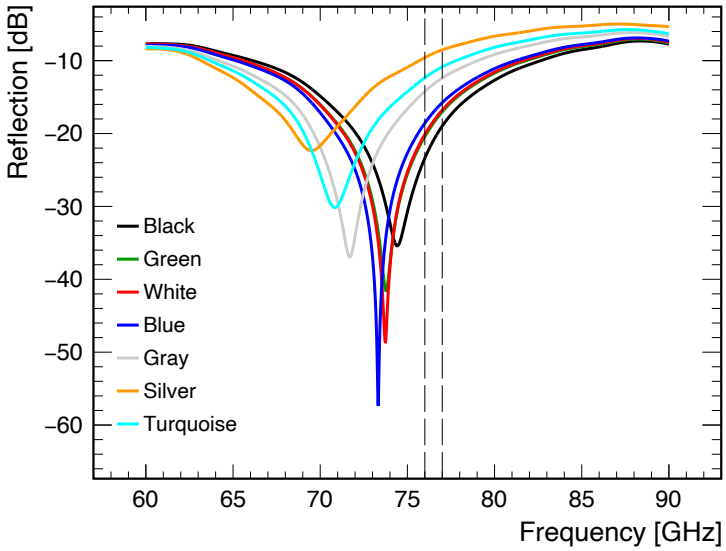

(b)

Figure 5.5: a) Reflection of VNA measurement of painted samples on thinner substrate. For coatings with lower permittivity a resonance can be observed between 76 - 77 GHz, indicated by the vertical dashed line. b) Reflection of VNA measurements for painted samples on the thicker substrate. The previously existing resonance between 76 - 77 GHz of the bare substrate is shifted to lower frequencies by the coating.

It can be seen that the thicker substrate is resonant within 76 - 77 GHz, which is the used frequency range of the radar sensor in this chapter. The thinner substrate does not have

a resonance between the desired range. In general, the substrate shows an expected low permittivity, which is determined to $\varepsilon'_r = 2.723$ and $\tan\delta = 0.0077$. These quantities are determined using the VNA measurements. Although the thicker substrate seems to be more suited for radar, this changes when the coatings are applied. The reflection recorded by the VNA for the coated samples can be seen in Fig. 5.5. It can be clearly seen that the resonance of the samples using the thinner substrate is shifted by applying the coating towards lower frequencies, into the frequency range used by the radar. The shifted resonance by the coating can also be observed for the thicker substrate, however, the shift by the coating results in resonances below the desired frequency range. This shows that designing a bumper resonant is extremely difficult due to tolerances in thickness of the substrate as well as the coating itself. As seen in both graphs, multiple substrate thicknesses would be needed to achieve a resonance for every single basecoat. As already expected, the reflection of the samples increases with increasing permittivity. The black basecoat shows the lowest permittivity and also reflection and the silver basecoat the highest. Therefore, it is also expected that the silver basecoat shows a higher angular deviation than the black one. Furthermore, samples using the thinner substrate are also expected to show a larger angular deviation due to a higher reflection between 76 - 77 GHz.

5.1.4 Angular Deviation caused by Automotive Coatings

To understand the influence of the ABS substrate itself, first the angular deviation caused by the bare substrate is evaluated. Therefore, all the data of the substrate measurements are evaluated and averaged. In total 21 measurements are taken for each of the two substrate. The 21 measurements originate from the seven different basecoats times three measurements for each basecoat. Since always the same substrate sample is used, it is sufficient enough to average over all measurements. In total, this measurement is repeated for each configuration, being 2 cm 0°, 2 cm 10°, 5 cm 0° and 5 cm 10°. The distance describes the spacing between sample and sensor, where the angle describes how much the sample is tilted relative to the sensor. In order to compare the different configuration and the angular deviation easily, the results are displayed in box plots shown in Fig. 5.6. The box contains 25 % of the distribution above and below the median. The circle represents the mean, where the whiskers indicate the data range. Comparing the two scenarios for a 0° tilting angle, it can be seen that the thicker substrate shows a lower averaged angular deviation as well as less fluctuation, which is indicated by the narrower whiskers. Increasing the spacing between sample and sensor from 2 cm to 5 cm does not influence this behavior. The mean of the angular deviation as well as the quantiles stay nearly the same. A higher fluctuation of the the data is visible for the thinner substrate, but this is most likely caused by an outlier. Comparing the 2 cm 0° measurements to the 2 cm 10° measurements shows that the tilting angle has no drastic impact on the thinner substrate. However, the thicker substrate shows a higher angular deviation. This behavior can also be observed for increasing the spacing to 5 cm. As mentioned before, the tilting is expected to reduce the reflection between the sensor and the sample. This effect is not observed to be significant for the bare

substrate. Since the permittivity increases the reflection of a material the reflection of the substrate is expected to be low beforehand. Furthermore, the differences between the two thicknesses is very small for all measurement configuration. As a result, the substrate can be considered equally homogenous as well as performing similar when put in front of the radar.

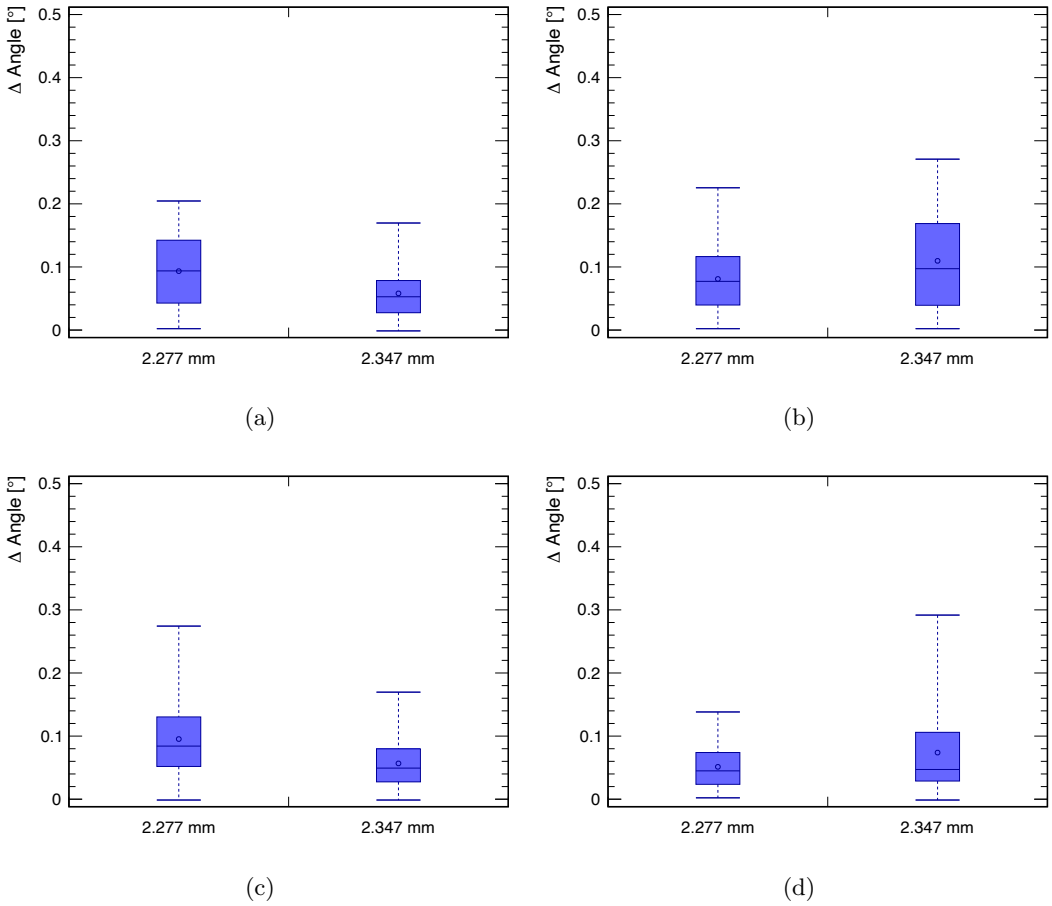

Figure 5.6: a) Results for 2 cm distance and 0° tilting angle. b) 2 cm, 10°. c) 5 cm, 0°. d) 5 cm, 10°. Although small differences between the two substrates and the different configurations is visible, no significant impact is visible. As a result, the performance of both substrates is expected to be similar.

In the following the results are discussed for the samples with coating. In Fig. 5.7, the angular deviation of the black and turquoise samples is shown. The graph shows the angular deviation for the two basecoats painted on the thinner and thicker substrate. The black line refers to the angular deviation caused by the bare substrate, where the blue line represents the deviation caused by the painted sample. The red line refers to the angular deviation of the painted sample compared to the bare substrate. The plots show the results for a spacing of 2 cm between sample and sensor and 0° tilting angle. First of

all, it can be seen that the turquoise basecoat shows a higher angular deviation than the black basecoat, which will be discussed in more detail later in this section. Furthermore, it is important to notice that the angular deviation fluctuates over the recorded range. This makes correcting the deviation by a calibration practically impossible. A linear offset on the other hand would be correctable. It can also be seen that for the thinner substrate the deviation of paint compared to the bare substrate is larger when compared to a measurement without a sample in front of the sensor (red line compared to the blue line). In addition, the red line seems to compensate the black line, which means that the paint actually reduces the angular deviation due to a thicker overall sample which shows a more resonant behavior.

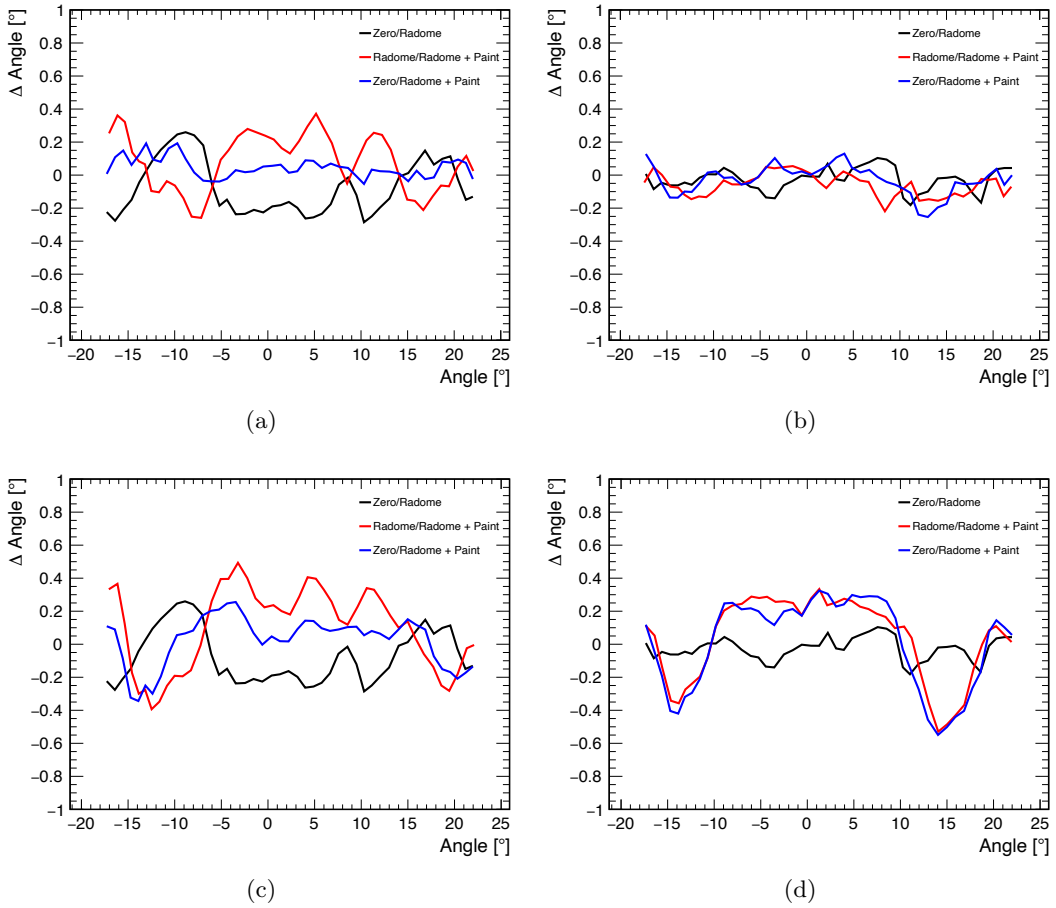

Figure 5.7: Angular deviation of the black and turquoise basecoat plotted against the range of measured angles all plots show results for 2 cm spacing between sensor and sample and 0° tilting angle. a) black basecoat on thin substrate. b) black on thick substrate. c) turquoise on thin substrate. d) turquoise on thick substrate.

In order to compare the angular deviation of all coatings similar plots are used as for the substrate. The angular deviation is now evaluated using an absolute value, since a

positive or negative deviation is equally critical for the radar sensor. The samples are sorted in ascending order with respect to the real part of the relative permittivity. In Fig. 5.8 the box plots are displayed for the samples with 2 cm spacing between sensor and sample and 0° as well as 10° tilting angle relative to measurements without a sample in front of the sensor. Looking at the box plot for 2 cm spacing and 0° tilting angle, it can clearly be seen that with increasing $\varepsilon'_{\mathrm{r}}$ also the angular deviation increases. However this can only be stated for the silver and turquoise basecoat for the thinner and also gray for the thicker substrate. These samples show the three highest permittivities within the examined basecoats. Samples painted with a lower permittivity basecoat are mostly fluctuating in the similar range of angular deviation. Despite an increase in angular deviation, also the fluctuation increases indicated by the larger quantiles as well as whiskers. For the box plot showing the measurements for the 10° tilting angle, it can be seen that the increasing angular deviation with increasing permittivity vanishes. This is caused by the tilting angle reducing reflections between the sample and the sensor. As mentioned before, due to the high permittivity a high reflection is expected, which results in a standing wave pattern between the sample and the sensor. A wave reflected by the actual target will interfere with these standing waves resulting in a phase shift and subsequently in an angular deviation seen by the sensor. All samples measured with a 10° tilting angle show similar performance. The results for a 0° and 10° tilting angle and 5 cm cm spacing between the sensor and sample are discussed in the following. The measurements can be seen in Fig. 5.9. For a 0° tilting angle it can be seen again that a higher permittivity leads to a higher angular deviation. In contrast to the 2 cm 0° measurements, the samples with the thinner substrate show a higher angular deviation and a higher fluctuation. As a result, it can be stated that the small difference in thickness although changing the reflection between 76 - 77 GHz, is neglectable. Clearly, the high permittivity of the basecoat is what results in a significant influence on the angular deviation. Similar to the tilting at 2 cm distance, no influence of the permittivity can be seen anymore. The average value of the angular deviation shows a fluctuation independent of the permittivity with all samples having a comparable data distribution, according to the sizes of the boxes and the whiskers. It is stated before that the influence of the substrate itself is expected to be low according to the shown measurements. In order to validate this further, the plots shown in Fig. 5.10 and Fig. 5.11 show the same results but all angular deviations are relative to the deviation already seen by the bare substrate. Again, at 0° tilting angle the angular deviation increases with permittivity, independent of the spacing between sensor and sample. Also for a 10° tilting angle the same can be stated as before. Tilting the sample reduces the angular deviation due to the fact that the reflections between sensor and sample are reduced. No influence of the permittivity can be seen when tilting the sample in terms of performance. In conclusion, the substrate shows indeed no significant influence on the angular deviation when compared to the basecoat. In order to compensate for the angular deviation caused by a high permittivity, the radome or the bumper should be tilted to reduce this effect. A significant effect caused by different spacings between sensor and sample is not observed.

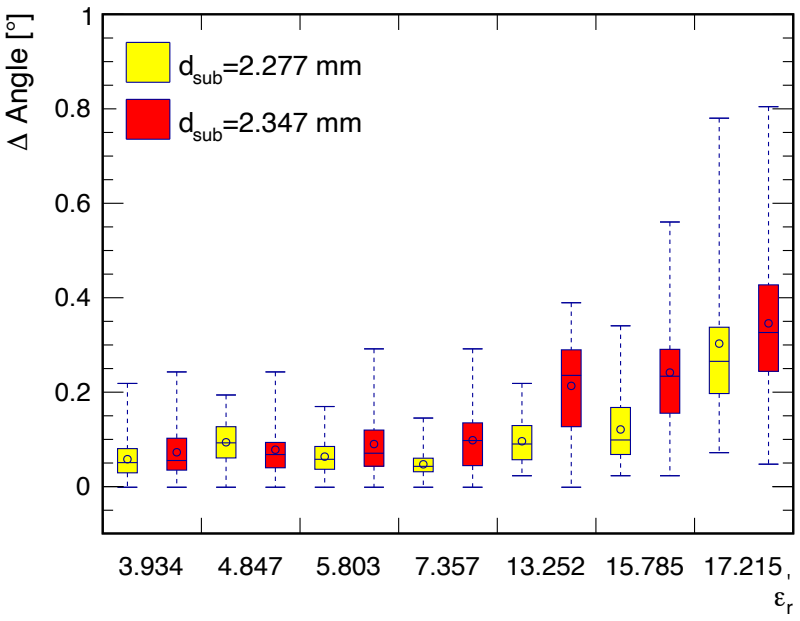

(a)

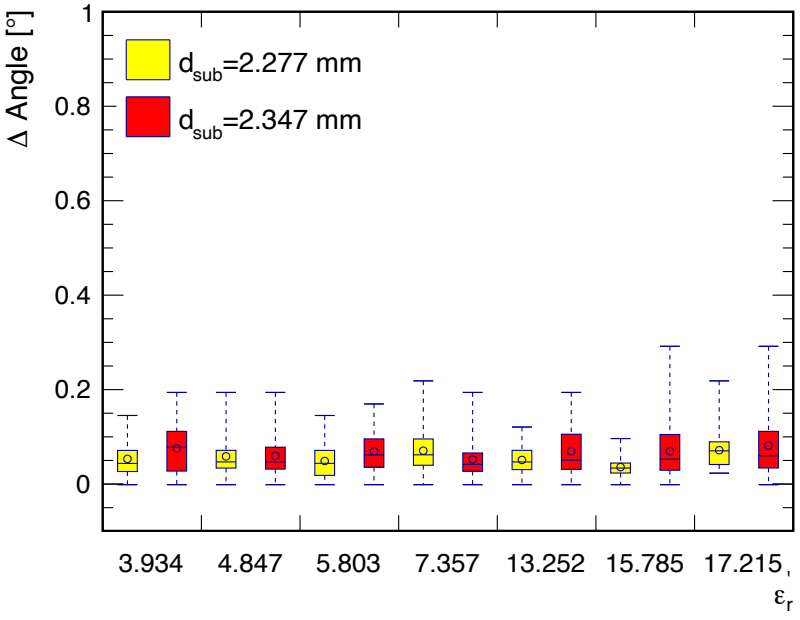

(b)

Figure 5.8: Angular deviations relative to measurement without sample. Yellow and red boxes within one bin on the x-axis have the same ε_r'. a) 2 cm distance and 0° tilting. b) 2 cm distance and 10° tilting.

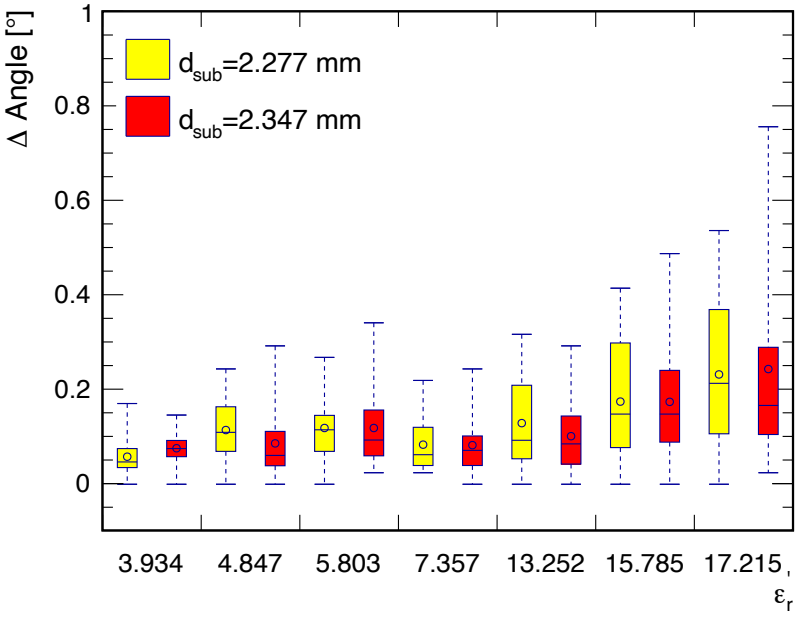

(a)

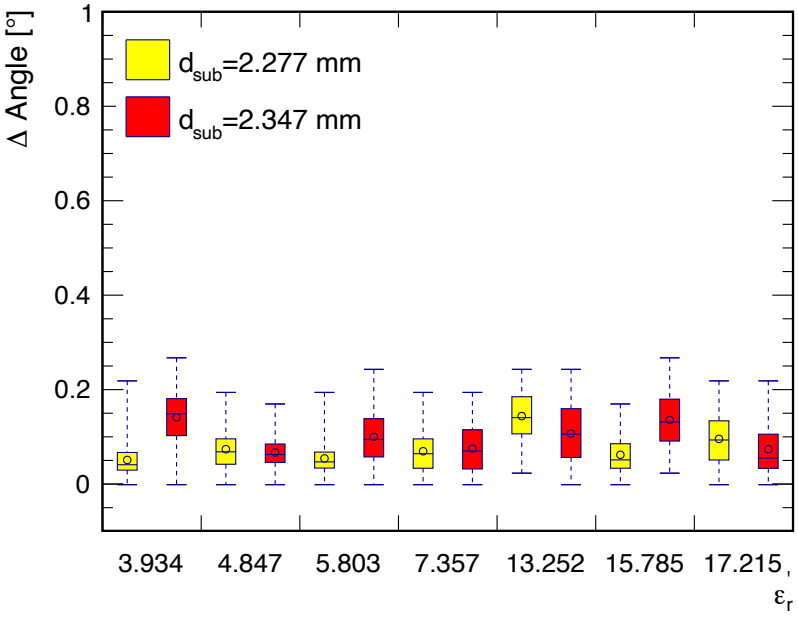

(b)

Figure 5.9: Angular deviations relative to measurement without sample a) 5 cm distance and 0° tilting. b) 5 cm distance and 10° tilting.

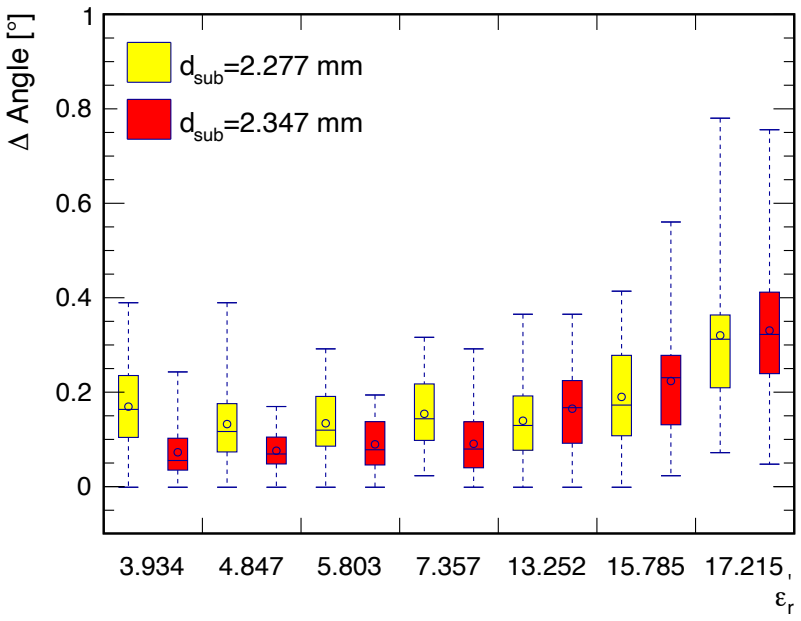

(a)

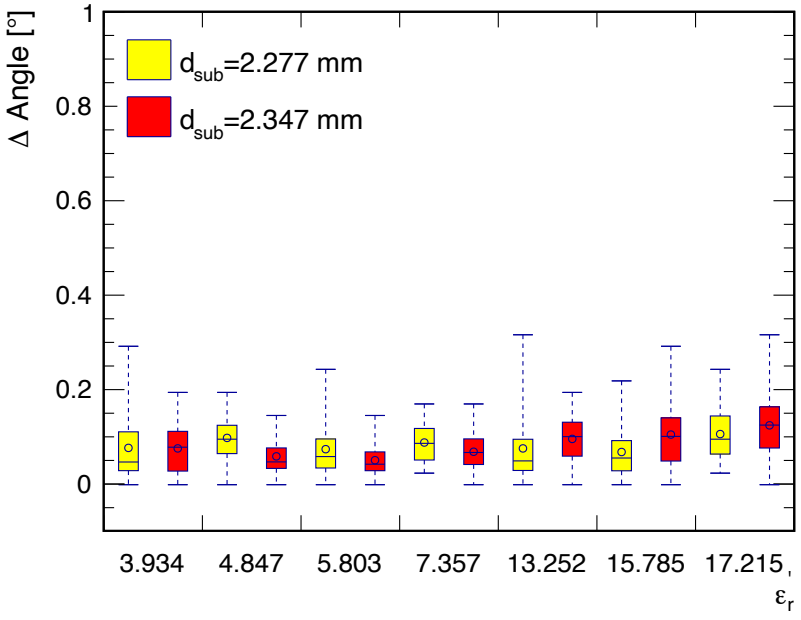

(b)

Figure 5.10: Angular deviations relative to the unpainted sample a) 2 cm distance and 0° tilting. b) 2 cm distance and 10° tilting.

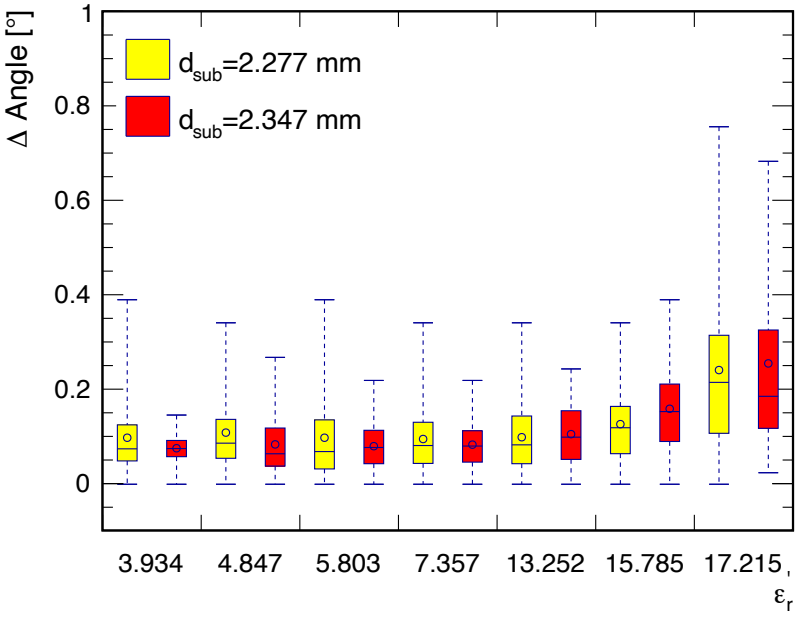

(a)

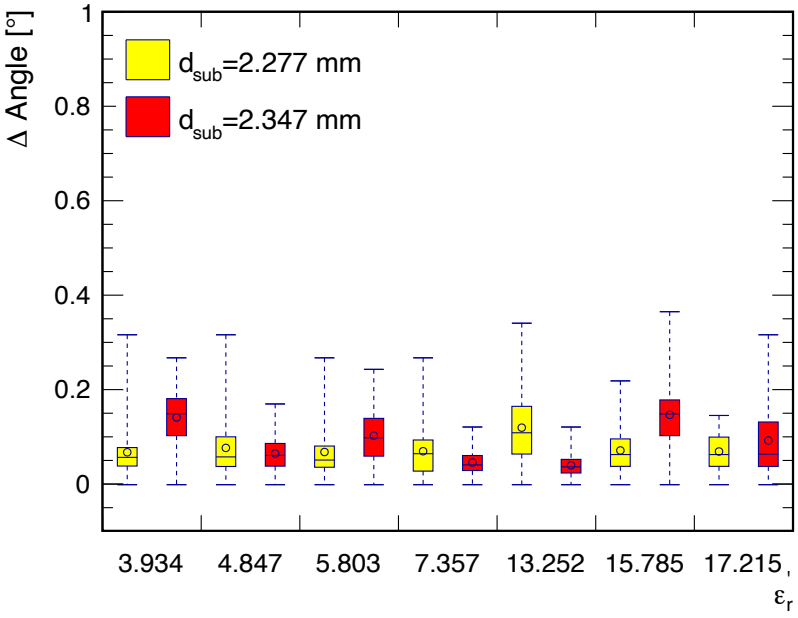

(b)

Figure 5.11: Angular deviations relative to the unpainted sample a) 5 cm distance and 0° tilting. b) 5 cm distance and 10° tilting.

5.1.5 Error in Object Separation

For examining the error in object separation caused by the different basecoats, a similar measurement setup is used as for the evaluation of the angular deviation. Since at least two targets are needed to evaluate the object separability of the radar sensor influenced by coatings, the target simulator is replaced with two corner reflectors. Since the object separation is evaluated by a binary statement, less precision is needed than for determining the angular deviation. As a result, using the corner reflectors is sufficient enough for this evaluation. The corner reflectors are positioned after the absorber tunnel at approximately 1.5 m distance from the sensor. The two mirrors are mounted on a rail to change the distance between them. All measurements are performed with the radar being positioned boresight relative to the targets.

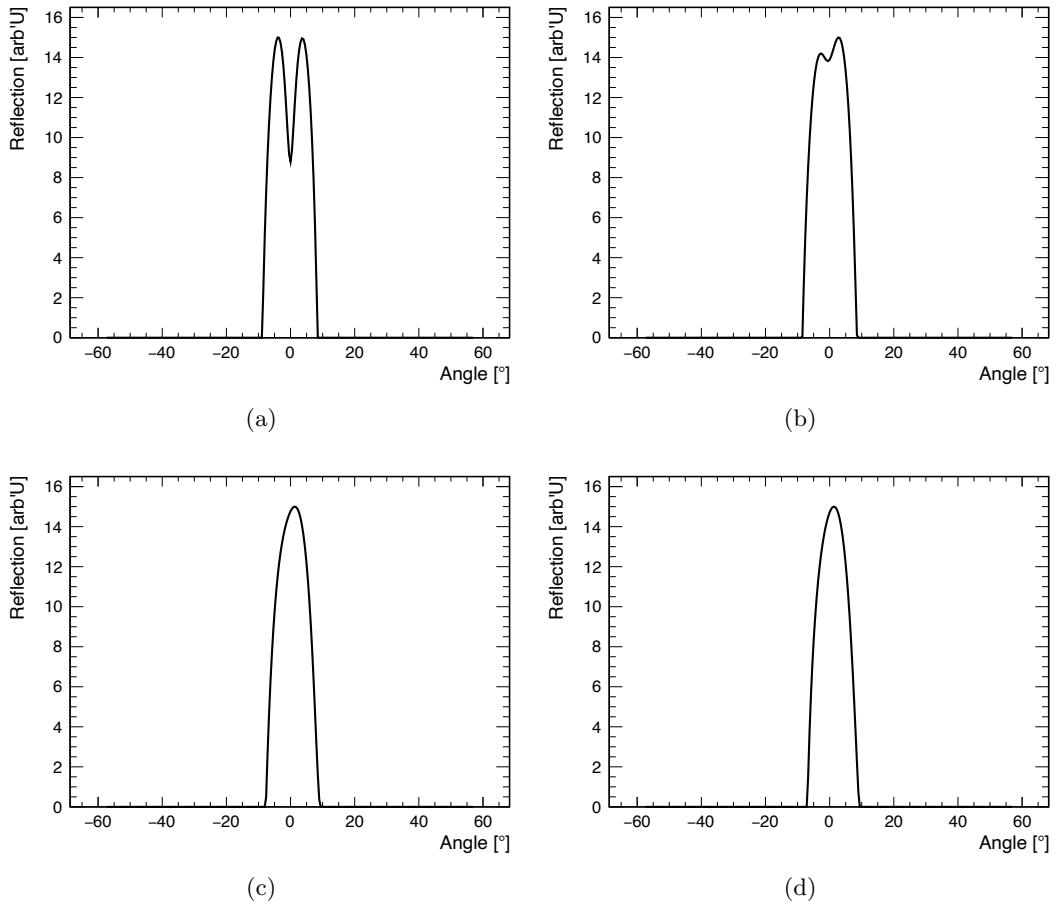

Figure 5.12: Angular projection of evaluated scenarios using two corner reflectors. The scenarios are: a) Clearly separable. b) Barely separable. c) and d) not separable.

First, the distance between the two mirrors is determined where the radar sensor can just barely separate the two objects. This is found at a spacing of 23 cm between the

mirrors. At 24 cm the two mirrors are clearly separated by the sensor, where for 22 cm and 21 cm they are only visible as one target. The angular projections of these scenarios can be seen in Fig. 5.12. These four distances will be investigated for all basecoats as well as the base substrate. Furthermore, the same spacing and tilting configurations are used as in the section about the angular deviation. The separability is evaluated using a peak finder, which compares the recognized peaks to the amount of peaks found for the measurement without a sample in front of the sensor.
The measurement showed that the separability of objects is not influenced by any configuration e.g. spacing between sensor and sample and tilting angle except for two samples. For the turquoise and silver basecoat, the sensor is not able to separate the two mirrors from each other for the distance where they are barely separable. In particular, the stated basecoats are problematic when applied to the thicker substrate at a distance of 5 cm between sensor and sample and 0° tilting angle. On the other hand, 2 cm and 0° showed no influence on the separability. The reason, why the stated basecoats applied on the thicker samples caused an error in the object separation is due to the fact that these basecoats show the highest permittivity and therefore the highest reflection. As shown before, the thicker substrate shows a higher reflection than the thinner one in general. As a result, the error in object separation is caused by the high reflections between the sample and the sensor as seen for the angular deviations. However, the fact that 2 cm and 5 cm spacing influences the separability at a 0° tilting angle can not be explained without further investigation. In general it is expected that a standing wave pattern between the sensor and the sample is present when tilting the sample 0° relative to the sensor. Depending on a maximum or minimum of the standing wave, the sensor sees less or more damping. This difference could be enough to result in an error in object separation depending on the spacing between the sensor and the sample. In terms of measurements performed in this section, the damping at 5 cm could be higher than at 2 cm, since one point lies within a minimum or maximum respectively.
In order to proof this statement, additional measurements as well as a simulation using CST is conducted. For the latter one, the simulation is performed in the time as well as the frequency domain to guarantee the independence of the results. First, measurements are performed using the same setup as before with slight changes. As a target one single corner reflector is used, since the target is just needed to reflect the signal back to the sensor. The amplitude of the reflection of the target is measured for different distances between sensor and the turquoise basecoat painted on the thicker substrate. In order to get a relatively high resolution measurement, a measurement is taken starting from 2 cm distance between sensor and sample every 1 mm until a distance of 5 cm is reached. The sample in front of the sensor is moved using an industrial robot enabling precise positioning. The resulting pattern can be seen in Fig. 5.14 (a). It can be clearly seen that two maxima are spaced nearly exactly 2 mm apart, which corresponds to half the wavelength of the radar sensor. It can be stated that the received signal amplitude depends on the spacing between the sensor and the sample and that certain spacings lead to a more favourable signal strength than others. Since the error in object separation is only present for samples with the highest permittivity, it is likely that the effect is mainly influenced by standing waves between sensor and sample. For the simulation, the sample

is modeled with substrate, basecoat and clearcoat and the corresponding thickness as well as utilizing the permittvity values of the materials, which are determined in Chapter 3 and 4. Since the main goal is to investigated if a distance between sensor and sample can have an influence on the amplitude of the signal at all, the simulation only considers the reflected waves of the backside of the sample not the signal coming from a corner reflector. For the simulation a step size of 0.5 mm is chosen, covering again a distance between sensor and sample from 2 cm to 5 cm. In order to recreate the same scenario as for the measurement, the electric field is evaluated monostatically, which corresponds to the red plane seen in Fig. 5.13.

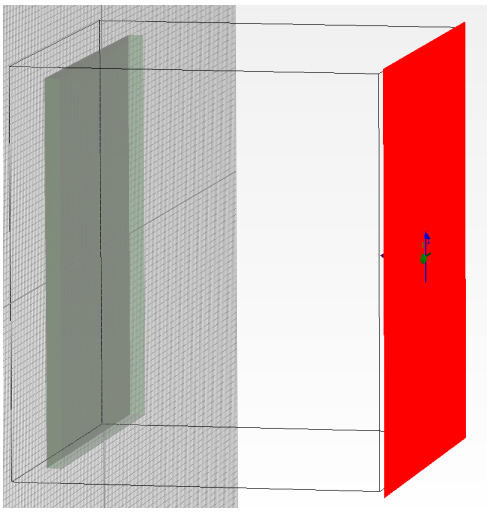

Figure 5.13: Setup for CST simulation. The modeled sample measures 6 cm on each side. The red surface shows the measurement point, where the amplitude of the electric field is evaluated. The distance between the red plane and the substrate is reduced by 0.5 mm every step.

The results of the simulation can be seen in Fig. 5.14 (b). Comparing the measurement with the simulation, a good agreement is found. Identical to the measurement, the simulation shows alternating minima and maxima every 1 mm, which corresponds to a quarter wavelength. It can also be seen that the overall pattern shown in the plot of the simulation and measurement are the same with the highest maximum located at approximately 37 mm distance. It should be mentioned that for the measurement the smallest distance is located at 2.1 cm, due to distance limitations caused by the robot. Moreover, a very slight shift can be observed when compared to the simulation, which is caused by an unavoidable mismatch between measured and actual distance. As mentioned before, on the simulation side two different solvers are tested to avoid results, which are dependent on a certain solver. However, both solver showed a very similar output, the simulation displayed in this section is performed in the time domain using the finite integration technique.

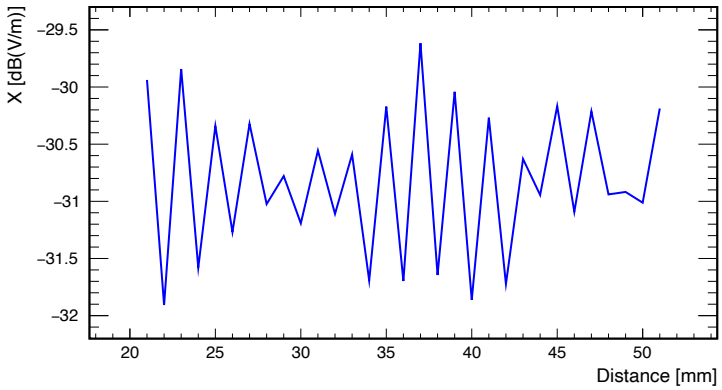

(a)

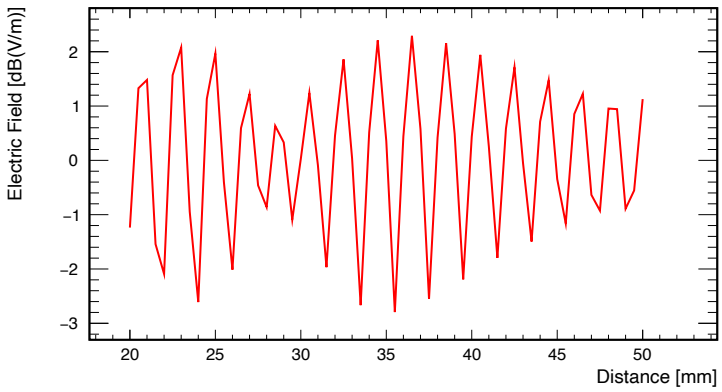

(b)

Figure 5.14: a) Measured amplitude of signal b) Simulated amplitude of signal. The measured as well as the simulated data show a standing waves pattern between the sensor/source and the sample.

The fact that the simulation and the measurement are that similar, although for the measurement the amplitude of the reflected signal of the corner reflector is used, shows that the error in object separation is caused by standing waves between the sensor and the sample. Furthermore, this also explains that only samples with the highest reflectivity tilted 0° relatively to the sensor caused a performance degradation. The additional simulation and measurement confirmed the assumption that the distance between sensor and sample can indeed impact the separation of objects. Depending on the spacing the received signal can be higher or lower, resulting in a strong damping, where both objects can not be separated anymore by the sensor. A more detailed simulated picture of the standing waves between sensor and sample can be seen in Fig. 5.15.

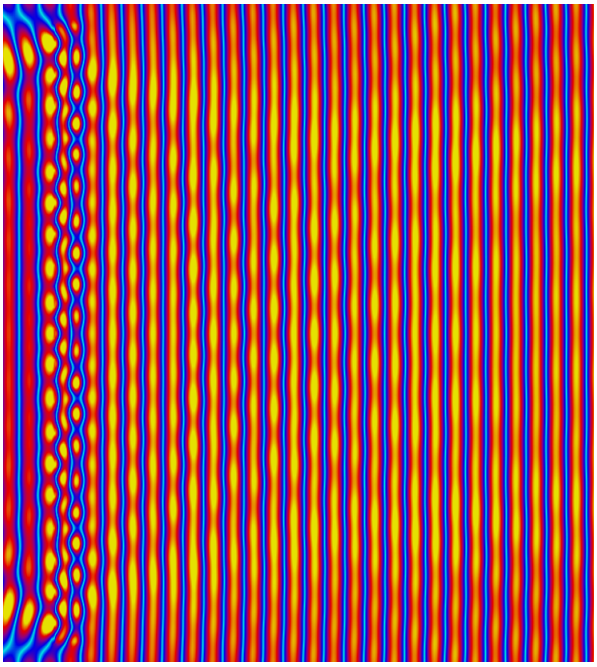

Figure 5.15: Simulated standing wave pattern between sensor and sample. The longitudinal side represents the distance between sensor and sample, similar to Fig. 5.13. The sample is placed in the left part of the picture, where diffraction effects are visible.

5.2 Impact on ADAS and AD Functions

In the second chapter, it is explained, how a radome or painted sample can influence the sensor. Especially the angular deviation caused by such scenarios is elaborated from a mere physical point of view. In this section, the impact of an angular deviation or an error in object separation on ADAS and AD functions such as brake assist or ACC is discussed. In order to evaluate maximum allowed deviation in estimating the AoA from function side, the following can be considered. A street with a width of 3.75 m, would result in a maximum tolerable angular deviation of $\approx 0.36°$ in a distance of 300 m, which is necessary for ACC and brake assist for high speeds. Exceeding this limit would lead to assigning a vehicle to a wrong lane which would have negative consequences, especially for a brake assist. Assuming a common deviation of 0.2° for current radar sensors, the additional deviation caused by the radome would have to be below 0.2°. How large the error can be strongly depends on the range of the sensor, as shown in Fig. 5.16. Assuming an error of approximately 0.2° allowed by a painted bumper or radome, strongly limits possible coatings. When looking at the results comparing the angular deviation relatively to a measurement without a sample in front of the sensor, displayed in Fig. 5.8 and Fig. 5.9, it can be seen that only the basecoat with the four lowest $\varepsilon_r^{'}$ values stay below the threshold when including the whole data range and tilting the sample 0°. When only considering the mean and the quartiles, a $\varepsilon_r^{'}$ up until

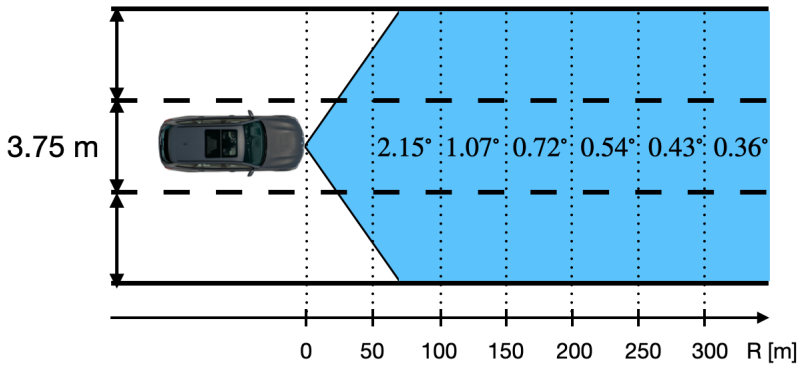

Figure 5.16: Maximum allowed angular deviation for a ACC function. The blue area shows the FoV within the street of a FRR sensor. A larger required distance decreases the threshold of the allowed deviation.

approximately 16 would be reasonable for the thin and up to 7 for the thick substrate. Unfortunately, even outliers exceeding the threshold can result in critical situations, where the sensor can not provide the necessary precision. The more interesting case, which also is closer to reality, is the tilted one. When comparing the same graphs as mentioned before for the 10° case, it can be seen that all coatings do not exceed the threshold of 0.2°, when comparing the quartiles. However, when looking again at the whole data range, it can be seen that some samples again exceed the 0.2°. Furthermore, this is completely independent of the ε_r' value. The 0.2° threshold is derived using a straight lane without a curvature. Since on a curved road as seen in Fig. 5.17, the 0.2° should not be exceeded, the estimated angles in the complete FoV have to stay below the threshold.

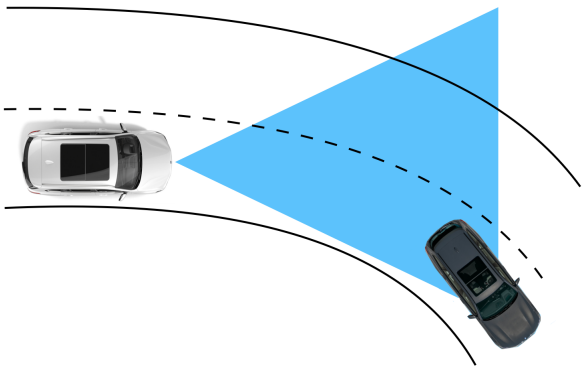

Figure 5.17: Schematic of FoV of sensor for a curved road. Due to the curvature, also the angular deviation for small or large angles is important.

Moreover, the guard rails are used for self-localization. The localization is done by evaluating the change of the radial velocity of objects in order to classify them as stationary, which requires the estimated angle as an input. Since the guard rails are located at the edge of the street, larger or smaller angles have to be determined as precise as angles at boresight.
An error in object separation, can have as negative consequences for ADAS and AD as an angular deviation. Especially for functions such as brake assist, the radar sensor needs to be able to separate two vehicles driving in front next to each other. Otherwise a brake assist would not be feasible based on radar sensors. In Section 5.1.5, it is shown that the ability of the radar sensor to separate objects can degrade depending on the sample and in particular the permittvity of the applied basecoat. It can be observed that basecoats with high permittivities applied to an unfavorable thickness of the substrate could render the sensor unable to separate two objects placed side by side from each other. This effects is also only seen for a certain spacing between sensor and sample. As a result, the effect can occur only in rather rare circumstances. Nevertheless, it can be simply avoided according to the measurements, by choosing the proper thickness of the substrate to reduce the reflectivity. In addition, this effect is only observed when not tilting the sample and is not seen for a 10° tilting. If a tilted bumper surface or radome is a considerable possibility from a design perspective, this is therefore strongly recommended.

CHAPTER 6

Influence of Titanium Dioxide on Radar Sensors

As shown in Chapter 4, basecoats consist of a complex mixture of different elements. For most of the effect coatings, aluminum is a crucial part of the coating. Therefore, its concentration and the consequences for radar transparency have also been of interest in the past [7] [49]. Besides alumium, TiO_2 is present in almost all colors. As mentioned before, TiO_2 has a high optical refractive index [86] [87], which makes coating appear colorful and vibrant. Since this pigment is very widespread, a dedicated investigation similar to aluminum is neccessary. Therefore, in this chapter different TiO_2 concentrations are investigated, including the influence on the real part of the relative permittivity as well as the influence on angle estimations and object separation. The permittivity determination uses the method described in Chapter 3. The latter two examinations are similar to the ones performed in Chapter 5. The results of this chapter are found in a more condensed form in [88]. In total three different weight percentage concentration are investigated, being 20 %, 40 % and 60 %. Higher concentrations could not be investigated due to the saturation of the used base material. The goal of this chapter is to understand for which concentration problems for radar arise. This enables choosing a limit for TiO_2, which combined with former investigations such as aluminum concentrations can provide knowledge for creating radar transparent coatings.

6.1 Influence on Permittivity

For the determination of $\varepsilon_r^{'}$, each concentration is applied to the PC plates used for all permittivity related investigations within this thesis. The thickness of the coating, which is needed for the model used to extract $\varepsilon_r^{'}$ and $\tan\delta$, is determined using the eddy current method described in Section 3.2.1. Unlike the samples with basecoat before, the TiO_2 samples only consist of two layers, the PC substrate and the TiO_2 coating. All samples are painted with a thickness of 25 µm. Although the permittivity is independent of the

thickness, a similar thickness reduces the risk of falsified results caused by numerical artifacts. Since the behavior of the permittivity with increasing concentration is of interest, a higher sample size is necessary to ensure a statistical significance. Therefore, for each concentration two samples are produced. All samples are painted using an electrostatic rotary-bell application, in particular the ESTA 1 application. Since two samples exist, 12 measurement points are taken using the VNA method and 2 for each concentration using the RMS. The results can be seen in Table 6.1.

Device	$\varepsilon_r^{'}(20\ \%)$	$\varepsilon_r^{'}(40\ \%)$	$\varepsilon_r^{'}(60\ \%)$
VNA	3.521 ± 0.251	5.126 ± 0.201	7.238 ± 0.212
RMS	3.355 ± 0.371	5.342 ± 0.410	7.051 ± 0.391

Table 6.1: Real part of relative permittivity for different TiO_2 concentrations evaluated with VNA and RMS setup.

It can be observed that $\varepsilon_r^{'}$ increases with increasing TiO_2 concentration, which holds true for the VNA as well as the RMS data. This is expected, since the higher concentration also makes the sample appear more white, which is caused by the high refractive index of TiO_2. Furthermore, the increasing refractive index of the material results in a higher permittivity as shown in Section 2.4. The data shows a good agreement between the VNA and RMS, although the RMS uses less data. The loss tangent $\tan\delta$ shows no significant change with increasing concentration but a relatively high value when compared to the basecoats investigated in this thesis. For the VNA and RMS, the loss tangent is found to be approximately $\tan\delta = 0.09 \pm 0.004$. It can also be seen that the real part of the relative permittivity scales linearly with increasing TiO_2 concentration. It should be noted that this is valid for the investigated range of concentration between 20 % and 60 % and might change for higher concentrations. However, such high concentrations are not used for automotive coatings and therefore the statement holds true for the purpose of creating radar transparent coatings. It should be also noted that TiO_2 shows a high dispersion as shown in [89]. As a result, the presented results are only valid for the frequency range of the VNA, which reaches from 60 GHz to 90 GHz. Since this thesis is dedicated to radar sensors operating between 76 - 77 GHz, all results in this section apply. The linearity and the results are represented graphically in Fig. 6.1. The fit represented by the red line is applied to the VNA data, to demonstrate the linear behavior within the error bars, which are a result of uncertainties caused by the thickness measurements as explained in Section 3.2. Comparing the results to similar measurements utilizing aluminum filled epoxy resins [7] it can be seen that a linear increasing permittivity with increasing the concentration is not obvious. In particular, in [7] it is shown that the permittivity scales exponentially with increasing aluminium concentration. This was also shown for automotive basecoats in [49]. However, in the latter one a slight deviation was observed due to the fact that automotive coatings consist of a complex mixture of various elements. Of course the main difference between aluminum and TiO_2 is given by

the fact that aluminum is conductive, where TiO_2 is a semi conductor [90]. Therefore, the physical mechanism behind the increasing permittivity with concentration is different for aluminum than TiO_2. In the aluminum case, a variety of complex models exist to estimate the permittvity as a mixture of metal and dielectric materials which can be found in e.g. [91] [92] [93]. All these models are based on a similar electrostatic approach, which is trying to calculate the polarization of small particles such as the aluminum particles found in coatings [7]. For TiO_2 on the other hand, the linear behavior shows that it behaves like a dielectric. Estimating the permittivity for a given concentration is therefore much less complex, which also is beneficial for creating automotive coatings with radar transparency in mind.

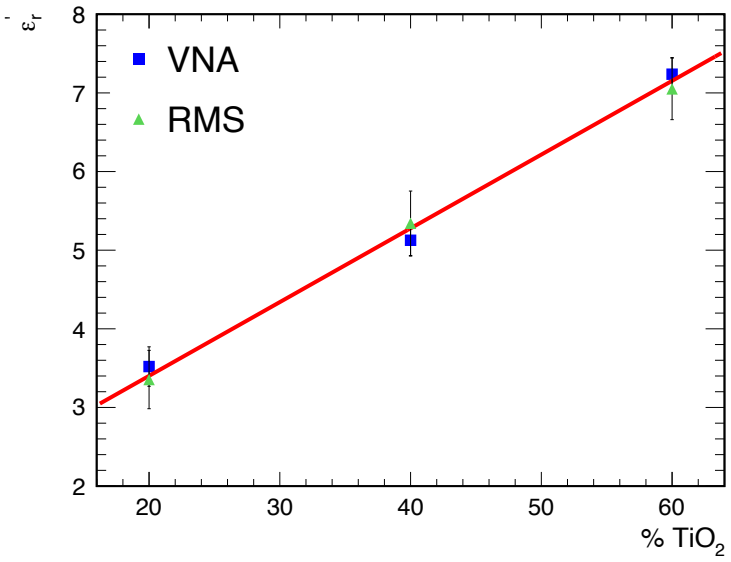

Figure 6.1: Change of real part of relative permittivity with TiO_2 concentration for VNA and RMS data. The red line represents a linear fit applied to the VNA data.

6.2 Influence on Sensor Performance

Similar to Section 5.1.4 and 5.1.5, the same measurements are repeated in this section. The same TiO_2 coatings are used as in the previous section but applied to the ABS substrate, which is used for all sensor related investigation in the last chapter. Again, two thicknesses are used to to avoid effects only caused by not intended resonances. In total six samples are investigated, two for each concentration. First, the results regarding an angular deviation caused by TiO_2 are discussed. The same four measurement configurations are used as before being 2 cm and 5 cm spacing between sensor and sample and 0° and 10° tilting angle respectively. In this section only the results are discussed for 2 cm and 0° tilting angle since this represents the worst case. As seen in Section 5.1.4, a tilting angle of 10° decreases the angular deviation drastically. As a result, no signifi-

cant influence of TiO_2 is observed when tilting the sample. Also no significant difference between 2 cm and 5 cm can be seen. The graph for 2 cm and 0° for the thin and thick substrate can be found in Fig. 6.2. For the thin substrate, which is displayed on the left column, it can be seen that similar to the basecoats investigated before, the coating has a compensating effect. As a result, the angular deviation caused by the bare substrate (black line) is higher than the deviation of the painted sample (blue line). Furthermore, the deviation of the painted sample relatively to the bare substrate (red line) shows almost no influence of the changing concentration at all. As mentioned before, in theory thickening the sample with a coating can achieve a more resonant sample. This effect is also influenced by the permittivity of the coating. As a result, a certain combinations of thickness and permittivity can make a sample more resonant than others. This can be observed for the 60 % concentration on the thin substrate, where the higher concentration shows a smaller angular deviation than the lowest concentration. The thick substrate shows a different, more expected behavior. Comparing the deviation caused by the painted sample relative to a measurement without a sample in front of the sensor (blue line) shows that the deviation clearly increases with increasing TiO_2 concentration. This is caused by the higher reflection due to higher permittvity. In contrast to the thin substrate, it can also be seen that the red and blue line almost match. This means that the main influence of the angular deviation is caused by the coating not the substrate itself. This is also supported by the fact that the thicker substrate shows a resonant behavior when no coating is applied. As stated before, in order to assign a vehicle in front of the car to the right lane, a maximum angular deviation of approximately 0.4° would be allowed. Assuming the deviation of the sensor being 0.2°, would only allow for additional 0.2°. Applying the 0.2° angular deviation to the graph in Fig. 6.2, shows that this threshold is already exceeded by the bare substrate. Moreover, the painted sample also shows higher deviations for rather large angles independent of the concentration itself. For the thicker substrate on the other hand, a much clearer statement can be given. The angular deviation shows an uncritical behavior for 20 % and 40 % only exceeding the threshold for a 60 % concentration. For the 60 % TiO_2 concentration, a higher angular deviation than 0.2° can be observed for angles smaller than −5° and greater than 10°. Although this is uncritical for a straight lane, it can be problematic for roads with a certain curvature or for the self-localization of the car. Regarding an error in object separation, no influence of TiO_2 is observed. This is expected due to the relatively low permittivity. For basecoats, TiO_2 can be critical for the radar sensor performance for extremely high concentrations such as 60 %. This strongly depends on the thickness of the coating as well as the substrate itself. For the thinner substrate a compensating effect of the coating is observed even reducing the angular deviation of the bare substrate in some cases. Compared to aluminum, however, TiO_2 can be classified as an uncritical part of automotive basecoats for radar applications.

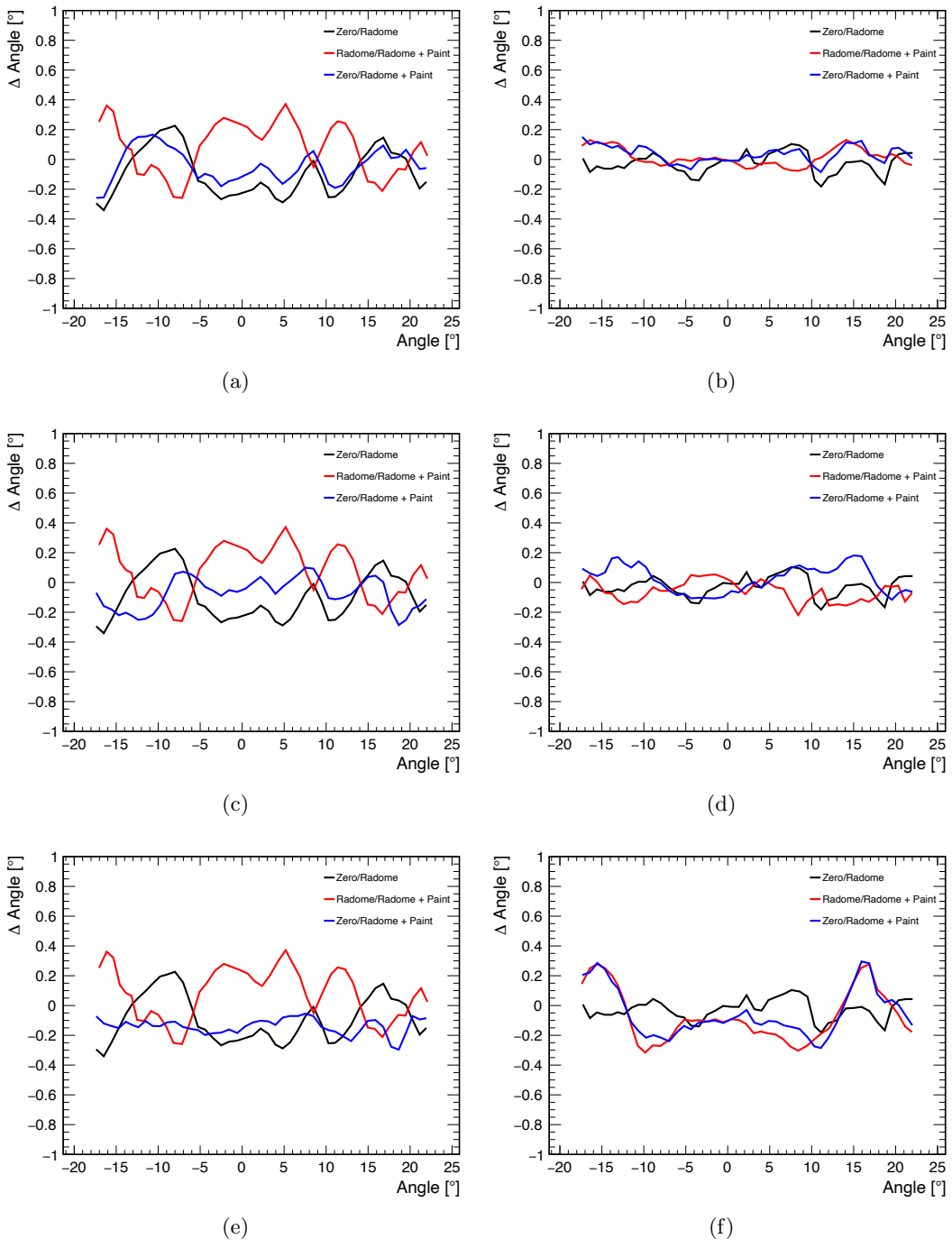

Figure 6.2: Angular deviation for 20 %, 40 % and 60 % concentration applied on the thin and thick substrate. a) 20 % concentration applied to the thin substrate. b) 20 % concentration applied to the thick substrate. c) 40 % concentration applied to the thin substrate. d) 40 % concentration applied to the thick substrate. e) 60 % concentration applied to the thin substrate. f) 60 % concentration applied to the thick substrate.

CHAPTER 7

Conclusion

In this thesis, unknown effects caused by automotive coatings on radar sensors operating between 76 - 77 GHz were investigated. Furthermore, expected effects are experimentally quantified. As a descriptive quantity, the permittivity was used to compare the radar transparency of different coatings. In order to determine the real part of the relative permittivity and the loss tangent precisely, a dedicated method utilizing the transmission line model was developed. This method enables determining the dielectric properties of multilayered samples. To reduce numerical ambiguities and therefore increase the accuracy of the results, specially designed Polycarbonate plates were used. In addition, alignment tools were developed to reduce uncertainties originating from thickness measurements. The validation with literature values showed that the method provides accurate results for single as well as multilayer samples. Using the permittivity, the dielectric inhomogeneities of Polypropylene and Polycarbonate were investigated. The results show that Polycarbonate is a superior material from a dielectric point of view.
Depending on the application technique of coatings, the radar transparency varies. This was investigated by applying the same basecoat with pneumatic and electrostatic applications, where for the latter one, two different charge processes were used. For the first electrostatic application, the coating are charged directly in contrast to the second method, where an external field is used to apply the charge in an indirect way. It was observed that the real part of the relative permittivity changes depending on the application technique. The pneumatic application showed the lowest, the indirectly charged electrostatic method the highest real part of the relative permittivity. For coatings without effect pigments, this effect can be explained by the fact that the pneumatic application uses the highest pressure resulting in an overall more condensed application of the coating. For basecoats with effect pigments such as aluminum particles, the main reason for a lower real part of the relative permittivity is due to the rotation of the bell cup. The content of the basecoats were analyzed using a scanning electron microscope

in conjunction with EDX-spectra. Using this analysis the root cause of the high permittivites of certain basecoats was determined. The high rotation speeds result in bigger particles being pushed outwards in radial direction and therefore into the overspray. As a result, in the case for e.g. silver basecoats with a high aluminum content, the effective aluminum concentration decreases and therefore the permittivity decreases as well. Although the difference in application technique is barely visible with the bare eye, it clearly can be seen in the micrographs. It was also observed that the improvement in permittivity scales with the amount of aluminum and mica flakes. For basecoats with high permittivity, an electrostatic application can noticeably improve the radar transparency and is therefore recommended.
To investigate possible consequences for advanced driver assistance systems and autonomous driving, measurements with an experimental radar were conducted. The goal of the measurement was to understand the impact of the permittivity of basecoats on angle estimations and errors in object separations. Therefore, the same basecoats as investigated in Chapter 4 were applied to acrylonitrile butadiene styrene substrates and mounted in front of the sensor. For each basecoat, two substrates were used differing in thickness. The different thicknesses resulted in different resonances. The thicker substrate showed a resonance between 76 - 77 GHz unlike the thinner one. However, after applying the coatings, the thinner substrate became resonant for certain basecoats. Moreover, the influence of the tilting angle and the spacing between the sensor and the sample were investigated. Two tilting angles of 0° and 10° were investigated, as well as spacings of 2 cm and 5 cm between sensor and sample. It was observed that a 0° tilting showed higher deviations in angle estimations than 10°. The main cause are standing waves between the sensor and the sample interfering with the actual signal reflecting back from the target. Furthermore, basecoats with higher permittivity showed a higher angular deviation, caused by the higher reflectivity. This effect can be drastically reduced by tilting the cover. For the maximum allowed angular deviation caused by a radome or painted sample, a value of 0.2° was derived. The value is based on requirements of advanced driver assistance systems such as brake assist. Not tilting the sample resulted in only basecoats with very low permittivity staying below the threshold. Tilting the sample 10°, resulted in a nearly permittivity independent behavior. Except a few outliers, all basecoats stayed below the thresholds. In general, no difference was observed between the two thicknesses of the substrates neither the spacing between sensor and sample. In addition to an angular deviation, also changes caused by basecoats in the object separation capability of the sensor were investigated. The same tilting angles and spacings were used as before. As a target, two corner reflector were used, which were positioned with four different distances from each other. For two spacings, the sensor could clearly separate the two targets, for the other two the sensor was barely and not able to separate the objects respectively. It was observed that only for the two basecoats with the highest permittivity and tilted 0°, the sensor was not able to separate the two targets anymore. This was only observed for the basecoats applied to the thicker substrate and with 5 cm spacing between sensor and sample. The root cause for this effect is given by standing waves. Depending on the distance, the sensor is exposed to more or less damping, which can result in an error in object separation. This conclusion was

also supported by a CST simulation utilizing two different solvers.
For the last part, the influence of TiO_2 on radar sensors was investigated. Therefore, a concentration of 20 %, 40 % and 60% was applied to polycarbonate plates and the acrylonitrile butadiene styrene substrate. It was observed that the real part of the relative permittivity scales linearly with increasing concentration within the investigated concentrations, for frequencies between 60 - 90 GHz. For aluminum on the other hand, an exponential behavior was observed in the past. In addition to determining the permittivity, also angular deviations and the influence on object separation was investigated. For the angular deviation only a critical behavior could be seen for a 60 % concentration applied to the thicker substrate. Furthermore, the threshold of 0.2° was exceeded for relatively large or small angles, which are relevant for curved roads and the self localization of the car. An influence on the capability of separating objects was not observed. In conclusion, TiO_2 is an uncritical part of automotive basecoats when compared to aluminum, since 60 % concentrations are not used.
With the investigations conducted in this thesis, the industry is one step closer to understand the complex topic of creating radar transparent paints. Scientifically unknown topics such as the influence of paint techniques were quantified. Effects such as angular deviations and errors in object separation were experimentally quantified and showed that even basecoats with relatively low permittivity can be problematic. In order to enable a hidden integration behind painted plastic parts such as bumpers, the surface has to be tilted to lower negative effects on the sensor performance. Furthermore, it is clearly shown that although more complicated to manufacture, the surface penetrated by the radar sensor has to be thickness optimized to lower the reflectivity. Since the right thickness strongly depends on the permittivity of the applied coating, different thicknesses have to be used for different basecoats. Otherwise, a hidden integration for high performance radar sensors necessary for future advanced driver assistance systems and autonomous driving functions is not possible.

Bibliography

[1] Marco Galvani. "History and future of driver assistance". In: *IEEE Instrumentation Measurement Magazine* 22.1 (2019), pp. 11–16. DOI: 10.1109/MIM.2019.8633345.

[2] H. Meinel and Juergen Dickmann. "Automotive Radar: From Its Origin to Future Directions". In: *Microwave Journal* vol.56 (Sept. 2013), pp. 24–40.

[3] SAE. *Taxonomy and Definitions for Terms Related to On-Road Motor Vehicle Automated Driving Systems*. 2014.

[4] Jonah Gamba. "Radar Signal Processing for Autonomous Driving". In: 1st ed. Signals and Communication Technology. Springer, Singapore, 2020. Chap. 1, pp. 11–12.

[5] John E. Mahan. *Physical Vapor Deposition of Thin Films*. 2000.

[6] Florian Pfeiffer. "Analyse und Optimierung von Radomen für automobile Radarsensoren". Dissertation. München: Technische Universität München, 2009.

[7] Frerk Fitzek. "Integrierte 79 GHz Breitbandradarsensoren für Fahrerassistenzfunktionen der Zukunft". Dissertation. München: Technische Universität München, 2012.

[8] *Introduction to Radar Systems*. 3rd ed. Electrical engineering series. Mc-Graw-Hill, 2001.

[9] Sujeet Milind Patole et al. "Automotive radars: A review of signal processing techniques". In: *IEEE Signal Processing Magazine* 34.2 (2017), pp. 22–35. DOI: 10.1109/MSP.2016.2628914.

[10] B. K. Sarkar, C. J. Reddy, and R. Chandrakanth. "Considerations to increase the isolation between two antennas kept side by side". In: *1988 Symposium on Antenna Technology and Applied Electromagnetics*. 1988, pp. 1–3.

[11] Mark A. Richards. *Fundamentals of Radar Signal Processing*. 2nd ed. McGraw-Hill Education, 2014. Chap. 4, pp. 191–193.

[12] J. R. Klauder et al. “The theory and design of chirp radars”. In: *The Bell System Technical Journal* 39.4 (1960), pp. 745–808. DOI: 10.1002/j.1538-7305.1960.tb03942.x.

[13] C.E. Shannon. “Communication in the Presence of Noise”. In: *Proceedings of the IRE* 37.1 (1949), pp. 10–21. DOI: 10.1109/JRPROC.1949.232969.

[14] R. G. Lyons, ed. *Understanding Digital Signal Processing*. 3rd ed. Pearson Education, 2010.

[15] J.A. Cadzow. “Multiple source location: The signal subspace approach”. In: *Twenty-Third Asilomar Conference on Signals, Systems and Computers, 1989.* Vol. 2. 1989, pp. 777–781. DOI: 10.1109/ACSSC.1989.1201004.

[16] S. Silver and Institution of Electrical Engineers. *Microwave Antenna Theory and Design*. IEE electromagnetic waves series. P. Peregrinus, 1984. ISBN: 9780863410178. URL: https://books.google.de/books?id=Aex6dlKreHEC.

[17] R. Schmidt. “Multiple emitter location and signal parameter estimation”. In: *IEEE Transactions on Antennas and Propagation* 34.3 (1986), pp. 276–280. DOI: 10.1109/TAP.1986.1143830.

[18] R. Roy and T. Kailath. “ESPRIT-estimation of signal parameters via rotational invariance techniques”. In: *IEEE Transactions on Acoustics, Speech, and Signal Processing* 37.7 (1989), pp. 984–995. DOI: 10.1109/29.32276.

[19] Zahid Oscar Go’mez Urrutia. “MIMO Radar with Colocated Antennas: Theoretical Investigation, Simulations and Development of an Experimental Platform”. PhD thesis. University of Paris-Est, 2014.

[20] Jian Li and Petre Stoica. “MIMO Radar with Colocated Antennas”. In: *IEEE Signal Processing Magazine* 24.5 (2007), pp. 106–114. DOI: 10.1109/MSP.2007.904812.

[21] I. Bekkerman and J. Tabrikian. “Target Detection and Localization Using MIMO Radars and Sonars”. In: *IEEE Transactions on Signal Processing* 54.10 (2006), pp. 3873–3883. DOI: 10.1109/TSP.2006.879267.

[22] Jan Mietzner et al. “Compact 3D MIMO radar — Antenna array design and experimental results”. In: *2017 European Radar Conference (EURAD)*. 2017, pp. 130–133. DOI: 10.23919/EURAD.2017.8249164.

[23] Alexander M. Haimovich, Rick S. Blum, and Leonard J. Cimini. “MIMO Radar with Widely Separated Antennas”. In: *IEEE Signal Processing Magazine* 25.1 (2008), pp. 116–129. DOI: 10.1109/MSP.2008.4408448.

[24] Frerk Fitzek, Ralph H. Rasshofer, and Erwin M. Biebl. “Metamaterial matching of high-permittivity coatings for 79 GHz radar sensors”. In: *The 40th European Microwave Conference*. 2010, pp. 1401–1404. DOI: 10.23919/EUMC.2010.5616577.

[25] Eugene Hecht. *Optik*. 7th ed. De Gruyter Studium. De Gruyter, 2018.

[26] Wolfgang Demtröder. *Elektrizität und Optik*. 7th ed. Experimentalphysik 2. Springer, 2017.

[27] Max Born. *Optik - Ein Lehrbuch der elektromagnetischen Lichttheorie*. 2nd ed. Springer, 1932.

[28] Gerhard Friedsam. "Bestimmung der komplexen Permittivität und Permeabilität im Millimeterwellenbereich". PhD thesis. Technische Universität München, 1999.

[29] Christian Winter et al. "Permittivity Determination Method for Multilayer Automotive Coatings for Radar Applications at 77 GHz". In: *IEEE Transactions on Microwave Theory and Techniques* 70.4 (2022), pp. 2380–2388. DOI: 10.1109/TMTT.2022.3147479.

[30] Ufuk Malayoglu and Nurgun Besun. "Development of Nanosized Mica Particles from Natural Mica by Sonication/Organic Intercalation Method for Pearlescent Pigment". In: *Minerals* 10 (June 2020), p. 572. DOI: 10.3390/min10060572.

[31] Maryam Zori. "Particle size and kind of mica in synthesis of nontoxic bronze and gold pearlescent pigments based on nanoencapsulated hematite". In: *Journal of Ultrafine Grained and Nanostructured Materials* 48 (Dec. 2015). DOI: 10.7508/jufgnsm.2015.02.005.

[32] 2022. URL: https://www.merckgroup.com/en/brands/pm/xirallic.html.

[33] Ulrich Poth. *Automotive Coatings Formulation*. Vincentz Network, 2008.

[34] N. Gagnon et al. "Material characterization using a quasi-optical measurement system". In: *IEEE Transactions on Instrumentation and Measurement* 52.2 (2003), pp. 333–336. DOI: 10.1109/TIM.2003.810042.

[35] D.K. Ghodgaonkar, V.V. Varadan, and V.K. Varadan. "A free-space method for measurement of dielectric constants and loss tangents at microwave frequencies". In: *IEEE Transactions on Instrumentation and Measurement* 38.3 (1989), pp. 789–793. DOI: 10.1109/19.32194.

[36] Toshihide Tosaka et al. "Development of Complex Relative Permittivity Measurement System Based on Free-Space in 220–330-GHz Range". In: *IEEE Transactions on Terahertz Science and Technology* 5.1 (2015), pp. 102–109. DOI: 10.1109/TTHZ.2014.2362013.

[37] J. Baker-Jarvis, E.J. Vanzura, and W.A. Kissick. "Improved technique for determining complex permittivity with the transmission/reflection method". In: *IEEE Transactions on Microwave Theory and Techniques* 38.8 (1990), pp. 1096–1103. DOI: 10.1109/22.57336.

[38] Yi Wang et al. "Characterization of Dielectric Materials at WR-15 Band (50–75 GHz) Using VNA-Based Technique". In: *IEEE Transactions on Instrumentation and Measurement* 69.7 (2020), pp. 4930–4939. DOI: 10.1109/TIM.2019.2954010.

[39] Osamu Hashimoto et al. "Measurement of complex permittivity of radome material at 60 GHz frequency band". In: *Electronics and Communications in Japan (Part I: Communications)* 82.12 (1999), pp. 70–76.

[40] Z. Abbas, R.D. Pollard, and R.W. Kelsall. "Determination of the dielectric constant of materials from effective refractive index measurements". In: *IEEE Transactions on Instrumentation and Measurement* 47.1 (1998), pp. 148–152. DOI: 10.1109/19.728808.

[41] Martin S. Hilario et al. "W-Band Complex Permittivity Measurements at High Temperature Using Free-Space Methods". In: *IEEE Transactions on Components, Packaging and Manufacturing Technology* 9.6 (2019), pp. 1011–1019. DOI: 10.1109/TCPMT.2019.2912837.

[42] Yevhen Yashchyshyn et al. "W-Band Sensor for Complex Permittivity Measurements of Rod Shaped Samples". In: *IEEE Access* 9 (2021), pp. 111125–111131. DOI: 10.1109/ACCESS.2021.3103243.

[43] Yi-Ting Lin et al. "Extraction of Complex Permittivity of Dielectrics on Package from W-band to D-band". In: *2021 IEEE 71st Electronic Components and Technology Conference (ECTC)*. 2021, pp. 564–569. DOI: 10.1109/ECTC32696.2021.00100.

[44] M.E. Baginski, D.L. Faircloth, and M.D. Deshpande. "Comparison of two optimization techniques for the estimation of complex permittivities of multilayered structures using waveguide measurements". In: *IEEE Transactions on Microwave Theory and Techniques* 53.10 (2005), pp. 3251–3259. DOI: 10.1109/TMTT.2005.855133.

[45] Andreas Kilian, Jochen Weinzierl, and Lorenz-Peter Schmidt. "Permittivity Measurement Techniques at 24 GHz for Automotive Polymer Composites Including Thin Films and Paint Foils". In: *German Microwave Conference*. 2008, pp. 1–4.

[46] Clifford Schoff. "Surface defects: Diagnosis and cure". In: *Journal of Coatings Technology - J COATING TECHNOL* 71 (Jan. 1999), pp. 56–73. DOI: 10.1007/BF02697888.

[47] Fischer Technology Inc. Apr. 2022. URL: https://www.helmut-fischer.com/de/methoden/amplitudensensitives-wirbelstrom-verfahren.

[48] G.L. Friedsam and E.M. Biebl. "Precision free-space measurements of complex permittivity of polymers in the W-band". In: *1997 IEEE MTT-S International Microwave Symposium Digest*. Vol. 3. 1997, 1351–1354 vol.3. DOI: 10.1109/MWSYM.1997.596579.

[49] Florian Pfeiffer and Erwin M. Biebl. "Inductive Compensation of High-Permittivity Coatings on Automobile Long-Range Radar Radomes". In: *IEEE Transactions on Microwave Theory and Techniques* 57.11 (2009), pp. 2627–2632. DOI: 10.1109/TMTT.2009.2031931.

[50] Frerk Fitzek and Ralph H. Rasshofer. "Automotive Radome Design - Reflection Reduction of Stratified Media". In: *IEEE Antennas and Wireless Propagation Letters* 8 (2009), pp. 1076–1079. DOI: 10.1109/LAWP.2009.2032571.

[51] S. Kästner and K. Altenburg. “Wellenausbreitung in Geschichteten Medien bei Senkrechtem Einfall und die Anwendung auf Leitungstheorie, Elektrische Wellen, Optik, Akustik, Wellenmechanik Sowie Mechanische und Elektrische Vierpolketten”. In: vol. 448. 1953, pp. 29–31.

[52] Peter Russer. *Electromagnetics, Microwave Circuit, and Antenna Design for Communications Engineering*. Artech House, 2003.

[53] F. James. *MINUIT function minimization and error analysis: Reference manual version 94.1*. Tech. rep. Geneva, Switzerland: CERN, 1998.

[54] Alfio Lazzaro and Lorenzo Moneta. “MINUIT package parallelization and applications using the RooFit package”. In: *Journal of Physics: Conference Series* 219.4 (2010), p. 042044. DOI: 10.1088/1742-6596/219/4/042044. URL: https://doi.org/10.1088/1742-6596/219/4/042044.

[55] Won Sang Cho et al. “OPTIMASS: a package for the minimization of kinematic mass functions with constraints”. In: *Journal of High Energy Physics* 1 (2016). DOI: 10.1007/jhep01(2016)026. URL: https://doi.org/10.1007%2Fjhep01%282016%29026.

[56] W. C. Davidon. *Variable metric method for minimization*. Tech. rep. Atgonne National Laboratory, 1959.

[57] Rogers Corporation. *RT/duroid 5870 - 5880 Data Sheet*.

[58] Rogers Corporation. *RO3000 Laminate Data Sheet RO3003 - RO3006 - RO3010 - RO3035*.

[59] Hisham Maddah. “Polypropylene as a Promising Plastic: A Review”. In: *2163-1352* 2016 (Jan. 2016), pp. 1–11. DOI: 10.5923/j.ajps.20160601.01.

[60] Olagoke Olabisi and Kolapo Adewale. *Handbook of Thermoplastics*. CRC Press, Dec. 2015. ISBN: 9781466577220.

[61] Muhammad Harris et al. “Acrylonitrile Butadiene Styrene and Polypropylene Blend with Enhanced Thermal and Mechanical Properties for Fused Filament Fabrication”. In: *Materials* 12 (Dec. 2019), p. 4167. DOI: 10.3390/ma12244167.

[62] M. Pieraccini et al. “Joint time-frequency analysis for investigation of layered masonry structures using penetrating radar”. In: *IEEE Transactions on Geoscience and Remote Sensing* 42.2 (2004), pp. 309–317. DOI: 10.1109/TGRS.2003.817801.

[63] Maximilian Korff. “Analysis of Differences in Radar Transparency of Water- and Solventborne Basecoats”. MA thesis. Universität Augsburg, 2021.

[64] D. Stoye and W. Freitag. *Paints, Coatings and Solvents*. 2nd ed. Wiley, 1998. ISBN: 9783527288632.

[65] Bodo Müller and Ulrich Poth. *Coatings Formulation: An International Textbook*. Vincentz Network SN - 9783748600268, 2017. DOI: doi:10.1515/9783748600268. URL: https://doi.org/10.1515/9783748600268.

[66] Mayur V. Andulkar, Shital S. Chiddarwar, and Akshay S. Marathe. "Novel integrated offline trajectory generation approach for robot assisted spray painting operation". In: *Journal of Manufacturing Systems* 37 (2015), pp. 201–216. ISSN: 0278-6125. DOI: https://doi.org/10.1016/j.jmsy.2015.03.006. URL: https://www.sciencedirect.com/science/article/pii/S0278612515000229.

[67] Heping Chen and Ning Xi. "Automated tool trajectory planning of industrial robots for painting composite surfaces". In: *The International Journal of Advanced Manufacturing Technology* 35.7 (2008), pp. 680–696. DOI: 10.1007/s00170-006-0746-5. URL: https://doi.org/10.1007/s00170-006-0746-5.

[68] Wenzhuo Chen et al. "Design of redundant robot painting system for long non-regular duct". In: *Industrial Robot: An International Journal* 43 (Jan. 2016), pp. 58–64. DOI: 10.1108/IR-06-2015-0113.

[69] Wenzhuo Chen et al. "Paint thickness simulation for robotic painting of curved surfaces based on Euler–Euler approach". In: *Journal of the Brazilian Society of Mechanical Sciences and Engineering* 41 (Apr. 2019). DOI: 10.1007/s40430-019-1651-9.

[70] Yin-An Wang, Xiao-Peng Xie, and Xiao-Hui Lu. "Design of a Double-Nozzle Air Spray Gun and Numerical Research in the Interference Spray Flow Field". In: *Coatings* 10 (May 2020), p. 475. DOI: 10.3390/coatings10050475.

[71] Björn Anersson. "Modeling and simulation of rotary bell spray atomizers in automotive paint shops". PhD thesis. Chalmers University of Technology, 2013.

[72] Christian Winter and Erwin M. Biebl. "Influence of Application Techniques of Automotive Coatings on Radar Transparency". In: *2021 Kleinheubach Conference*. 2021, pp. 1–3. DOI: 10.23919/IEEECONF54431.2021.9598190.

[73] Lucas Ariel Martinez. "Automotive Rotary-Bell Spray Painting Modelling and Simulation". MA thesis. University of Gothenburg, 2012.

[74] Steven Anthony Colbert. "Numerical Simulations of Droplet Trajectories from an Electrostatic Rotary-Bell Atomizer". PhD thesis. Drexel University, 2006.

[75] Nico Guettler et al. "Initial droplet conditions in numerical spray painting by electrostatic rotary bell sprayers". In: *Journal of Coatings Technology and Research* 17.5 (2020), pp. 1091–1104. DOI: 10.1007/s11998-020-00352-1. URL: https://doi.org/10.1007/s11998-020-00352-1.

[76] Joachim Domnick, Andreas Scheibe, and Qiaoyan Ye. "The Simulation of the Electrostatic Spray Painting Process with High-Speed Rotary Bell Atomizers. Part I: Direct Charging". In: *Particle and Particle Systems Characterization* 22 (Sept. 2005), pp. 141 –150. DOI: 10.1002/ppsc.200400968.

[77] Joachim Domnick, Andreas Scheibe, and Qiaoyan Ye. "The Simulation of Electrostatic Spray Painting Process with High-Speed Rotary Bell Atomizers. Part II: External Charging". In: *Particle and Particle Systems Characterization* 23 (Dec. 2006), pp. 408 –416. DOI: 10.1002/ppsc.200601018.

[78] G.M. Tsangaris, G.C. Psarras, and A.J. Kontopoulos. "Dielectric permittivity and loss of an aluminum-filled epoxy resin". In: *Journal of Non-Crystalline Solids* 131-133 (1991). Proceedings of the International Discussion Meetings on Relaxations in Complex Systems, pp. 1164–1168. ISSN: 0022-3093. DOI: https://doi.org/10.1016/0022-3093(91)90747-T. URL: https://www.sciencedirect.com/science/article/pii/002230939190747T.

[79] Ralf Ballhausen. "X-ray spectroscopy of X-ray binaries". doctoralthesis. Friedrich-Alexander-Universität Erlangen-Nürnberg (FAU), 2021.

[80] Bipin K. Agarwal. *X-Ray Spectroscopy*. Vol. 15. Springer Series in Optical Science. Springer Berlin Heidelberg, 1991.

[81] Merck KGaA. May 2022. URL: https://www.merckgroup.com/en/brands/pm/iriodin.html.

[82] Michaela Liese. "Lacke für radarbasierte Fahrerassistenz-Systeme". In: *JOT Journal für Oberflächentechnik* 59.9 (2019), pp. 36–41. DOI: 10.1007/s35144-019-0294-z. URL: https://doi.org/10.1007/s35144-019-0294-z.

[83] Christian M. Schmid et al. "Motion compensation and efficient array design for TDMA FMCW MIMO radar systems". In: *2012 6th European Conference on Antennas and Propagation (EUCAP)*. 2012, pp. 1746–1750. DOI: 10.1109/EuCAP.2012.6206605.

[84] Rodrigo Pérez et al. "Single-Frame Vulnerable Road Users Classification with a 77 GHz FMCW Radar Sensor and a Convolutional Neural Network". In: *2018 19th International Radar Symposium (IRS)*. 2018, pp. 1–10. DOI: 10.23919/IRS.2018.8448126.

[85] Andreas Haderer. *RDL-77G-TX2RX16 Frontend (User Manual)*. 1.0.0. Inras GmbH. Altenbergerstraße 69 4040 Linz, Austria, Dec. 2016.

[86] Joaquin Rams, A. Tejeda, and J. Cabrera. "Refractive indices of rutile as a function of temperature and wavelength". In: *Journal of Applied Physics* 82 (Sept. 1997), pp. 994 –997. DOI: 10.1063/1.365938.

[87] Rakesh Kumar Gupta et al. "Light scattering behavior of oxide nanoparticles". In: *IEEE International Conference on Electro-Information Technology , EIT 2013*. 2013, pp. 1–5. DOI: 10.1109/EIT.2013.6632673.

[88] Christian Winter et al. "Evaluation of Influences of Titanium Dioxide on Radar Sensors Operating at 77 GHz". In: *2022 14th German Microwave Conference (GeMiC)*. 2022, pp. 220–223.

[89] Jean-Francois Hochepied et al. "Dielectric Properties and Characterisation of Titanium Dioxide Obtained by Different Chemistry Methods". In: *Journal of Nanomaterials* 2014 (2014), p. 124814. DOI: 10.1155/2014/124814. URL: https://doi.org/10.1155/2014/124814.

[90] Marshall D. Earle. "The Electrical Conductivity of Titanium Dioxide". In: *Phys. Rev.* 61 (1-2 1942), pp. 56–62. DOI: 10.1103/PhysRev.61.56. URL: https://link.aps.org/doi/10.1103/PhysRev.61.56.

[91] Karl Willy Wagner. "Erklärung der dielektrischen Nachwirkungsvorgänge auf Grund Maxwellscher Vorstellungen". In: *Archiv für Elektrotechnik* 2.9 (1914), pp. 371–387. DOI: 10.1007/BF01657322. URL: https://doi.org/10.1007/BF01657322.

[92] Lord Rayleigh Sec. R.S. "LVI. On the influence of obstacles arranged in rectangular order upon the properties of a medium". In: *The London, Edinburgh, and Dublin Philosophical Magazine and Journal of Science* 34.211 (1892), pp. 481–502. DOI: 10.1080/14786449208620364. eprint: https://doi.org/10.1080/14786449208620364. URL: https://doi.org/10.1080/14786449208620364.

[93] C. Böttcher. "The Dielectric Constant of Crystalline Powders". In: *Recueil des Travaux Chimiques des Pays-Bas* 64 (Sept. 1946), pp. 47–51. DOI: 10.1002/recl.19450640205.